ACQUISITION AND ANALYSIS OF ULTRASONIC WAVEFIELD DATA TO CHARACTERIZE ANGLE-BEAM PROPAGATION AND SCATTERING IN PLATES

A Thesis
Presented to
The Academic Faculty

by

Alexander James Wayne Dawson

In Partial Fulfillment
of the Requirements for the Degree
Doctor of Philosophy in the
School of Electrical and Computer Engineering

Georgia Institute of Technology
December 2015

ACQUISITION AND ANALYSIS OF ULTRASONIC WAVEFIELD DATA TO CHARACTERIZE ANGLE-BEAM PROPAGATION AND SCATTERING IN PLATES

Approved by:

Professor Jennifer E. Michaels,
Advisor
Committee Chair
School of Electrical and Computer Engineering
Georgia Institute of Technology

Professor Aaron D. Lanterman
School of Electrical and Computer Engineering
Georgia Institute of Technology

Professor Thomas E. Michaels
School of Electrical and Computer Engineering
Georgia Institute of Technology

Professor Massimo Ruzzene
School of Aerospace Engineering
Georgia Institute of Technology

Professor Ghassan Al-Regib
School of Electrical and Computer Engineering
Georgia Institute of Technology

Date Approved: 18 August 2015

To my family,

Dan, Michele, Chris, and my wife, Amanda,

without whom this thesis would never have been written.

ACKNOWLEDGEMENTS

I would first like to take the time to express my appreciation for my advisor, Dr. Jennifer Michaels. Without her continuous support, guidance, and encouragement, this thesis would never have been written. Her positive influence extends well beyond the research presented here to all aspects of my life. I will carry with me always everything that she has taught me.

Thank you to all the other committee members, Dr. Ghassan Al-Regib, Dr. Aaron Lanterman, Dr. Thomas Michaels, and Dr. Massimo Ruzzene. Their time, efforts, suggestions, and support are sincerely appreciated.

I would also like to thank all of my friends and colleagues in the QUEST Lab. It was truly an honor to work with Dr. Xin Chen, Dr. Ross Levine, Westin Williams, Joe Kummer, Yu Weng, and Hongye Liu. I would specifically like to thank Xin for welcoming me to the lab and teaching me about ultrasonic experimentation and to Westin for his tireless dedication to improving the wavefield scanner that made my work much easier. In addition to my friends from the lab, I would also like to thank Chris Blanchard, Jake Higbie, Nick Ketchum, Brian Mack, Zack McCoy, Ryan Niklas, Scott Spalding, and Rich Taylor. Although we are separated by great distances, they are never far from my thoughts. I am honored to be counted as a member of such a merry band.

My greatest gratitude goes out to my family, whose love and support throughout graduate school is impossible to repay. First, I would like to thank my parents, Dan and Michele, who instilled in me an insatiable appetite for knowledge, an indomitable work ethic, and unbreakable will to succeed. Second, I would like thank my brother, Chris; through his razor wit has always pushed me to be my best. Lastly, I would like

to thank my wife, Amanda. I cannot find words to express my gratitude for her love, understanding, and support over the years. In many ways, this thesis is as much a culmination of her work as it is mine. I truly could not have done it without her.

The work reported in this thesis was sponsored by the Air Force Research Laboratory (AFRL) under Contract No. FA8650-10-D-5210. I would like to give a special thanks to our program manager, Dr. Eric Lindgren, whose contribution to this work and dedication to the NDE community cannot be overstated. Also, I would like to acknowledge Dr. James Blackshire, who supported the finite element modeling efforts found in this work.

TABLE OF CONTENTS

LIST OF TABLES

LIST OF FIGURES

SUMMARY

The aging of military and civilian aircraft in the United States has prompted a movement towards condition-based maintenance strategies to allow these vehicles to continue to operate safely and cost effectively over the length of their service life and inmany cases beyond. Improvements in NDE techniques could aid in the continuing development of reliable condition-based maintenance routines that reduce the growing operating costs for these aging aircraft.

The objective of this thesis is to present methods for the acquisition and analysis of ultrasonic wavefield data for characterizing angle-beam bulk wave propagation and scattering in plates. The motivation behind studying angle-beam wavefields is that better understanding of the both the incident wavefield and subsequent scattering has the potential to increase the reliability of data interpretation for ultrasonic non-destructive evaluation (NDE) techniques, provide reliable means of ultrasonic model validation, and lead to the development of new wavefield-based inspection methods. The specific contributions of this work include: a reliable means for high-resolution measurement of angle-beam wavefields in plates; a framework for the analysis of angle-beam wavefield data; a method for characterizing scattering behavior by isolating scattered waves from full wavefield data via baseline subtraction; and a method for generating angle-beam scattering patterns from wavefield data.

A description of the experimental setup for the wavefield scanner used to record high resolution wavefield images of wave propagation is provided. Additionally, the trade-offs between data quality and scan time are discussed. Initial experiments are used to characterize angle-beam wave propagation in undamaged plates to establish a foundation on which to build an understanding of angle-beam scattering. Two

classical analysis techniques, the Radon and Fourier transforms, are used to provide a reliable means to identify the direction, speed, and mode of propagating waves; however, they do not allow for the separation of incident and scattered waves, which is needed to provide for more complete characterization of scattering. To this end, baseline subtraction, a technique commonly used to separate incident and scattered waves in ultrasonic structural health monitoring, is formulated for and applied to angle-beam wavefield data.

Existing image processing algorithms are adapted to the problem of separating incident and scattered waves in wavefield images. Two methods for aligning the wavefield data in space and time prior to performing baseline subtraction to compensate for spatial misalignment are presented and their efficacy is evaluated using data acquired before and after introducing notches that originate from a through-hole. Although perfect baseline subtraction is not achieved, the improvement in performance after alignment using either method allows for scattered waves from small defects to be separated and visualized.

Isolation of scattered waves allows for new wavefield-based means of quantifying scattering to be used for characterization. A method is described for generating radial energy maps, which quantify scattering as a function of both scattered angle and phase velocity. These maps allow for scattering of different wave modes to be studied, and they can be converted into angular scattering patterns,for phase velocity ranges of interest. Both the radial energy maps and the scattering patterns are used to characterize scattering from corner notches of various sizes. Lastly, the efficacy of the scattering characterization methods developed in this work is discussed and recommendations are made for future work.

CHAPTER I

INTRODUCTION

This first chapter provides a brief description of the pressing need for improved maintenance strategies and methodologies in an era when the United States infrastructure consists of structures being used well beyond their designed service lives. Motivated by safety and cost concerns, there is a movement towards condition-based maintenance supported by various nondestructive evaluation (NDE) techniques. Research goals are proposed next that aim to study angle-beam ultrasonic NDE techniques using wavefield imaging. The first problem addressed is acquisition of high frequency bulk wavefields, which is difficult because of the high temporal and spatial frequencies involved. The second is the study and characterization of angle-beam wave propagation and scattering using wavefield data. Lastly, research contributions are summarized and the organization of the remaining chapters is provided.

1.1 Background

The United States of America relies on an aging transportation system made up of structures and vehicles that, for economic and political reasons, are being used well beyond their designed service lives. Failures in these aging structures, such as the I-35 bridge collapse in Minneapolis, have drawn national media attention and prompted plans to develop solutions to the aging vehicle and infrastructure problem [1]. Although some of the most overt examples of the dangers of the United States' aging infrastructure have involved the highway system, the problem is widespread.

One of the most dangerous and costly examples of aging structures in the United States is civilian and military aircraft. The operation and maintenance of civilian and military aircraft are quite different; however, the trend in aging aircraft service life is

similar. The cost of operating and maintaining aircraft grows with age. The United States Air Force (USAF) estimates that 70% of of the funds required to develop, qualify, and operate an aircraft in service are spent in operation and maintenance [2].

In an effort to reduce the costs associated with aircraft maintenance, there is a movement away from schedule-based maintenance (SBM) and towards condition-based maintenance (CBM). SBM sets a periodic interval to perform preventive maintenance on a system component regardless of the condition of the component. CBM relies on monitoring of system components so that maintenance actions can be recommended based on the information collected on the condition of the component. CBM attempts to avoid unnecessary maintenance by taking actions only when there is evidence of undesirable changes to a system or component. There are two strategies for condition monitoring in CBM: continuous and periodic. Usually involving the use of mounted or embedded sensors, continuous monitoring measures the operation of a system *in situ*. Continuous monitoring is often limited by three factors: (1) it is expensive, (2) it is often to heavy to be used on aircraft, and (3) the continuous monitoring of raw signals is affected by the system operation, resulting in inaccuracies in data interpretation. Because of the limitations of continuous monitoring and the advantages of periodic inspection including cost effectiveness and accuracy of diagnosis, periodic inspection has become the standard in most industries [3].

Periodic inspection of aircraft components is based on a variety of nondestructive evaluation techniques. NDE techniques involve the evaluation of the properties of a material, component, or system without changing its functionality or causing damage. Since NDE does not alter the article under inspection, it is a valuable tool that can save both time and money in product inspection. Ultrasonic nondestructive evaluation is one of the most widely used NDE methods because ultrasonic energy can effectively penetrate materials of interest, is sensitive to defects of interest, and does not pose environmental hazards.

1.2 Motivation and Research Goals

Bulk wave and more specifically angle-beam ultrasonic NDE is a well established technique, serving as a preferred industrial NDE method for years; however, recent advances in technology have created opportunities for improvement. Angle-beam transducers and wedges are used to introduce a refracted shear wave into a test specimen; the angled path allows defects to be interrogated from different angles, which improves the detectability of certain defects. Wavefield imaging, the measurement of time-domain waveforms over a 2-D rectilinear grid resulting from a fixed source, offers a relatively new way to analyze wave propagation and scattering that has historically not been possible. As applied to lower frequency (under 1 MHz) guided waves, wavefield imaging has been shown to be a powerful tool to both determine the nature of wave propagation and provide quantitative scattering information from defects [4]. Acquisition of higher frequency bulk wavefields in the 1-10 MHz range over larger areas is more challenging because of not only the bandwidth requirements but also the need for fine spatial sampling to prevent aliasing. Advances in ultrasonic equipment, data acquisition, signal processing techniques, computational power, and memory have mitigated some of the challenges associated with bulk wavefield imaging and allowed it to be employed at higher frequencies and on larger areas.

Wavefield imaging has been applied to a wide array of applications including the measurement of angle-beam waves in pipes [5]; however, it has not been used to rigorously study the propagation and scattering of angle-beam waves in plates. The study of angle-beam propagation in plates is of interest to a variety of industries because angle-beam techniques are commonly used in industrial NDE applications and because plates mimic many of the structures on which NDE methods are used. Existing analysis techniques used to study wavefield data are application specific and do not lend themselves well to studying angle-beam scattering from defects. Studying angle-beam scattering using wavefield imaging requires not only developing

new analysis methods, but also understanding how the properties of angle-beam waves influence interpretation of results.

Many of the existing means of quantifying ultrasonic scatting behavior, both experimentally and analytically, have been developed for guided waves and there has been little research into generating experimental angle-beam scattering patterns. Most likely the lack of experimental studies into characterizing bulk wave scattering behavior is due to (1) the large amount of data required to characterize scattering, and (2) large transducer dimensions (relative to wavelength) that make it difficulty to obtain fine enough angular sampling when using conventional transducers.

The primary focus of this work is to study ultrasonic angle-beam wave propagation and scattering, specifically by using wavefield imaging to characterize bulk wave scattering. Methods for the acquisition and analysis of ultrasonic wavefields are developed and described to characterize angle-beam wave propagation and scattering in plates. Greater understanding of the both the incident wavefield and the subsequent scattering from a variety of scatterers and geometrical features, gained from these methods, could be used to increase the reliability of data interpretation of ultrasonic nondestructive evaluation (NDE) techniques, provide a reliable means of ultrasonic model validation, and lead to the development of new wavefield-based techniques. Improvements in NDE techniques could also aid in the continuing development of reliable condition-based maintenance routines that reduce the growing operating costs for aging civilian and military aircraft.

1.3 Contributions

The main objective of this work is to develop methods for the measurement and analysis of angle-beam wavefield data; data that may be used to gain a better understanding of angle-beam propagation, improve ultrasonic NDE, and provide for more rigorous model validation. The first contribution of this work is a reliable means

for high-resolution measurement of angle-beam wavefields in plates. Wavefield acquisition systems have been employed in a variety of applications; however, few of these systems meet the temporal and spatial sampling frequencies required to study angle-beam waves at frequencies of interest for aerospace NDE.

The second contribution of this work is a framework for the analysis of angle-beam wavefield data. Radon and Fourier transforms are used in combination with ray-tracing and finite element models to study angle-beam wave generation and propagation in undamaged plates. These preliminary results provide insight into angle-beam wave propagation that is used to guide scatterer characterization.

The third contribution is a method for characterizing scattering behavior by isolating scattered waves from full wavefield data via baseline subtraction. Using image registration techniques to align sets of wavefield data allows for isolation of the scattering behavior from a defect; in the absence of the incident waves, the scattering can be clearly identified and studied.

The final contribution is a method for generating angle-beam scattering patterns from wavefield data. Scattering patterns can be produced from the wavefield data by partitioning the wavefield data radially outward from the scatterer of interest and using the Fourier transform to separate waves of different velocities. Producing scattering patters that are a function of both angle and velocity can be used not only to study scattering by different wave modes but also to study mode conversion caused by the defect or scatterer.

1.4 Thesis Organization

The remainder of the thesis is organized as follows. Chapter II presents a review of the existing literature focused on prior research on angle-beam ultrasonic NDE methods, wavefield imaging for measuring wave propagation, methods of characterizing wave propagation and scattering behavior, and image registration techniques for improving

scattering isolation using baseline subtraction. The objective and scope of the research presented in this thesis is then placed in the context of this prior work.

Chapter III introduces the experimental methodology used to acquire high fidelity angle-beam wavefield data including an description of equipment, sampling considerations, excitation, signal quality, and various experimental trade-offs. This chapter summarizes all of the data used throughout the paper and provides snapshots of representative wavefield data used for scatterer characterization. Portions of this chapter can be found in Dawson *et al.* [6], which is a extension of the work reported in [7] and [8].

Chapter IV provides initial characterization of angle-beam wave propagation in undamaged plates to establish a foundation on which to build an understanding of angle-beam scattering. Three methods are used to characterize angle-beam wave propagation. The first method is a simple ray-tracing model that is used to described the reflections of angle-beam waves between the surfaces of the plate, which are commonly called skips or V-paths. The second method is to use experimental wavefield measurements to gain a better understanding of angle-beam wave propagation not captured by the ray-tracing model. Finally, a simple 2-D finite element model is constructed and compared to the experimental data, which is published in [9].

Chapter V describes methodologies for analyzing scattering behavior using the wavefield data described in Chapter III. These methods include baseline subtraction, analysis of radially propagating waves referred to as radial energy maps, and scattering pattern techniques. The first portion of this chapter, related to baseline subtraction performance and used for isolating scattering, can be found in Dawson *et al.* [6] and the second portion, related to the radial energy analysis and the scattering patterns, can be found in Kummer *et al.* [10].

Chapter VI presents a detailed analysis of scattering behavior from crack-like corner notches emanating from a through-hole using the analysis techniques described

in Chapter V. The effect of notch size on the scattering behavior is presented and discussed. In addition to the characterization results, the efficacy of the scattering characterization methods is discussed.

Chapter VII concludes this thesis and provides recommendations to guide future research. Specifically, future work should focus on applying the methods described in this work to study a variety of scatterers or defects and on improving the methods themselves.

CHAPTER II

LITERATURE REVIEW

The purpose of the literature review, presented in this chapter, is to discuss prior research related to angle-beam wave propagation and scattering, wavefield imaging, and analysis techniques for ultrasonic waves. Section 2.1 begins with a brief overview of the fundamentals of ultrasonic wave propagation with a focus on waves produced by angle-beam transducers. Section 2.2 discusses the use of ultrasonic waves for nondestructive evaluation (NDE). Section 2.3 outlines current research efforts into the modeling of ultrasonic wave propagation. Section 2.4 describes the acquisition of wavefield data and outlines applications in which wavefield imaging has been employed. Common methods of presenting and analyzing ultrasonic measurement data which are used throughout the paper are then presented in Section 2.5. Specifically, Section 2.5 focuses on four analysis techniques used to study ultrasonic wave propagation and scattering: the Radon transform, the Fourier transform, baseline subtraction, and scattering pattern estimation. Section 2.6 outlines work in the area of image registration that can be used to improve wavefield baseline subtraction discussed in Section 2.5.4. Finally, Section 2.7 discusses the scope of the research presented in this thesis placed in the context of this prior work and outlines the objectives of the work.

2.1 Fundamentals of Ultrasonic Wave Propagation

The fundamentals of ultrasonic wave propagation in isotropic solids have been well understood since the early twentieth century. The works of Rayleigh, Lamb, and Stonely serve as the foundation for understanding of ultrasonic wave propagation [11, 12, 13]. Ultrasonic waves are divided into two classifications: bulk waves and guided waves; both have been studied extensively for use in ultrasonic NDE.

2.1.1 Types of Ultrasonic Waves in Plates

Bulk elastic wave propagation occurs in an infinite medium or a medium with dimensions large relative to the wavelength of the propagating wave. Bulk waves are relatively simple in nature; they propagate along paths defined by the wavenumber. The wavenumber is a vector in three-dimensional space that contains information about the direction and velocity of a propagating wave. There are two types of bulk waves which exist in solid media: longitudinal and shear waves. Longitudinal waves are characterized by particle motion parallel to the direction of wave propagation. Shear waves, on the other hand, are characterized by particle motion perpendicular to the direction of wave propagation. Theoretically, shear waves are defined as shear-horizontal or shear-vertical depending the polarization relative a surface of the medium [14]. Bulk waves have been used extensively for industrial ultrasonic NDE applications because of their well understood propagation characteristics, sensitivity to defects, and ease of interpretation.

Guided elastic waves are formed from the interaction of shear and longitudinal waves with boundaries of a medium. Guided waves are typically categorized by the type of boundary condition that produces them. The main categories of guided waves that propagate in plates include: Rayleigh waves [11], Lamb waves [12], and Stoneley waves [13]. Rayleigh waves are a type of surface wave generated by the interaction of longitudinal and shear waves at a free boundary of a solid body and travel along that boundary. Lamb waves propagate in thin, solid plate or plate-like media with free boundaries and unlike surface waves excite the media throughout its thickness. Stoneley waves are similar to Rayleigh waves only they propagate at the interface of two solid half-spaces.

2.1.2 Ultrasonic Wave Propagation Equations

Bulk waves and guided waves are governed by the same wave equations, however, the nature of their propagation differs. Here, the general equations for wave propagation are presented.

Propagating wave displacement is expressed as 3-D vector that is a function of time, t, and three-dimensional space, (x, y, z), i.e., $\mathbf{u}(x, y, z, t)$. Propagating elastic waves in a homogeneous, isotropic medium obey the elastodynamic wave equation,

$$\mu\nabla^2\mathbf{u} + (\mu + \lambda)\nabla(\nabla\mathbf{u}) + \mathbf{F} = \rho\frac{\partial^2\mathbf{u}}{\partial t^2} \tag{1}$$

where $\mathbf{u}$ is the 3-D displacement vector and (μ, λ) are the Lamè parameters. The solution to the elastodynamic wave equation, i.e., the particle displacement in one direction, can be expressed as a plane wave of the form,

$$u(t, x, y, z) = A\cos(\omega t - k_x x - k_y y - k_z z), \tag{2}$$

where ω is the frequency and k_x, k_y, and k_z are the wavenumber in the x-, y-, and z-directions respectively. Elastic waves propagate as either longitudinal or shear waves with velocities

$$c_l = \sqrt{\frac{\lambda + 2\mu}{\rho}} \tag{3a}$$

and

$$c_s = \sqrt{\frac{2\mu}{\rho}}, \tag{3b}$$

respectively. Often times, the wavenumber will be expressed as a vector quantity such that

$$\vec{k} = k_x\vec{x} + k_y\vec{y} + k_x\vec{z}. \tag{4}$$

There is a fundamental relationship between the frequency of the propagating wave,

ω, the propagation velocity, c, and the magnitude of the wavenumber

$$|k| = \frac{\omega}{c}. \tag{5}$$

In essence, the wavenumber describes both the direction and the velocity of the wave propagation [14].

2.2 Nondestructive Evaluation

A variety of existing nondestructive evaluation (NDE) methods are being used to meet the growing need for accurate and reliable means of periodic inspection of aircraft components and other aging infrastructure elements discussed in Section 1.1. The American Society for Nondestructive Testing defines NDE as "the examination of an object with technology that does not affect the object's future usefulness" [15]. The purpose of this section is to provide a general overview of NDE methodology and an in-depth description of ultrasonic angle-beam NDE.

2.2.1 Overview of NDE

The terms nondestructive evaluation (NDE) and nondestructive testing (NDT) are often used interchangeably; however in practice, NDE is more quantitative in nature than NDT. NDT is concerned with assuring, by detecting defects or damage, that structural components and systems are capable of performing their function in a reliable and cost effective fashion. NDE, on the other hand, refers to not only locating a defect, but also measuring the characteristics of the defect such as its size, shape, and orientation. In an effort to reduce the costs associated with maintenance, there is a movement towards condition-based maintenance. NDE engineers are working to develop and implement tests that locate and characterize conditions and defects that may cause critical system components to fail. Since NDE inspection methodologies allow for the inspection of a structure without interfering with its future performance;

they provide a balance between quality control and cost-effectiveness that is critical in maintaining the safety of important civilian and military equipment [16].

There are a variety of common inspection methods that are used for NDE including: Visual and Optical Testing (VT), Radiography (RT), Magnetic Particle Testing (MT), Ultrasonic Testing (UT), Penetrant Testing (PT), Electromagnetic Testing (ET), Leak Testing (LT), and Acoustic Emission Testing (AE). Of these, ultrasonic testing is one of the most widely used NDE methods since it can typically interrogate specimens at depths that cannot be achieved with other methods and is sensitive to a variety of defects [15, 17].

2.2.2 Ultrasonic Waves for NDE

In general, ultrasonic NDE, regardless of the technique used, generates elastic waves in a specimen or structure under test with an initial excitation and based on the received echoes, quantitative judgments are made about the specimen. Since ultrasonic NDE relies on the reception of these echoes, the performance of ultrasonic NDE is dependent on the size of a defect relative to the wavelength and the degree to which the defect scatters waves. Ultrasonic NDE employs a variety of waves to detect different kinds of defects.

The waves used predominate in ultrasonic NDE are bulk waves, Rayleigh waves, and Lamb waves. Bulk waves offer several advantages over Rayleigh and Lamb waves. As surface waves, Rayleigh waves do not penetrate into the depth of specimen; consequently, can only be used to detect surface-breaking or near-surface defects, *e.g.*, [18, 19]. Bulk waves are not confined to the surface of the specimen and can be used to detect and locate a much wider variety of defects. Also high frequency bulk waves can detect and locate smaller defects than Lamb waves.

Lamb waves propagate in elastic media with a thickness that is small relative to the wavelength [20]. Due to the ability of Lamb waves to travel long distances with

lower losses in amplitude as compared to bulk waves, they have become an active topic in current ultrasonic NDE research, *e.g.*, [21, 22, 23]. Although Lamb waves present some advantages over bulk waves for use in ultrasonic NDE, there are several disadvantages that have prevented widespread implementation of Lamb waves methods in practical NDE systems. Lamb waves are dispersive; i.e., the velocity of propagation is a function of the frequency. As a result, the shape of the wave changes as it propagates through the media. Lamb waves are also multimodal, propagating as symmetric and anti-symmetric modes. Depending on the wavelength of the Lamb wave relative to the thickness of the plate, multiples wave modes exist, each propagating at a different velocity. The dispersive and multimodal nature of Lamb waves makes interpretation and diagnosis of Lamb wave signals for ultrasonic NDE more challenging and less reliable than for bulk waves [24, 25].

2.2.3 Angle-Beam Ultrasonic NDE

Angle-beam ultrasonic testing is one of the most common NDE practices that uses bulk waves for the detection, location and characterization of a variety of material defects and damage. Angle-beam ultrasonic NDE is a specific type of bulk wave NDE that is performed using probes consisting of the transducer itself and a plexiglass or acrylic wedge that allows a variety of refracted angles to be achieved. The typical configuration for an angle-beam transducer as well as relevant parameters can be seen in Figure 1. The refracted angle, θ_R, is the angle at which the refracted wave is transmitted into the specimen under test. The refracted angle in a particular material (typically steel) is noted on the incidence wedges. The skip distance, the distance measured along the surface of the specimen where the beam reaches the surface of the plate, and the V-path distance, the distance the beam travels within the specimen, are a function of both the refracted angle, θ_R, and the specimen thickness, T. Inspectors or technicians use calculations of the V-path and skip distance to

establish a relationship between the transducer location on the surface of the material and corresponding locations of internal defects.

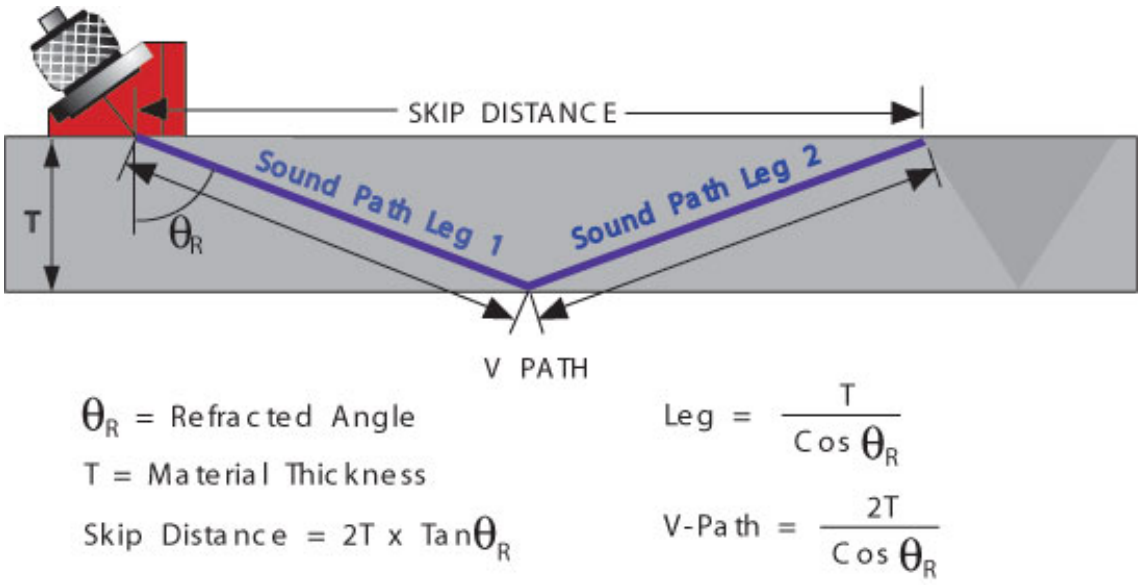

Figure 1: Diagram and equations for angle-beam wave propagation, reproduced from [16].

In addition to the refracted angle, there are two other characteristics of angle-beam transducers: the probe index and the beam spread. The probe index, or incident point, is the point along the wedge where the transducer beams emerges from the bottom of the incidence wedge. Like the refracted angle, the probe index is noted on the incidence wedge. Although Figure 1 depicts the sound path propagating as a line, angle-beam waves propagate as a diverging beam. The dimensions of this beam increase as a function of the propagation distance; the beam spread is a measure of the change in beam's angular width as as it propagates through the medium. Generally a beam spread diagram can be determined from calibration measurements [15, 17].

Techniques for angle-beam testing are well established and have been used in a variety of industries for both manual and automated testing. In general angle-beam inspection is accomplished by moving the angle-beam probe along the surface of the specimen under inspection and observing the received, or backscattered, echo. The

size and shape of the received echo may be used as an indicator of defect properties. Angle-beam methods can be categorized as pulse-echo (common transmitter and receiver) or pitch-catch (separate transmitter and receiver). For the pitch-catch method, the receiver may be located either opposite the transmitter, where it receives the forward propagated wave, or adjacent to the transmitter, where it receives backscattered waves [26]. In addition to using angle-beam wedges for inspection, it is also common practice to use arrays for the pulse-echo configuration where appropriate delay laws are employed to steer the beam through a range of refracted angles [27, 28].

Ultrasonic angle-beam inspection is frequently used to locate cracks and corrosion and to inspect fastener holes and welds in both plates and pipes. Locating planar cracks is accomplished by sweeping a shear wave angle-beam probe over the region of interest and observing the rise and fall of the received echo. Detecting planar cracks is challenging because often the crack scatters waves in a direction other than back to the probe and pulse-echo techniques have little likelihood of detection. For example, when operating in a pulse-echo configuration, a probe is more likely to receive backscattered waves when the waves are incident on the broadside of the crack. The performance of angle-beam inspections is dependent on the relative position of the probe and the defect.

High-angle longitudinal wave angle-beam probes have also been employed to detect corrosion. These probes are applied in a pitch-catch mode and the presence of a travel-time change is used to detect corrosion [26].

Angle-beam inspection of fastener holes is typically used to detect fatigue cracks emanating from the hole. Cracks can be detected by sweeping the probe around the hole and observing if there are echoes received other than those scattered from the hole. The interaction of waves scattered from the hole and the fatigue crack can often make locating and sizing of these defects difficult [26]. Waves diffracting from the tips

of a crack can be used instead of the direct reflections for detecting and sizing cracks in a method referred to as time-of-flight diffraction (TOFD). Since, the diffracted energy from the tip of a crack is distributed over a range of angles it is less sensitive to defect orientation. One limitation of TOFD is the difficulty of sizing cracks that are not perpendicular to the inspection surface [29, 30].

There are several weld defects, *e.g.*, slag, inclusions, and porosity, that can be detected using angle-beam methods. The type of defect and weld geometry often dictates the wedge angle used for the inspection. Typically, weld inspections are performed by placing the probe at a distance of one skip from the weld and then moving the probe along the length of the weld. Perturbing distance of the probe from the weld and observing the received echoes provides indication about the presence and characteristics of defects [26].

Many of the angle-beam techniques used to inspect plates are also used to inspect pipes. Inspection of pipes using pulse echo is complicated by the curvature of the pipe, which can often direct scattered energy away from the probe, by irregularities in the pipe wall thickness, and by waves propagating around the circumference of the pipe. A pitch-catch configuration can mitigate some of these complications; however, great care must be taken to control the location and orientation of the probe relative to the pipe surface. Special probe designs that focus the ultrasonic energy more precisely can also improve the inspection quality [26].

2.3 Modeling Ultrasonic Wave Propagation

Prior to the development of the computer, ultrasonic modeling efforts were restricted to analytical models developed from solutions to the elastodynamic wave equation summarized in Section 2.1.2. Although limited mainly to simplified geometries, analytical or quantitative models were able to explain and provide insight into a variety of wave propagation phenomena. Initially, the solutions to the elastodynamic wave

equation provided insight into bulk wave propagation in free space [31, 32]. Improved analytical models were developed based on extensions of the wave equation and provided information relevant to ultrasonic NDE techniques including transducer radiation/reception, material attenuation, NDE measurement, scattering from defects, and defect sizing [33]. Recently, analytical models have been developed, which have been able to approximate realistic NDE scenarios, including a model of scattering of oblique incidence shear waves from a cylindrical cavity [34], and a modular Gaussian beam model was developed to predict corner crack pulse-echo signals for an angle-beam contact transducer [35].

Analytic models are powerful tools for developing understanding into the fundamentals of wave propagation and scattering; however, they are often limited to analytically tractable problems. In the mid-1970's, developments in computing power allowed for more widespread implementation of finite element (FE) and finite difference (FD) methods to the modeling of ultrasonic wave propagation that were too complex or tedious for analytical methods. Examples of these early modeling efforts include determination of static stress fields, study of the vibration modes in piezoelectric transducer arrays, investigation of the motion of rigid wave guides and surface acoustic wave (SAW) devices [36], and predicting 2-D displacement in bars and blocks [37]. More recent models have been used to simulate ultrasonic imaging arrays [38], to generate full matrix capture data for studying an ultrasonic array post-processing technique for determining crack depth [39], to simulate wave propagation in isotropic media using the commercial software package COMSOL [40], and to simulate ultrasonic fields and received signals from an angle-beam transducer [41] similar to those used here. Although finite element/difference methods are powerful tools, even with modern computers, they are still limited by memory and computational power constraints.

In addition to purely analytical and finite element/difference models, several semi-analytical or hybrid models that blend aspects of both have been developed. Recent examples of these hybrid or semi-analytical models include using a combination of FD methods and the Rayleigh integral to model ultrasonic fields scattered by defects [42], using the distributed point source method to model wave propagation for oblique incidence ultrasonic waves in an immersed plate [43], and using a combination of continuity equations and the commercial software package ABAQUS [44] to allow for the simulation of larger 3-D problems.

One popular semi-analytic simulation software for modeling realistic NDE scenarios is CIVA. Developed by the CEA (the French Atomic Energy Commission) and collaboration of academic and industrial partners, CIVA is composed of simulation, imaging, and analysis modules, which allow for the design, simulation, and optimization of inspection techniques. CIVA has the capabilities to simulate ultrasonic (CIVA UT), x-ray/gamma-ray/computed tomography (CIVA RT-CT), eddy current (CIVA ET), and guided waves (CIVA GW) techniques [45, 46]. CIVA has been used recently to simulate the inspection multi-layered metallic structures [47] and scattering from cracks [48].

Although some aspects of the models presented in this section were verified experimentally, full wavefield data, which is described in the next section, would be useful for a more complete validation. Finite element and finite difference methods could be used to model angle-beam wave propagation, but there do not appear to be any results in the literature that show model data similar to what can be measured via wavefield imaging; it is presumed that computational issues are the limiting factor.

2.4 Ultrasonic Wavefield Measurements

Wavefield imaging generally refers to the measurement of time-domain waveforms over a 2-D rectilinear grid resulting from a fixed source. Wavefield imaging produces

three-dimensional data, $f(t, x, y)$, that is a function of time, t, and two spatial coordinates, x and y. Wavefield imaging typically measures the surface displacement of a specimen and can be performed using either a scanning air-coupled ultrasonic transducer (SAUT) [49] or a scanning laser Doppler vibrometer (SLDV) [50]. SLDV can be accomplished by either mechanically scanning a commercially available single-point or multi-point laser Doppler vibrometers (LDV) or by employing a commercial SLDV system, which moves the laser point-to-point using a system of mirrors [51]. Wavefield imaging, as applied to lower frequency (under 1 MHz) guided waves, has been shown to be a powerful tool to both determine the nature of wave propagation and provide quantitative scattering information from defects [4]. Wavefield imaging has been used to study, for example, Rayleigh waves propagating in heterogeneous granite slabs [52], surface wave propagation in concrete [53], laser generated wave interaction with welds in steel plates [54], and guided wave interaction with delaminations in composites [55, 56].

Acquisition of higher frequency bulk wavefields in the 1-10 MHz range over larger areas is more challenging because of not only the bandwidth requirements but also the need for fine spatial sampling to prevent aliasing. The difficulties associated with bulk wavefield imaging have, historically, limited its use to either lower frequencies (e.g., under 1 MHz) or to scans over small areas such as the characterization of disc-shaped compression and shear-mode piezoelectric transducers [57], the characterization of bulk wave devices over small areas [58], and the measurement of surface acoustic wave propagation over small distances or areas [59, 60].

Recent advances in ultrasonic equipment, data acquisition, signal processing techniques, computational power, and memory have mitigated some of the challenges associated with bulk wavefield imaging and allowed it to be employed on higher frequency and larger scale applications. Acquisition of wavefields in the 1-10 MHz range

over larger areas have been used to measure surface acoustic waves to visualize reflections from a complex, surface-breaking crack [61], to measure waves generated by a pulsed infrared laser in an effort to simulate laboratory scale seismic waves [62], and to measure bulk wave propagation in pipes and blocks [5].

2.5 Analysis Techniques for Ultrasonic Wavefields

Although wavefield imaging is used in a wide array of applications to measure a variety of wave types, the analysis techniques for ultrasonic wavefields generally rely on fundamental wave propagation governed by the mathematic relationships summarized in Section 2.1.2. Two techniques that are particularly useful for identifying propagating wave modes are the Radon and Fourier transforms. Another technique, baseline subtraction, can be used to isolate and study scattering behavior. The final technique described here, scattering patterns, are typically used by the ultrasonic community to quantify scattering as a function of incident and scattered angle. Wavefield data is partitioned and formatted depending on the type of analysis being performed.

2.5.1 Formatting Ultrasonic Data for Analysis

Wavefield data can be partitioned into the common means of ultrasonic data presentation for analysis. The three common means of ultrasonic data presentation are the A-scan, the B-scan, and the C-scan, which are illustrated in Figure 2. Since the three scan types are drawn from the wavefield data, the terminology and purpose of presenting the data in the formats used here is different the traditional use in ultrasonic testing.

The A-scan is a display of the received ultrasonic signal as a function of time. In traditional ultrasonics, the A-scan can be used to estimate relative discontinuity sizes by comparing the signal amplitude of known and unknown reflectors. Here, the one-dimensional A-scan, $f(t)$, is obtained from the wavefield data by observing the data at a single spatial (x, y) sample.

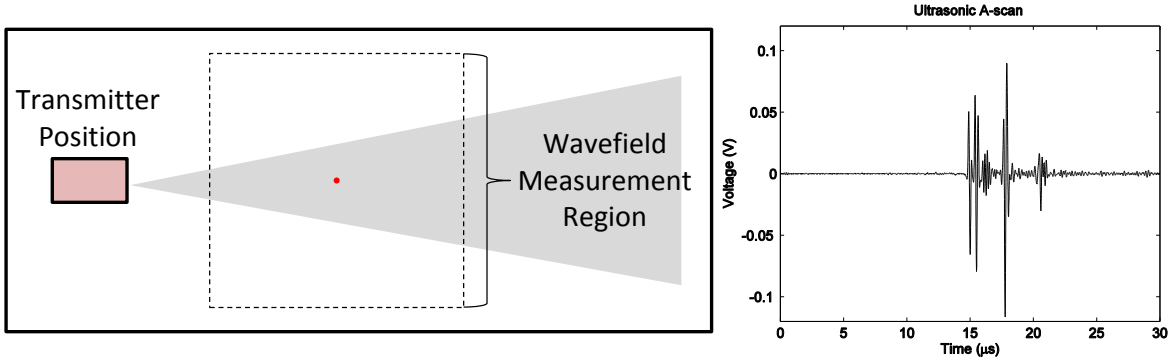

(a) A-Scan: single point in the wavefield data

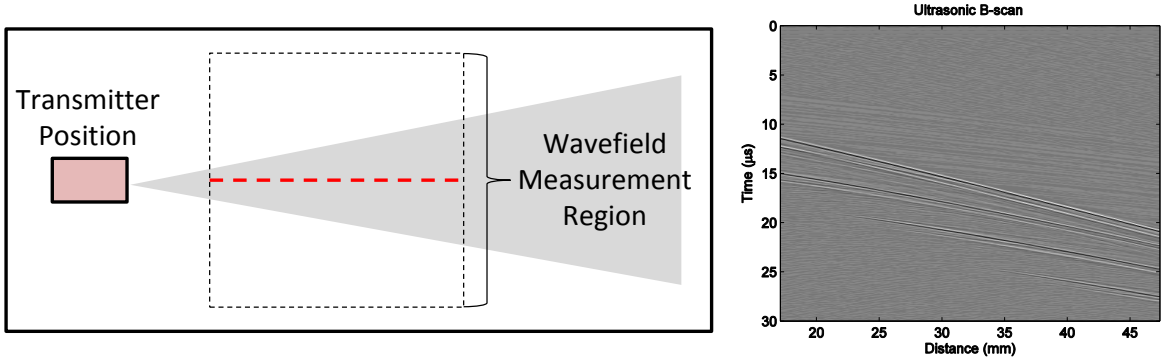

(b) B-scan: line of points in the wavefield data

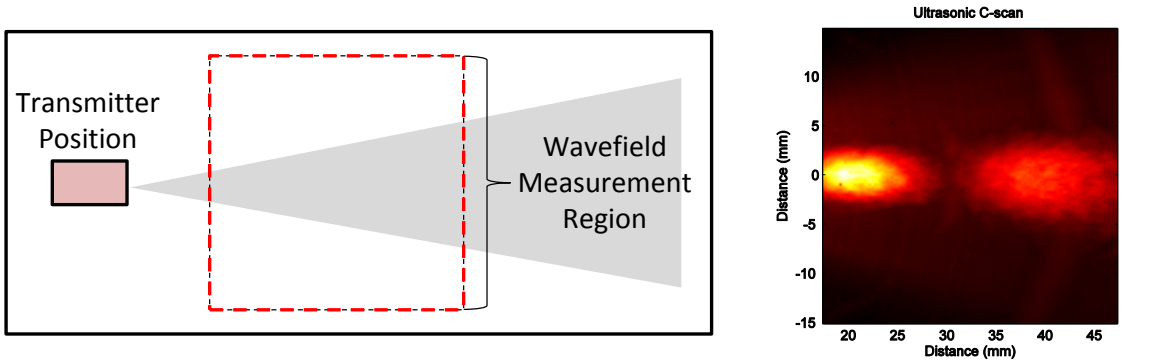

(c) C-Scan: wavefield energy for each point in the wavefield

Figure 2: Wavefield data partitioned into common ultrasonic data formats for presentation and analysis.

In the traditional B-scan, the time-of-flight (travel time) of the sound energy is displayed along the vertical axis and the linear position of the transducer is displayed along the horizontal axis. It can be used to estimate the depth of the reflector and its approximate linear dimensions in the scan direction. The two-dimensional B-scan, $f(r,t)$, as defined here, is obtained from the wavefield data by observing the wavefield data along a coordinate line and is used to analyze the propagation characteristics of waves.

Traditionally, the C-scan provides an image of the features that reflect and scatter the sound within and on the surfaces of the test piece. The plane of the image is parallel to the scan pattern of the transducer. The two-dimensional C-scan, $f(x,y)$, as defined here, is obtained from the wavefield data by observing the data at a single time sample, referred to as a frame, or by calculating the energy over many frames. The most common ultrasonic analysis techniques utilizes data that is formated in one of these three formats [16, 63].

2.5.2 Radon Transform

The slant-stack Radon transform, also referred to as τ-p mapping, is a technique commonly used in geophysical signal processing to identify and localize seismic waves [64, 65]. Because of the similarity in the ratio of the wavelength of the propagating wave to the dimensions of the body in which the waves propagate, there are many analogs between the techniques used to analyze ultrasonic and seismic waves [66]. Here the slant-stack Radon transform is used primarily for identification of the propagating waves based on their velocity. From the B-scan data, $f(t,x)$, the Radon transform can be computed as

$$g(\tau,p) = \int_x f(\tau + px, x)dx, \tag{6}$$

where τ is the time offset, p is the slowness, and x is the distance offset (distance from the transducer). In essence, the Radon transform maps from the space-time domain into the offset-slowness domain. It is important to note that the offset time is the time of a straight line in the x-t plane at the source location ($x = 0$), not the arrival time of the wave. Angle-beam data are measured on the surface of the plate and as a result the slowness, $p = 1/c_p$, is a function of the phase velocity, c_p, as projected on the surface, which is not the same as the phase velocity along the direction of propagation. The slowness or phase velocity can be used identify the wave modes that are propagating in the plate.

2.5.3 Frequency-Wavenumber Analysis

Frequency-wavenumber analysis is a common analysis technique used to identify propagating wave modes. General frequency-wavenumber analysis is performed using a Fourier transform which maps a four-dimensional time-space function, $f(t, x, y, z)$, of three spatial coordinates, x, y, and z, and a single time coordinate, t, into a four dimensional frequency-wavenumber function, $g(\omega, k_x, k_y, k_z)$, of three wavenumber coordinates, k_x, k_y, and k_z, and a single frequency coordinate, ω [67]. The dimensionality of the general frequency-wavenumber analysis can be restricted to analyze either the full wavefield data or any subset of it described in Section 2.5.1. Although all operations are performed on discrete wavefield data sets, the continuous notation is used for ease of presentation. The wavefield data,$w(t, x, y)$, can be transformed into the frequency-wavenumber domain, $W(\omega, k_x, k_y)$, using a three dimensional Fourier transform,

$$W(\omega, k_x, k_y) = \int_{-\infty}^{\infty} \int_{-\infty}^{\infty} \int_{-\infty}^{\infty} w(t, x, y) \exp\left(-\jmath(\omega t - k_x x - k_y y)\right) dt dx dy. \tag{7}$$

The frequency-wavenumber domain can be used to identify the propagating wave modes as described in [68]. In addition to being used as an analysis technique for

identify propagating wave modes, the Fourier transform can be used to filter different wave modes [69].

2.5.4 Baseline Subtraction

Baseline subtraction is a technique used to isolate the effect of changes in a system by examining the differences in signals taken before and after the changes occurred. It was previously used on signals obtained from discrete transducers and not on complete wavefields; however, both applications will be discussed here.

2.5.4.1 Baseline Subtraction Methodology

The ultrasonic baseline subtraction paradigm typically used in structural health monitoring (SHM) involves the subtraction of a signal recorded when a structure is in pristine condition, referred to as the baseline, from the current test signals in order to isolate changes, such as damage, to the structure. Baseline subtraction in the SHM framework uses a permanently mounted array of transducers that typically produce guided waves to interrogate a structure throughout its service life. Comparison of the signals from various times during the structure's life with a baseline can be used to detect and monitor changes to the structure. The goal of wavefield baseline subtraction, as defined here, is the separation of waves scattered off a known defect from the full wavefield to provide quantitative scattering information about the defect. To quantify a known defect using wavefield baseline subtraction, first a baseline scan is performed on a specimen. Then the specimen, in this case the plate, is typically removed from the wavefield scanning fixture and the defect is introduced. The specimen is then remounted and a second scan is performed. The success of baseline subtraction methods is dependent on their ability to suppress benign structural features and isolate damage [70].

The sensitivity of the baseline subtraction is dependent on the degree to which signals resulting from structural elements remain consistent from measurement to

measurement. Generally, signal inconsistencies that reduce the sensitivity of baseline subtraction techniques are the result of uncontrolled environmental conditions the structure is subjected to during measurement. Although the environmental conditions that have an effect on the sensitivity of baseline subtraction can vary greatly between industries, the effect of temperature is both universal and pervasive. Unlike SHM applications for which the transducers are permanently attached to the specimen, spatial alignment issues also affect the performance of wavefield baseline subtraction techniques.

2.5.4.2 Effects of Temperature on Baseline Subtraction

The temperature of a structure affects its dimensions due to thermal expansion and the velocity at which the ultrasonic waves propagate. Both of these factors affect the quality of baseline subtraction techniques, making it difficult to distinguish structural damage from temperature effects. For wavefield baseline subtraction, since the receivers are not affixed to the structure, changes in structural dimensions do not affect the spacing and pattern of the receiver locations, but the location of the pattern on the specimen could be shifted. It is virtually impossible to calculate how much the pattern will shift for a given temperature change because the shift is a function of the thermal expansion of not only the plate itself but any relative motion between the laser vibrometer and the specimen mounting. Regardless, the net effect is a translation of the receiver pattern on the surface of the plate, which is essentially identical to other sources of spatial misalignment.

A great deal of research has been devoted to developing methods to compensate for temperature differences between measurements used for baseline subtraction in SHM applications. These methods can be divided into two categories: optimal baseline subtraction (OBS) and baseline signal stretch (BSS).

OBS is a data-driven approach, first developed by Lu and Michaels, which records

a set of baseline measurements at a variety of temperatures spanning the expected operating operating range of the structure and then selects the baseline that most closely matches the current measurement. Once the optimum baseline has been selected it is adjusted to bast match the current measurement [71].

BSS is a model-driven approach that relies on model of the effects of temperature change on the wave propagation. In general these models assume that temperature influences the wave velocity and results in a time-dependent delay between the baseline and current measurement. BSS methods compensates for the time-dependent delay by stretching or compressing the baseline measurement to match the current signal [71]. The stretching of the baseline signal can be accomplished using data resampling via the FFT [72], the scale transform [73], or instantaneous phase matching via the Hilbert transform [74].

Although the model of the effects of temperature eliminates the need to to take multiple baseline measurements, the combination of the OBS and BSS methods often improves the performance of baseline subtraction. Lu et al. improved the method developed by the Lu and Michaels by incorporating BSS methods such as stretch/shift algorithms and weighted averaging of the baselines taken at different temperatures. The flexibility of the new method increased the sensitivity of the baseline subtraction by reducing the variability between the baseline and current measurements adaptively [75].

2.5.4.3 Effects of Spatial Misalignment on Baseline Subtraction

Unlike SHM applications for which the transducers are permanently attached to the specimen, spatial alignment issues must be considered for wavefield baseline subtraction. The first source of spatial misalignment is a result of removing and remounting the specimen. If the plate is not remounted in exactly the same position, then a global spatial misalignment will result between the two wavefield scans. A second

source of spatial misalignment is lack of repeatability in the mechanical motion of the scanning operation, resulting in local spatial misalignment. Such local variations may be random or systematic depending upon the specific scanning system employed.

2.5.5 Characterizing Scattering Behavior

In the area of NDE, a great deal of current research is focused on integrating information from defect characteristics, ultrasonic modeling techniques, and statistical measures of reliability to improve NDE inspection capabilities. NDE, especially ultrasonic NDE, is performed by highly trained technicians to reliably detect and characterize defects in a variety of structures. Technicians rely on their training and knowledge of ultrasonic scattering by the defects they are likely to encounter. Researchers, by investigating interactions of ultrasonic waves with defects and methods for distinguishing between defects, help improve the reliability and accuracy of NDE methods. Effective defect characterization is fundamental to the improvement of NDE methods.

The scattering behavior of a defect is a function of the properties of the defect such as location, type, orientation, shape, and size [16]. Common defect locations include surface-breaking, near-surface, and sub-surface. Common defect types include linear defects such as cracks and volumetric defects such as inclusions or voids. The orientation of a defect is typically described relative to the surface over which the inspection is being performed; different NDE methods are sentive to defects at certain orientation [15, 17]. For example, cracks oriented normal to the inspection surface can be difficult to detect with normal incident waves. Given the variety of scatterers, the methods used to describe scattering behavior generally distill this behavior into a function of the incident and scattered angles.

There are several methods of characterizing defect scattering behavior; however,

they share some common characteristics. Early analysis of ultrasonic scattering followed many of the methods used for electromagnetic and acoustic scattering and usually evolved from solutions for simplified geometries such as cylinders and spheres [76]. Scattering behavior is usually quantified by either transmission and reflection coefficients or by scattering coefficients. Transmission and reflection coefficients are defined as the amplitude or energy ratio between the transmitted (or reflected) wave and the incident wave [14] and are usually used to characterize linear scatters such as bonds or welds. Scattering coefficients are used to characterize scattering in multiple directions and are defined as the amplitude or energy ratio between the scattered wave and the incident wave. Early analysis of ultrasonic scattering produced models for bulk wave scattering in infinite solids, generally called scattering patterns, as a function of the scattered angle for some fixed angle of incidence [76] and then validated these models experimentally [77]. The procedure for fixed angles of incidence has been extended to all angles of incidence to form scattering matrices [78], which express the scattering behavior for incident and scattered angles ranging from 0° to 360°.

Scattering information has been obtained for both bulk and guided waves for a variety of defects; however, scattering patterns are mostly produced using ultrasonic models, like those described in Section 2.3, because the amount of data required to produce experimental scattering patterns/matrices is often prohibitive. Scattering behavior in the form of transmission/reflection coefficients has been obtained for Lamb wave scattering from strip welds [79], rivet holes with edge cracks [80], adhesively bonded joints [81, 82], and through-thickness cracks [83]. Lamb wave scattering behavior in the form of scattering patterns/matrices has been obtained from models and/or experiment measurements for through-holes [84, 85], notches and cracks [86], and crack-like defects emanating from through-holes [87]. Scattering patterns/matrices have been produced from models for bulk wave scattering from near and surface-breaking defects [88] and from rough crack-like defects [89]. In some

cases the scattering patterns produced from these models have been validated experimentally [90].

Although there has been great deal of work into quantifying Lamb wave scattering, both experimentally and analytically, there has been little research into producing bulk wave and more specifically angle-beam scattering patterns for defects in plates. Most likely the lack of experimental studies into characterizing angle-beam wave scattering behavior is because of (1) the large amount of data required to characterize scattering, and (2) large transducer dimensions (relative to wavelength) makes it difficult to obtain fine enough angular sampling with discrete transducers. Fortunately, wavefield imaging alleviates these issues and allows for robust and detailed the characterization of bulk wave scattering.

2.6 Image Registration

In the presence of the unavoidable effects of temperature and spatial misalignment on the baseline subtraction of wavefield images, means of compensating for these effects are necessary to achieve the level of baseline subtraction performance required to isolate scattered waves. The field of image processing, specifically the area of computer vision, has been concerned with developing algorithms that can robustly measure and correct for differences in images due to changes in location, rotation, and illumination similar to those resulting from temperature and misalignment in wavefield measurements. Section 2.6.1 describes the common motion changes that can occur between a pair of images and Section 2.6.2 outlines the common image alignment or registration methods that exist to estimate and correct for the alignment differences between images. Both Sections 2.6.1 and 2.6.2 are drawn extensively from [91, 92], which provide a comprehensive overview of image registration techniques, and additional references are included where necessary.

2.6.1 Models for Image Motion

Image registration methods rely on mathematical models that map between the pixel coordinates in two images; specifically parametric motion models can be constructed for 2-D and 3-D image motion. The misalignment of wavefield images will be assumed to be the result of 2-D image motion and not 3-D image motion due to changes in the viewing angle, thus the discussion in this section will be limited to 2-D coordinate transformations. The general equation for a 2-D coordinate transformation is

$$\mathbf{x}' = \mathbf{T}\mathbf{x}. \tag{8}$$

where $\mathbf{x}$ is the augmented original pixel coordinates $(x, y, 1)$ and $\mathbf{x}'$ is the transformed coordinates (x', y') following the image motion represented by the transformation matrix $\mathbf{T}$. The degrees of freedom (DoF), which describes the complexity of the image motion, determines both the composition and dimensionality of the transformation matrix, $\mathbf{T}$. Table 1 describes the most common image transformation including composition, dimensionality, and complexity; visually these transforms are displayed in Figure 3. As a note, the transformations increase in complexity moving down Table 1; each simpler transformation, i.e., the groups above are a subset of the more complicated groups below.

Table 1: Summary of 2-D coordinate transformations; reproduction of Table 2.1 from [91].

Name	Matrix Expression	Description	DoF
Translation	$\mathbf{T} = [\mathbf{I}\|\mathbf{t}]_{2\times3}$	Motion in one or both the x- and y-directions	2
Euclidean	$\mathbf{T} = [\mathbf{R}\|\mathbf{t}]_{2\times3}$	Translation and rotation	3
Similarity	$\mathbf{T} = [s\mathbf{R}\|\mathbf{t}]_{2\times3}$	Translation, rotation, and scaling	4
Affine	$\mathbf{T} = [\mathbf{A}]_{2\times3}$	Transformation that preserves collinearity and distance ratios	6
Projective	$\mathbf{T} = [\mathbf{P}]_{3\times3}$	Transformation that preserves straight lines	8

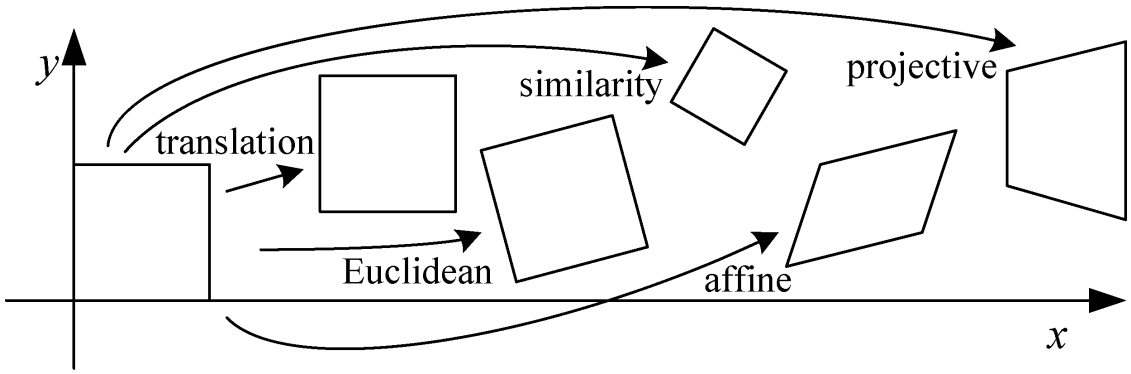

Figure 3: Visualization of 2-D image transformations; reproduction of Figure 2.2 from [91].

2.6.2 Overview of Image Registration Methods

Image registration methods are methods used to estimate the transformation matrix that maps between two identical or similar images using an error metric to quantify the differences between the pair of images. A variety of image registration algorithms exist that estimate and correct for the alignment differences between two images. These techniques can be divided into two main classifications: direct (pixel-based) alignment and feature-based registration. The methods that fall into these two classifications focus on the registration of a pair of images; an extension of these methods, referred to as global registration, focuses on aligning sets of images to minimize the total mis-registration.

2.6.2.1 Direct (pixel-based) Alignment

Direct methods align two image to produce the best match between the values of the pixels in each image. To determine what constitutes the best match, error metrics are established. These metrics include the sum of squared differences (SSD), weighted or windowed SSD (WSSD), sum of absolute differences (SAD), median of absolute differences (MAD), root mean squared (RMS) intensity error, bias and gain (BG)

error, and normalized cross-correlation (NCC). Typically, the error metric being used depends on the nature of the data and of the registration operation as described in Section 2.6.1. In general, direct alignment methods do not allow for subpixel registration; however, subpixel registration can be achieved by performing the image registration in the Fourier domain or by using an incremental refinement method.

2.6.2.2 Feature-Based Registration

Feature-base image registration is a two-part operation that first extracts distinctive features from each image in the registration pair and then aligns the extracted features. The feature extraction required for alignment makes these methods more complicated than direct alignment methods. Features identified by these methods are often referred to as keypoints, interest points, or salient points in the literature. Common feature detectors are corner detectors, blob detectors, and affine-invariant detectors. Features are typically identified by contour-based methods that identify features by examining image changes along curves, by intensity-based methods that use various forms of correlation or auto-correlation, or by parametric model-based methods that use an analytical model to approximate the image and features are detected based on the parameters of the approximation [93, 94].

Once the key features have been identified, feature matching is performed to identify the correspondence between the features in the two images. For registration of images containing simple features such as in rectified stereo pairs, several of the techniques and error metrics used for direct alignment such as SSD or NCC can be applied. Also incremental matching can be used to improve the feature matching in cases where features points are not exactly located, however, it can be time consuming and depending on the feature matching algorithm may decrease performance. For more complicated features, feature matching can be accomplished simply using a

exhaustive search; however, the computation for an exhaustive search grows quadratically with the number of features and is therefore infeasible for large numbers of features. More computationally efficient methods include: (1) rapid indexing and matching, which is based on finding nearest neighbors in high-dimensional spaces, and (2) random sample consensus (RANSAC) and least median of squares (LMS), which select a random subset of correspondences, perform motion estimation, and then update the estimation using a set number of random correspondences.

After the correspondence between the features in the two images being registered has been identified it can be used to estimate the motion transformation that best registers the two images. For motions that are linear operations, such as translation, similarity, and affine transformations, a simple least squares solution, either weighted or unweighted, can be used to identify the unknown transformation. For nonlinear motion, such as the projective transformation, more complicated estimation techniques like homography updating are required [91, 92].

2.6.2.3 Global Registration

The direct and feature-based alignment methods described in Sections 2.6.2.1 and 2.6.2.2 are limited to the alignment of pairs of images and not larger sets of images, which are the focus of global registration methods. The first type of global registration, bundle adjustment, is an extension of the image pair methods that simply aligns additional images to the previous ones in the collection. The second and better method is to simultaneously align all the images using a least squares framework or by optimizing over some error function. Often the least squares framework can be optimized with the same error metrics used for the direct alignment methods extended to multiple images.

2.6.3 Image Registration for Baseline Subtraction

Exploiting the assumption that the scattered waves resulting from a defect are small, the second of two wavefield measurements can be treated as a linear transformation of the first. Under this assumption the alignment wavefield images for baseline subtraction is closer to the registration of video frames than it is to the alignment of a collection of images. Typically, video registration algorithms are concerned with (1) moving object detection, tracking, and classification [95], (2) video to site-model registration [96], (3) video georegistration [97, 98] or (4) frame-by-frame registration [99]. The frame-by-frame registration of video is traditionally used as a stabilization technique to minimize effects of camera motion and not as a means to align images to the degree necessary to facility baseline subtraction of wavefield images.

As a technique, the alignment and subtraction of wavefield images is similar to digital subtraction angiography (DSA), a medical technique used to study the flow of blood in vessels [100]. DSA uses a set of X-ray images prior to the introduction of a contrast medium, where blood vessels are not visible, as a mask that is subtracted from the images containing the contrast medium to improve the visualization of the blood vessels. The voluntary or involuntary patient motions during the X-ray acquisition make aligning angiograms difficult, especially considering that the human tissues move non-rigidly. Fortunately, the alignment of wavefield images can be performed using only simple transformations.

There are several properties of the wavefield data that makes registration simpler than for either DSA or video. In video frames and to a lesser extent angiograms, the pixel values are arbitrary functions of brightness and viewing angle; however, in wavefield images the pixel values correspond to a physical measure of displacement. As a result, direct-alignment methods are much more effective at aligning wavefield images than feature-based methods. Second, because the laser vibrometer is mounted on a fixed scanning stage wavefield images do not suffer from projective and rotation

transformations that are common in video frames due to camera motion. The properties of wavefield data allow techniques similar to direct global registrations method to be used to find a globally consistent set of alignment parameters to minimize the mis-registrations between the two sets of wavefield measurements over all frames.

2.7 Research Context and Objectives

The literature review shows that wavefield imaging has been applied to a wide array of applications including the measurement of angle-beam waves in pipes [5], outlined in Section 2.4; however, it has not been used to rigorously study the propagation and scattering of angle-beam waves in plates. The study of angle-beam propagation in plates is of interest to a variety of industries because angle-beam techniques are one of the preferred methods of NDE used in industry. Second, analysis techniques for wavefield data are generally limited to the Fourier and Radon transforms, outlined in Section 2.5, or are application specific and do not lend themselves well to studying angle-beam scattering from defects. Using wavefield imaging to study angle-beam scattering requires not only developing new analysis methods, but also understanding how the properties of angle-beam waves culminate in different analysis methods.

The main purpose of this work is to obtain and study angle-beam wavefield data; data that can be used to gain a better understanding of angle-beam propagation, improve ultrasonic NDE, and for more rigorous model validation. First, this work presents a reliable means for high-resolution measurement of angle-beam wavefields in plates. Then a framework for the analysis of angle-beam wavefield data is described and used to study angle-beam propagation in undamaged plates. Next, a method for characterizing scattering behavior by isolating scattered waves from full wavefield data via baseline subtraction is discussed and its performance quantified. Lastly, a method for generating angle-beam scattering patterns from wavefield data is described and used to analyze scattering from notches emanating from a through-hole.

CHAPTER III

EXPERIMENTAL METHODOLOGY

This chapter presents an experimental methodology used to acquire high-fidelity ultrasonic bulk wavefield data including a discussion of the relevant experimental parameters, the rationale for the selected parameters, and the trade-offs in the selection of experimental parameters. The chapter concludes with a summary of the experimental data used throughout the remainder of the thesis.

3.1 Experimental Setup

Initial wavefield measurements were performed to determine parameters for subsequent experiments. An angle-beam probe consisting of an off-the-shelf wedge (Olympus part number ABWM-4T-70) and a 5 MHz, 6.35 mm diameter transducer (Olympus part number C543-SM) was mounted on a 6061 aluminum plate with dimensions of 610 mm $\times$ 610 mm $\times$ 6.35 mm. The wedge was designed to generate shear vertical waves with a refracted angle of 70° in steel, which corresponds to 65.2° in aluminum. The probe was liquid coupled to the plate using Sonotech Pyrogel ultrasonic couplant and was secured with adhesive mounts and plastic ties. It was located on the centerline of the plate 205 mm from one edge, and was oriented so that outward waves propagated towards the opposite edge of the plate. A diagram of angle beam wave propagation in a plate can be seen in Figure 4, which shows the center line of the ultrasonic beam as it exits the transducer, propagates as a longitudinal wave through the wedge, refracts and mode converts into a shear-vertical wave at the wedge-plate boundary, and propagates two V-paths before it is received; the V-path refers to one cycle of the wave traveling from the top surface of the plate, reflecting off the bottom surface of the plate, and returning to the top surface.

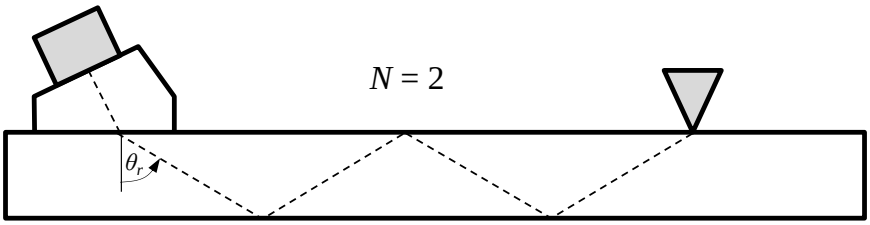

Figure 4: Illustration of the angle-beam propagation trajectory to a point receiver for a refracted angle of θ_r and two skips.

Initially, two excitations were considered: a spike excitation using a Panametrics (Olympus) model 5058PR pulser-receiver, and a chirp excitation using an arbitrary waveform generator amplified by a Ritec RAM-5000 gated amplifier. The 5058PR generates a typical negative spike whose amplitude can be adjusted from 100 to 900 V. The chirp was a linear frequency-modulated sine wave from 1-10 MHz with a duration of 180 μs and an amplitude of 200 Vpp. This chirp duration was selected to fall within the 200 μs gate window of the RAM-5000.

Wavefield measurements were obtained using a single point Polytec laser fiber vibrometer, model OFC-551, controlled by a Polytec vibrometer controller, model OFV-5000. The Polytec laser vibrometer has a laser spot size of 16 μm, resulting in minimal spatial averaging of the measured wave motion. The laser vibrometer's fiber optic sensor head was mounted on an XYZ scanning stage, which was programmed via custom LabView$^{\text{TM}}$ software to move in a point-to-point raster pattern. The output of the vibrometer controller was bandpass filtered between 1-10 MHz with a Panametrics (Olympus) model 5072PR pulser-receiver, and then subsequently digitized with a Cleverscope model CS328A digital oscilloscope at a sampling frequency of 100 MHz.

3.1.1 Sampling Considerations

Wavefield measurements sample the surface displacement of the plate in both time and space; considerations must be given to both the temporal and spatial sampling

intervals. The temporal sampling interval is chosen based on the bandwidth of the received signal. The received signal is filtered to 10 MHz prior to sampling and requires a sampling interval of at least 20 MHz. To avoid jitter in the measurements and minimize error, the sampling rate was increased to 100 MHz. The spatial sampling interval is chosen based on the maximum wavenumber of the propagating waves in the plate. The maximum wavenumber is bounded by

$$k = \frac{f_{max}}{c_{min}}, \tag{9}$$

where f_{max} is the maximum frequency of the propagating wave and c_{min} is the minimum of the propagating wave velocities. Based on the maximum frequency of the input signal and the slowest propagating wave, the Nyquist sampling interval is

$$\Delta x = \frac{c_{min}}{2f_{max}}. \tag{10}$$

The frequency spectrum of the input, a linear frequency-modulated sine wave from 1-10 MHz, has a maximum frequency component of 10 MHz. The slowest propagating wave mode in the aluminum plate is the Rayleigh wave, which propagates at a velocity of 2.90 mm/μs. Substituting these quantities into Eq. 10 gives a Nyquist sampling interval of 0.15 mm.

3.1.2 Excitations, Averaging and Noise Reduction

Laser vibrometer wavefield measurements are sensitive to both temporal and spatial noise, particularly at the frequencies of interest for bulk wave inspection. Both types of noise can be effectively reduced by signal averaging, but the trade-off is increased acquisition time. For guided wavefield measurements, it is typical to use reflective tape to increase signal amplitudes and thus increase the signal-to-noise ratio (SNR) [101], particularly for a scanning laser vibrometer, and the use of a reflective tape is considered in this study. Another approach to increase the SNR is to use a broadband

excitation such as a linear frequency modulated (LFM) chirp excitation and post-process the received signals. Here the processing was performed via deconvolution as described in [102] and various target waveforms were considered. Signals were bandpass filtered after deconvolution by multiplication in the frequency domain with a tapered cosine window from 0 to 10 MHz with a taper width on each end of 1 MHz (20% Tukey window [103]). This technique yields the equivalent response to the target excitation but with a higher SNR because of both the larger energy of the chirp and the additional filtering.

The left side of Figure 5 shows four signals obtained from the 65.2° wedge and 5 MHz transducer (referred to as a probe) at a distance of 50 mm, referenced from the point where the center of the beam exits the wedge, i.e., the incident point or probe index; each signal was normalized to the peak of its absolute value. For Figure 5(a), the excitation was a 400 V spike and 16 averages were taken to reduce incoherent noise. Figure 5(b) is the corresponding signal using a chirp excitation and is shown after deconvolution to an impulse; it is essentially identical to that of Figure 5(a) but with an improved SNR. Although not shown here, increasing the number of averages for the spike to 512 yielded a SNR similar to that achieved with the chirp using 16 averages. It is common in guided wavefield acquisition to apply reflective tape to the testing surface to improve the quality of the laser signal. Figure 5(c) shows an undesirable distortion and reduction in amplitude caused by adding such reflective tape; the excitation and processing were the same as for Figure 5(b). Figure 5(d) was computed from the same measured signal as Figure 5(b) but the deconvolution target was a 5 MHz, 2 cycle, Hann-windowed tone burst. The resulting center frequency is higher than that of Figures 5(a) and 5(b), which is manifested in the improved resolution of the three arrivals between 21 and 24 μs.

Another important advantage of the chirp excitation, or any broadband excitation, is that various target signals can be investigated during post-processing. The right

side of Figure 5 shows processed chirp responses for the same measured signal as Figure 5(b) for 2 and 5 cycle tone bursts at 2 and 8 MHz. Clearly the ability to discriminate and identify the various arrivals is strongly dependent upon the frequency and number of cycles. As compared to the other signals in Figure 5, the 5 MHz, 2 cycle target signal of Figure 5(d) offers improved separation of arrivals, has a comparable SNR, and minimizes lower frequency clutter; this target signal is used for the rest of the data reported in this work.

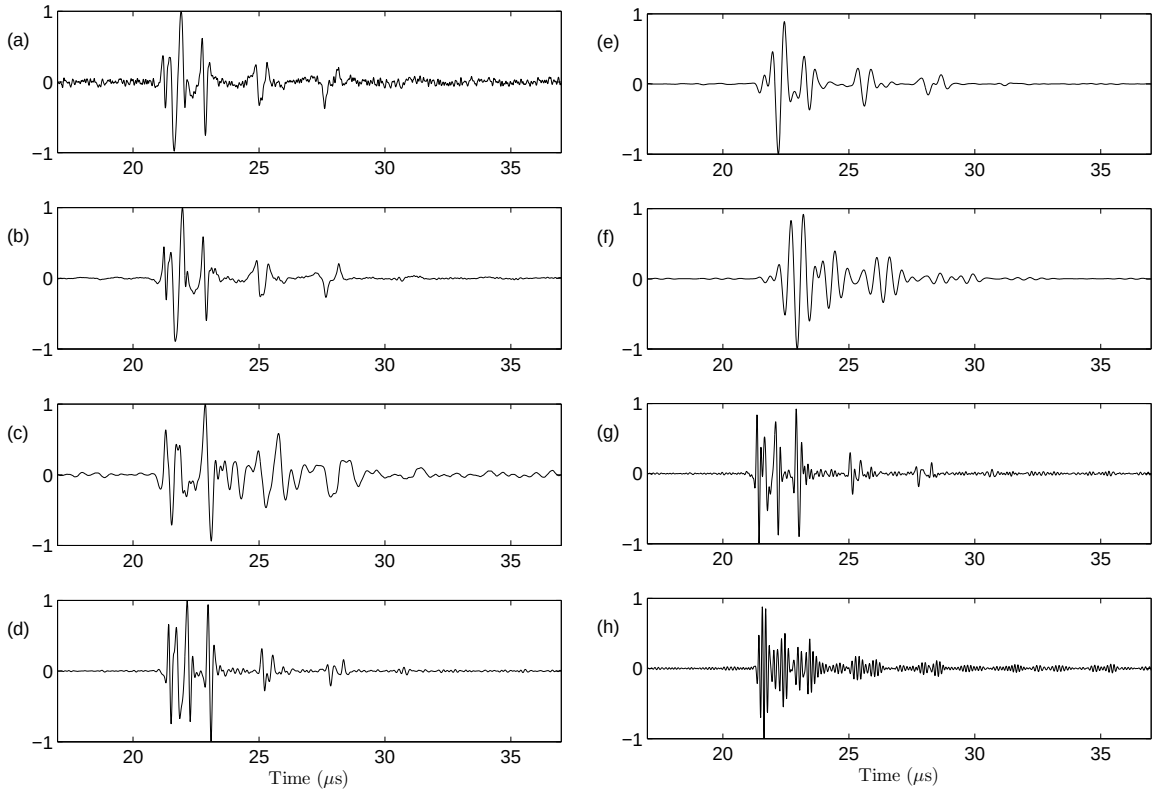

Figure 5: Signals recorded at a distance of 50 mm from the 65.2° probe. (a) 400 V spike excitation, 16 averages. (b) 200 V chirp excitation, 16 averages, deconvolution to an impulse. (c) 200 V chirp excitation, 16 averages, deconvolution to an impulse, with reflective tape. (d) 200 V chirp excitation, 16 averages, deconvolution to a 5 MHz, 2-cycle Hann-windowed tone burst. (e) 2-cycle, 2 MHz, Hann-windowed tone burst. (f) 5-cycle, 2 MHz, Hann-windowed tone burst. (g) 2-cycle, 8 MHz, Hann-windowed tone burst. (h) 5-cycle, 8 MHz, Hann-windowed tone burst.

3.1.3 Trade-offs in Experimental Parameters

Practical measurement systems involve trade-offs between the quality of the acquired data and the acquisition time. In practice, the acquisition of wavefield measurements is heavily dependent on the measurement setup; however, there are generalities that can be made. The acquisition time, t_a, for a single point in the wavefield is related to the number of averages, N_{avg} and the pulse repetition interval, PRI of the transmitted signal,

$$t_a = N_{avg} PRI. \tag{11}$$

The PRI is chosen based on the power limits of the amplifier and transducer and to minimize wrap-around in the measurements. The number of averages is restricted by the specifications of the measurement system. For the Cleverscope Model CS328A digital oscilloscope used here, the maximum number of on-board averages is 128 and the maximum number of samples is 4 million. The Cleverscope performs waveform averaging by dividing the maximum number of samples amongst the frames to be averaged, which gives the maximum number of samples that can be taken for a particular number of averages. For example, at 128 averages the length of the measurement would have to be less than 31,250 samples.

In addition to trade-offs in the measurement time, there are also trade-offs related to the scanner motion between the measurement points. There is a trade-off between the velocity of the scanner motion, the dwell time prior to measurement, and the data quality. Faster motion between measurement points comes at the expense of measurement quality unless the dwell time prior to measurement is increased to allow for the laser to stabilize. In general, the selection of the scanner velocity and dwell time must be done empirically because of differences between the motion control and lasers in different systems. The importance of motion and dwell time selection increases as the scan area and measurement interval increases as a result of the larger

distance between scan points.

Combining the considerations for the scanner motion as well as the measurement time per scan point, the total scan time, $t_{s,Total}$, can be estimated as

$$t_{s,Total} = N_p(N_{avg}PRI + t_m + t_d) + t_i, \tag{12}$$

where N_P is the total number of scan points, t_m is the motion time between two scan points, t_d is the dwell time at each point, and t_i is a constant initialization time for each scan.

3.2 Summary of Experiments

Once the experimental setup and parameters were finalized, data sets were acquired that are used throughout this work. The first sets of data are line scans, i.e., the scan was performed along a line in the direction of propagation moving away from the transducer. These scans were performed to study the angle-beam wave propagation characteristics and the effect of refracted angle on those characteristics. The line scan experiments were performed on the 610 mm × 610 mm × 6.35 mm aluminum plate used in the initial experiments. The plate was excited with the Olympus Model C543 transducer used in conjunction with ABWM-4T-45°, ABWM-4T-60°, or ABWM-4T-70° wedges. The line scans are summarized in Table 2 and the respective B-scans can be seen in Figure 6 .

Subsequent wavefield data reported here, which are all area scans obtained for the purpose of studying scattering, were acquired on a 305 mm × 305 mm × 6.35 mm, mirror-finish, aluminum plate using the chirp excitation followed by post-processing to a 5 MHz, 2 cycle, Hann-windowed target signal as previously described. The mirror finish was selected to provide a higher SNR with fewer averages since reflective tape was found to produce significant signal distortion. A 6.35 mm diameter through-hole was drilled in the plate, and 45° corner notches were subsequently introduced on the

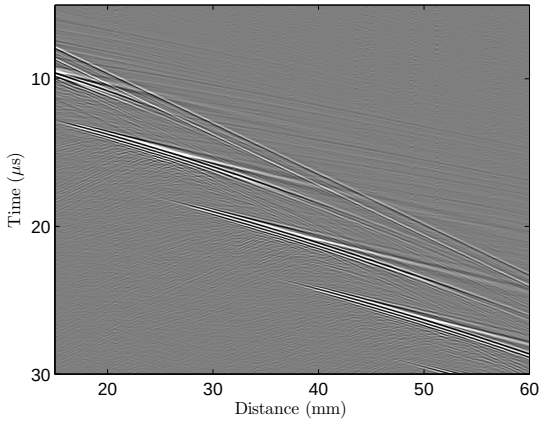

(a) Refracted angle of 43.1°

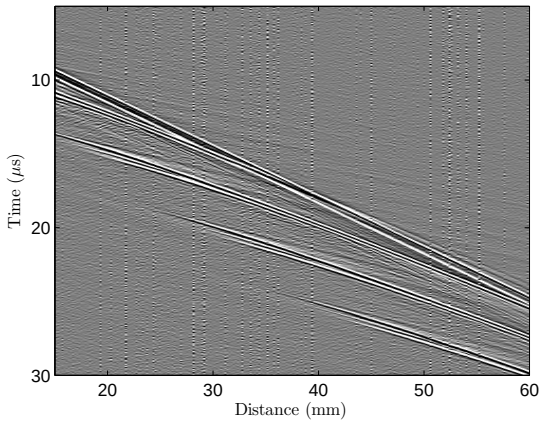

(b) Refracted angle of 56.8°

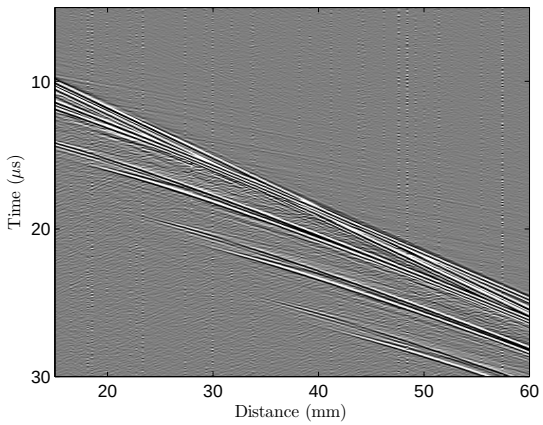

(c) Refracted angle of 65.2°

Figure 6: B-scans for the three different wedge angles: (a) 43.1°, (b) 56.8°, and (c) 65.2°.

far side of the plate at an angle of 0° relative to the hole. The same 5 MHz transducer was installed on a wedge designed to generate a 60° shear wave in steel (Olympus part number ABWM-4T-60), which corresponds to 56.8° in aluminum. This probe was mounted to the plate in the same manner as previously described at a distance of 32.5 mm from the hole, which corresponds to 1.5 skips, and at an angle of −90°. A second transducer was mounted at the same distance of 1.5 skips at a angle 45° relative to the notch. A diagram of the area scans experiments can be seen in Figure 7. The diagram depicts the front and side views of the angle-beam propagation for the −90° orientation, which includes the beam path. Also depicted is the top view of the experimental setup, which includes both the −90° and 45° transducer orientations.

Multiple scans were performed over a 30 mm × 30 mm area at a spatial resolution of 0.25 mm as summarized in Table 2. All scans were recorded under typical laboratory conditions at nominally the same temperature; although not measured, it is estimated that the temperature changed no more than ±2° during and between scans. Note that the first set of area scans (#4-8) were all recorded over a one-week period, the differences being the addition and enlargement of the corner notch. The next three scans (#9-11) were recorded about 1 month after the first three with no changes in the scatterer; the purpose of these last three scans was to investigate baseline subtraction performance on nominally identical wavefields. The final five scans (#12-16) were recorded over the same week period as scans #4-8. They are identical to scans #4-8 except the transducer is at an angle of 45° to the notch to allow for the scattering from more than one incident angle to be studied.

Although the calculated Nyquist spatial sampling interval, based on the slowest propagating wave velocity, was 0.15 mm at 10 MHz, recorded data using the 5 MHz transducer manifests in minimal spatial aliasing at 0.25 m. This spacial increment was used and the scan time was significantly reduced. The temporal sampling frequency was set to 100 MHz to reduce measurement jitter and the time window acquired

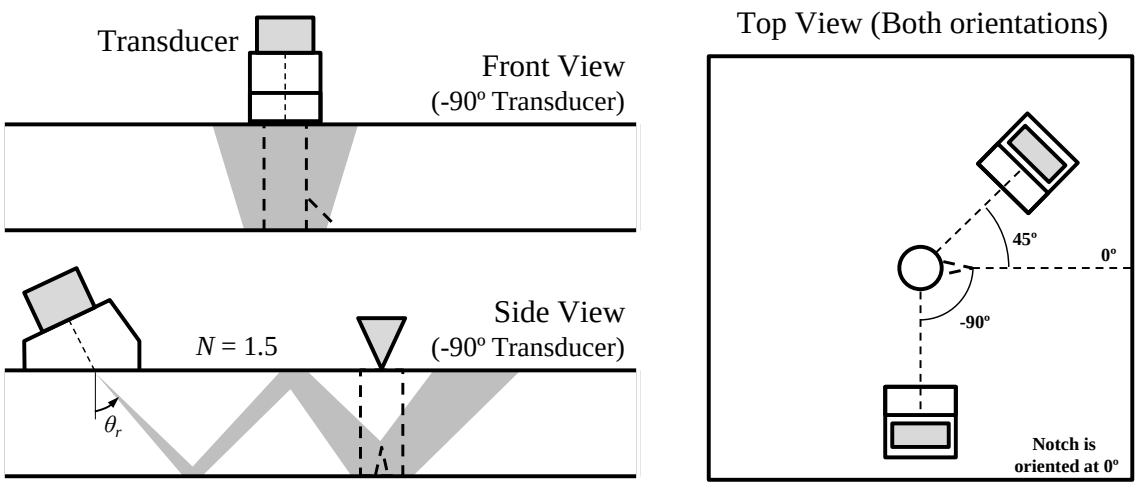

Figure 7: Illustration of the angle-beam transducer configuration for the area scan experiments.

was 400 μs, which after chirp deconvolution resulted in signals 200 μs in length. The surface finish of the aluminum plate improved the SNR so that only four averages were performed. The resulting scan time was approximately 1.1 seconds per scan point, which translates to a total scan time of roughly 3.5 hours for the 30 mm $\times$ 30 mm region. The limiting factor in the acquisition speed was the maximum allowable pulse repetition rate of the Ritec amplifier.

Wavefield snapshots for Scans #4-8 are shown in Figure 8 at times of 18, 19, and 20 μs. These images illustrate overall data quality and show scattering from the hole and notches. The incident waves encounter the hole in the following order: (1) the first shear wave skip overlapped with the Rayleigh wave, (2) the second shear wave skip, and (3) the third shear wave skip. As a note, although the shear wave velocity is higher than the Rayleigh wave velocity, the first shear wave and the Rayleigh wave overlap at distances near the hole because the shear wave travels along a longer path as it bounces between the two plate surfaces. In each case, scattering from the notch is overpowered by the incident waves and the waves scattered from the hole; scattering from the smallest 1 mm notch is barely visible.

Figure 9 shows corresponding plots of spatial energy maps and histograms for

scans. The spatial energy map of a wavefield, $w(t, x, y)$, is calculated from the total energy at each pixel referenced to the maximum energy and is expressed in dB as

$$E(x_l, y_m) = 10 \log_{10} \left(\frac{\sum_n w(t_n, x_l, y_m)^2}{\max_{i,j} \left(\sum_n w(t_n, x_i, y_j)^2 \right)} \right). \tag{13}$$

The energy map for the 1 mm notch is essentially the same as that for the no notch case, and the 4 mm notch has only a small effect on the energy map near the notch location. The snapshots and energy maps in both Figures 8 and 9 show slight asymmetry, which indicates that the transducer beam is not perfectly aligned with the through-hole. The histograms are essentially the same for all the notch sizes. Although not shown here, data from scans #9, 10, and 11 are essentially identical to those of scan #8 except for a slight spatial shift in scan #11.

For comparison, wavefield snapshots for Scans #12-16 are shown in Figure 10 at times of 16, 17, and 18 μs. The change in transducer orientation does not change the order of wave arrivals, but does change the scattering behavior. As is for the case when the transducer was oriented -90°, the scattering from 1 mm is almost invisible in the wavefield snapshots; however, scattering from the larger notches is clearly visible, especially the scattered wave propagating out along the length of the notch. Figure 11 shows corresponding plots of spatial energy maps and histograms.

Table 2: Summary of experimental wavefield data used throughout this work.

Scan Number	Scan Type	Wedge Angle	Scatterer	Description
#1	Line	43.1°	Undamaged plate	
#2	Line	56.8°	Undamaged plate	
#3	Line	65.2°	Undamaged plate	
#4	Area	56.8°	6.35 mm through-hole	Baseline through-hole scan
#5	Area	56.8°	6.35 mm through-hole with 1 mm corner notch	Plate removed to cut the notch and reinstalled
#6	Area	56.8°	6.35 mm through-hole with 2 mm corner notch	Plate removed to cut the notch and reinstalled
#7	Area	56.8°	6.35 mm through-hole with 3 mm corner notch	Plate removed to cut the notch and reinstalled
#8	Area	56.8°	6.35 mm through-hole with 4 mm corner notch	Plate removed to enlarge the notch and reinstalled
#9	Area	56.8°	6.35 mm through-hole with 4 mm corner notch	Data recorded 1 month after Scan #8
#10	Area	56.8°	6.35 mm through-hole with 4 mm corner notch	Data recorded after Scan #9 without remounting the plate
#11	Area	56.8°	6.35 mm through-hole with 4 mm corner notch	Data recorded after Scan #10 after removing and remounting the plate
#12	Area	56.8°	6.35 mm through-hole	Identical to Scan #4 but wedge 45° to notch
#13	Area	56.8°	6.35 mm through-hole with 1 mm corner notch	Identical to Scan #5 but wedge 45° to notch
#14	Area	56.8°	6.35 mm through-hole with 2 mm corner notch	Identical to Scan #6 but wedge 45° to notch
#15	Area	56.8°	6.35 mm through-hole with 3 mm corner notch	Identical to Scan #7 but wedge 45° to notch
#16	Area	56.8°	6.35 mm through-hole with 4 mm corner notch	Identical to Scan #8 but wedge 45° to notch

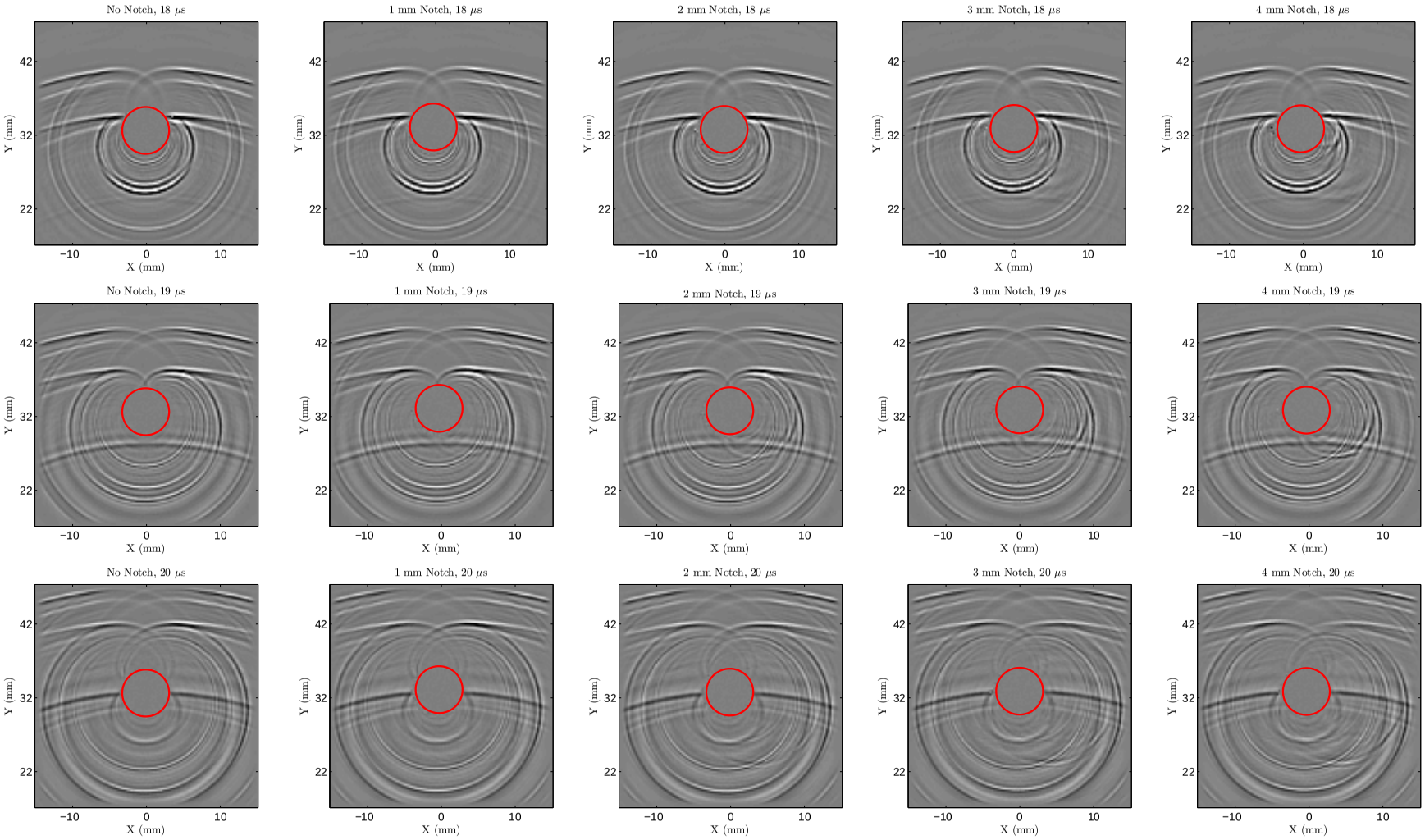

Figure 8: Wavefield snapshots of a 30 mm × 30 mm scanned area centered on a 6.35 mm through-hole at three different times (18, 19, and 20 μs) for scans #4-8. The edge of the hole is outlined in red.

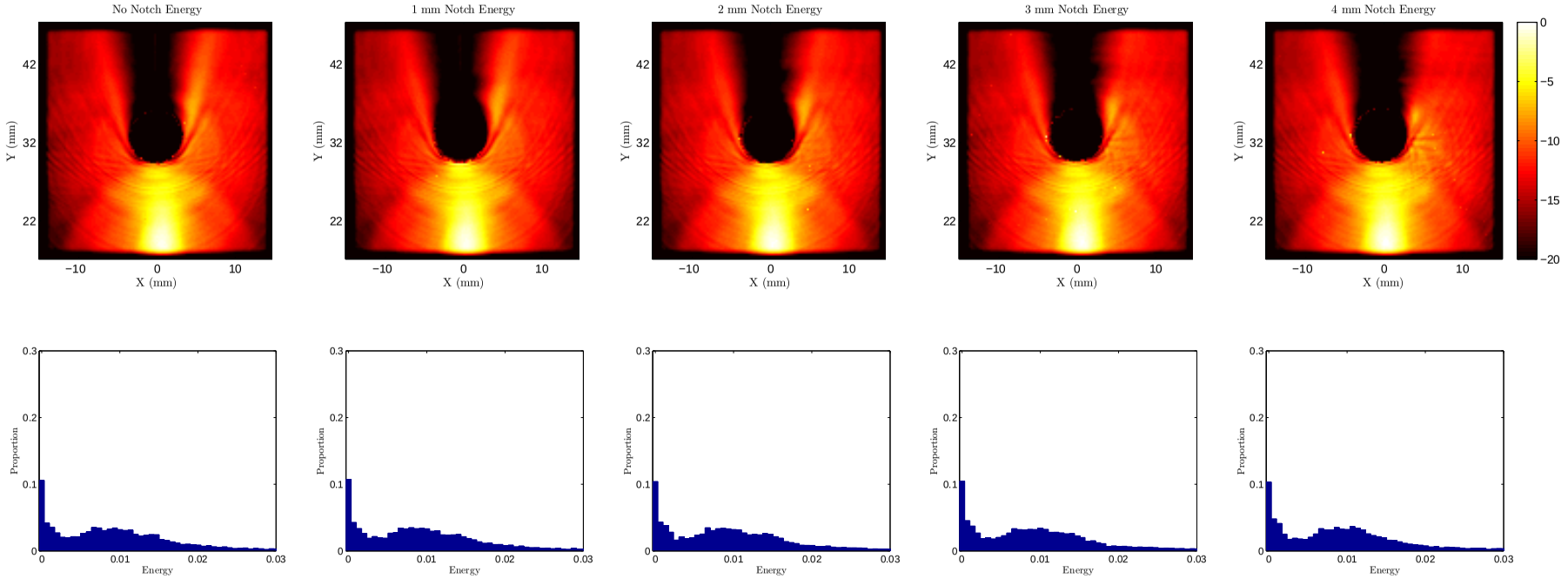

Figure 9: Globally referenced energy maps and energy histograms of the wavefield data from scans #4-8.

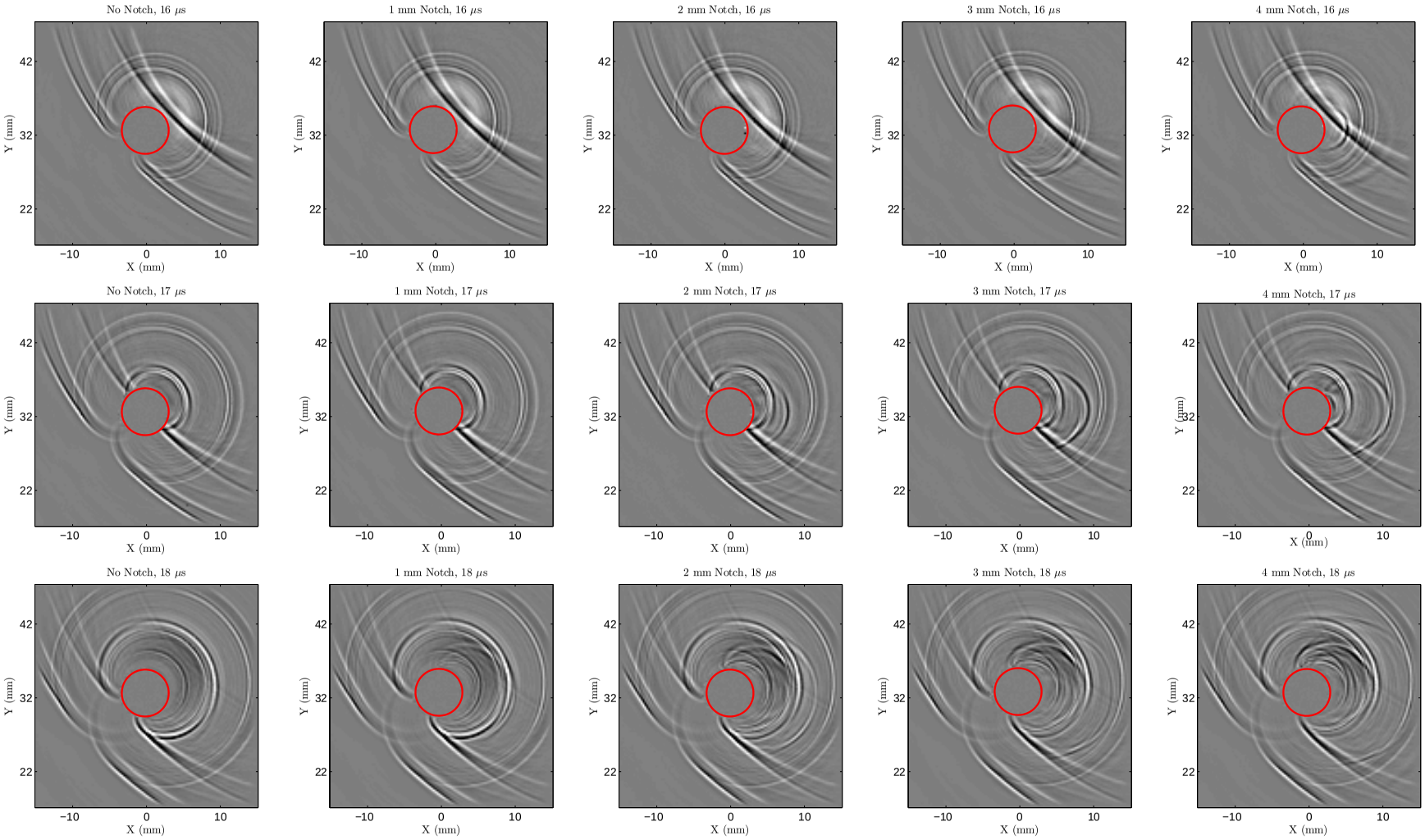

Figure 10: Wavefield snapshots of a 30 mm × 30 mm scanned area centered on a 6.35 mm through-hole at three different times (16, 17, and 18 μs) for scans #12-16. The edge of the hole is outlined in red.

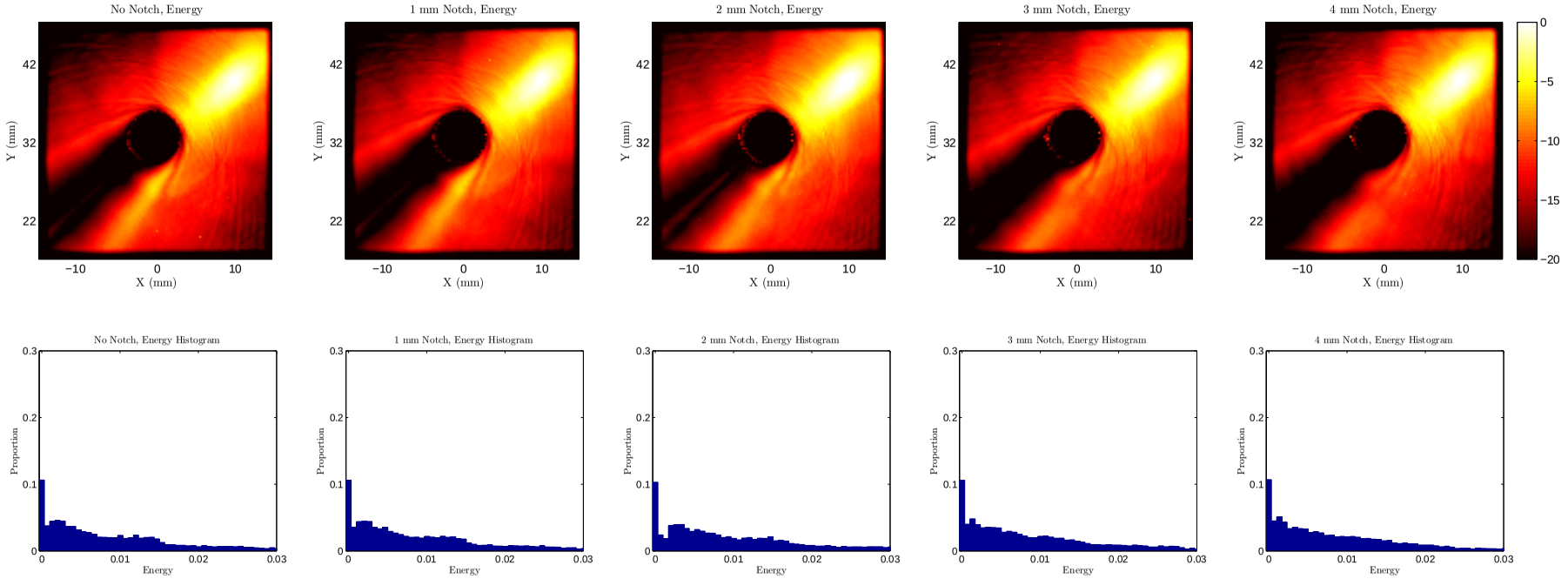

Figure 11: Globally referenced energy maps and energy histograms of the wavefield data from scans #12-16.

CHAPTER IV

CHARACTERIZATION OF ANGLE-BEAM WAVE PROPAGATION: EXPERIMENTAL AND MODELING RESULTS

Bulk waves in infinite media, as outlined in Section 2.1, are relatively simple in nature; however, the measurement and analysis of angle-beam bulk waves is complicated by the reflections of these waves between the surfaces of the plate. Understanding the nature of these reflections, commonly called skips or V-paths, is fundamental to understanding the propagating waves recorded on the surface of the plate from wavefield measurements. The purpose of this chapter is to present a simple and widely know analytical model of angle-beam wave propagation and then use that model to study the features of angle-beam wave propagation in scatterer-free plates by characterizing and comparing results from experimental data and a 2-D finite element model .

4.1 Simple Analytical Propagation Model

Angle-beam bulk waves reflect between the surfaces of the plate and are measured on the surface of the plate; a simple ray-tracing model [104] can be used to relate the 2-D wavefield measurements and 3-D propagation characteristics. The reflection of the angle-beam bulk waves between the two surfaces of the plate is referred to as a V-path. When measured on the surface of the plate, as in wavefield imaging, angle-beam bulk waves propagate along a hyperbolic trajectory in space-time, as displayed in the B-scan. The path function, $g(r)$, for a angle-beam shear wave, which is also

the V-path distance, along the direction of propagation is

$$g(r) = \sqrt{r^2 + (2Nh)^2}, \tag{14}$$

where r is the measurement distance (along the surface) referenced to the incident point, N is the number of skips, and h is the plate thickness. The arrival times of a wave propagating along a particular V-path, $g(r)$, at a particular measurement distance, r, is

$$t_a = \frac{g(r)}{c} + t_0, \tag{15}$$

where c is the velocity of the propagating waves and t_0 is the time offset which accounts for the propagation time through the angle-beam wedge and delay resulting from wave generation mechanisms. Because the angle-beam waves propagate at an angle within the medium, the velocity measured on the phase velocity measured on the surface of the plate,

$$c_p = c/\sin\theta_r, \tag{16}$$

is a function of the refracted angle, θ_r, and the wave velocity, c. Figure 12 provides a graphical representation of the interaction of the wavefronts with surface of the plate and the resulting phase velocity. Since the magnitude of the sine function is bounded from 0 to 1, the lower bound of the phase velocity is either the shear (c_s) or longitudinal (c_l) wave velocity depending on the wave mode. There is no upper bound on the phase velocity, which can lead to ambiguity between the wave modes for different combinations of refracted angles.

Although angle-beam bulk waves are often presented as propagating along a specific ray trajectory determined by their nominal refracted angle, as seen in Figure 13(a), the nature of bulk wave propagation is more complex. Bulk waves do not propagate in an infinitely narrow beam; thus, it is more accurate to describe bulk wave propagation in terms of a range of refracted angles and fixed number of

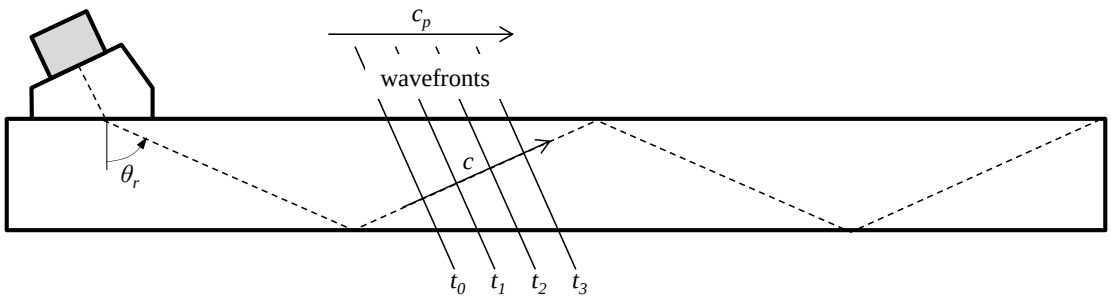

Figure 12: Illustration of the relationship between the wave velocity, c, and the phase velocity, c_p, for angle-beam wave propagation.

skips. Although Eq. 15 does not explicitly include the refracted angle, θ_r, or the beam width, an arrival is only present if the beam path falls within the beam width of the transducer. Larger amplitude arrivals correspond to beam paths centered about the nominal refracted angle. The skip distance, d, measured along the surface of the plate where a wave breaks the surface is a function of the refracted angle, θ_r, the number of skips, N, and the thickness of the plate, h,

$$d = 2Nh \tan \theta_r. \tag{17}$$

Substituting the skip distance from Eq. 17 in for r in the arrival time equation, Eq. 15, gives an expression that characterizes the shear wave arrivals in the B-scan as a function of the refracted angle,

$$t_a = \frac{2Nh}{\cos(\theta_r)c} + t_0. \tag{18}$$

In effect angle-beam bulk waves propagate as function of the refracted angle due to the beam width of the transducer [7]. Figure 13(a) gives a graphical representation of the skip patterns for a range of refracted angles, which can be used to understand the wave behavior at the surface. Figure 13(b) plots the hyperbolic arrival time curves, given by Eq. 15 with 5 skips for an angle-beam wave propagating at a refracted angle 56.8° of in a 6.35 mm thick plate.

In addition to the propagating shear wave skips, a Rayleigh wave is also generated

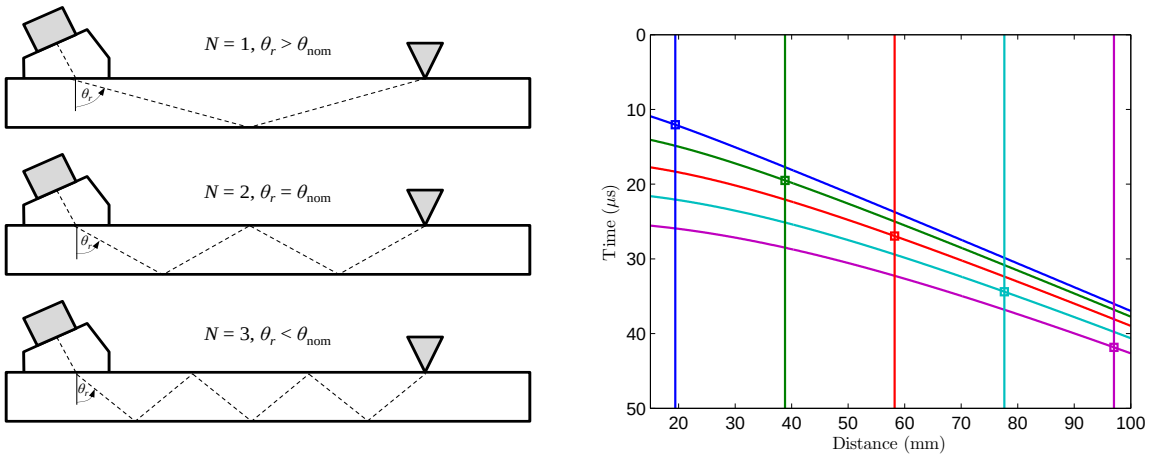

(a) (b)

Figure 13: Theoretical angle-beam bulk wave propagation (a) diagram and (b) shear wave arrival time curves for a refracted angle of 56.8° and N = 1, 2, 3, 4, and 5 skips.

by the angle-beam wedge and it propagates along the surface of the plate. Since the Rayleigh wave propagates along the surface and not along a V-path, it's path function,

$$g(r) = r, \tag{19}$$

is much simpler than for the shear and longitudinal waves.

4.2 Experimental Measurements

To study the features of angle-beam wave propagation in scatterer-free plates, the B-scans measurements for the 43.1°, 56.8°, and 65.2° wedge transducer configurations were compared to the theoretical wave propagation behavior in the x-t domain, summarized in Section 4.1. Two Rayleigh waves are present in the B-scan for each refracted angle; theoretical Rayleigh wave arrival times were calculated from Eq. 15 using the linear path function from Eq. 19. Theoretical shear wave arrival times were calculated from Eq. 15 using the hyperbolic path function from Eq. 14 for up to 5 skips; i.e., N=1,2,...,5. The nominal Rayleigh and shear wave velocity in aluminum were used for plotting the arrival time curves and are 2.902 mm/μs and 3.114 mm/μs, respectively. The Rayleigh wave velocity is calculated using the

approximation from [20],

$$c_R = \frac{0.87 + 1.12\nu}{1 + \nu} c_s, \tag{20}$$

where ν is Poisson's ratio (0.32 for aluminum) and c_s is the shear wave velocity. Table 3 summarizes the wave velocities measured on the surface of the plate and the time offsets, t_0, used in Eq. 15 for each angle and wave type. Time offsets were calculated based on the travel time through the wedge and then adjusted to account for inaccuracies in the velocity to produce the best match with the experimental curves. The time offset for the second Rayleigh wave and the shear waves is the same, which suggests that these waves are generated simultaneously, whereas the first Rayleigh wave is either generated earlier or closer to the front of the wedge.

Table 3: Summary of phase velocities measured on the surface of the plate and time offsets, t_0, used in Eq. 15 to generate theoretical arrival time curves.

	Wedge Angle		
	43.1°	56.8°	65.2°
Rayleigh Wave Velocity (mm/μs)	2.902	2.902	2.902
Shear Wave Phase Velocity* (mm/μs)	4.56	3.72	3.43
Time offset (μs) for 1st Rayleigh wave	2.6	4.0	4.8
Time offset (μs) for 2nd Rayleigh wave	3.4	4.6	5.3
Time offset (μs) for shear waves	3.4	4.6	5.3

*Calculated from Eq. 16.

Figure 14 shows the comparison of these theoretical arrival time curves and the B-scan for all three refracted angles for both the Rayleigh (Figure 14(a), 14(c), and 14(e)) and shear waves (Figure 14(b), 14(d), and 14(f)). Comparison of the theoretical arrival time curves and the propagating shear waves are in good agreement for all three

wedge angles. The slight differences can be explained by minor inaccuracies in the wave velocities and offsets.

As can be seen by Eq. 14, the theoretical travel time curves for the shear waves follow hyperbolic trajectories. The asymptotic nature of these curves as the distance approaches zero corresponds to normal incidence shear waves reflecting back and forth through the thickness, which cannot happen physically because of the non-zero incident angle. From Figure 14, it can be seen that the shear wave for each skip, regardless of refracted angle, follow the same hyperbolic trajectories, however the refracted angle changes the nature of the waves in two ways. Both the skip distance, given by Eq. 17, and the waves visible window about the skip distance increases as a function of the refracted angle.

In addition to the propagating shear waves, the B-scan also reveals two propagating Rayleigh waves, which will be referred to as a Rayleigh wave doublet. Theoretically, Rayleigh waves should only be present for refracted angles that are greater than the second critical angle. The second critical angle, θ_{c2}, can be calculated from Snell's Law,

$$\theta_{c2} = \sin^{-1} \frac{c_l}{c_s}, \tag{21}$$

where c_l is the longitudinal wave velocity in the first medium and c_s is the shear wave velocity in the second medium. For the refraction between the acrylic wedge and aluminum plate, the second critical angle is 48.7°. The presence of such a strong Rayleigh wave is surprising since the incident angles (31.2°, 39.3°, and 43.4° for the 43.1°, 56.8°, and 65.2° refracted angles, respectively) of all three wedges is less than the second critical angle. The existence of the propagating Rayleigh wave doublet is thought to arise from the finite extent and the beam spread of the 6.35 mm diameter transducer as well as from wave interactions at the interface between the wedge and the plate. The magnitude of the Rayleigh waves decreases as the difference between

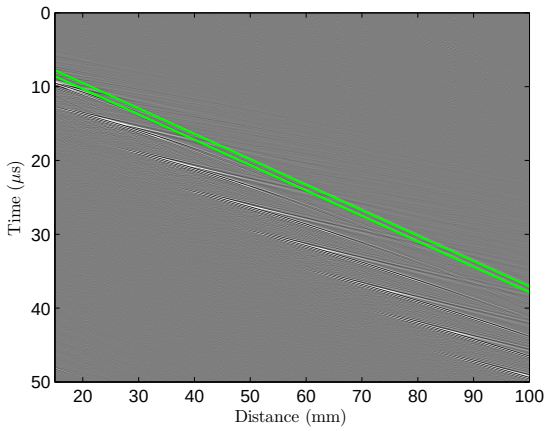

(a) Refracted angle of 43.1°: Rayleigh Waves

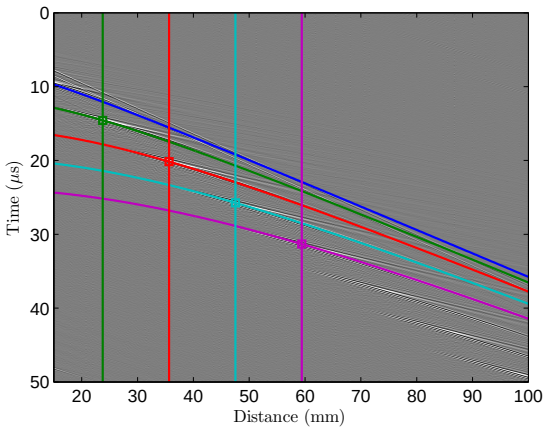

(b) Refracted angle of 43.1°: Shear Waves

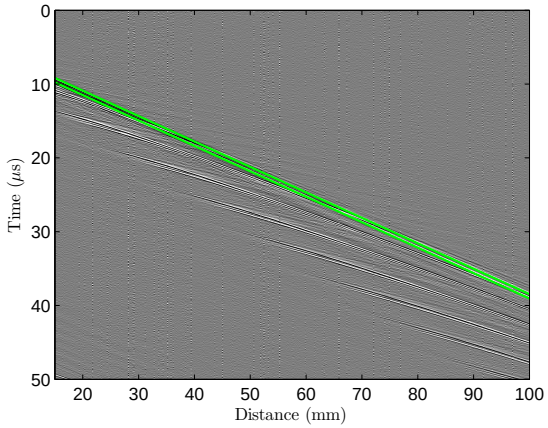

(c) Refracted angle of 56.8°: Rayleigh Waves

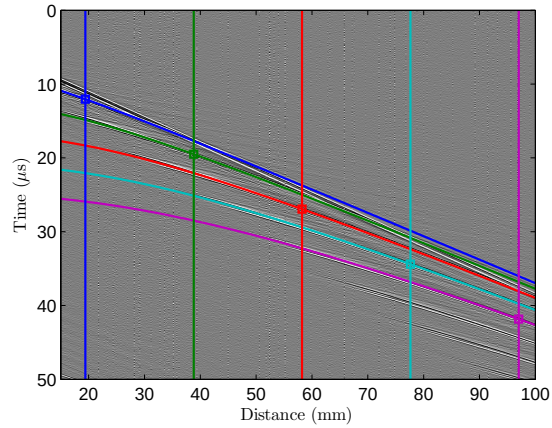

(d) Refracted angle of 56.8°: Shear Waves

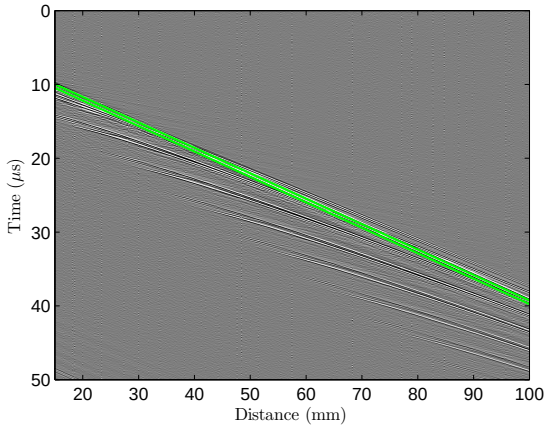

(e) Refracted angle of 65.2°: Rayleigh Waves

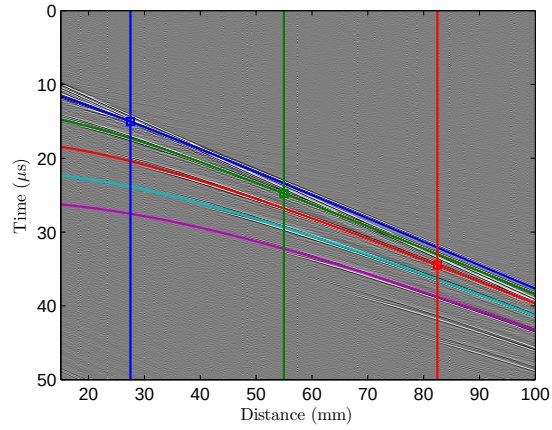

(f) Refracted angle of 65.2°: Shear Waves

Figure 14: Overlay of theoretical Rayleigh (left) and shear (right) wave arrival time curves on the B-scans for the three different wedge angles: 43.1° (top), 56.8° (middle), and 65.2° (bottom).

the refracted angle and the second critical angle increases.

In addition to using overlaid trajectories, the propagating wave modes can be identified using either the Radon transform or frequency-wavenumber analysis. The Radon transform, described in Section 2.5.2, maps straight lines in the x-t domain to points in the τ-p domain. Traditionally the Radon transform is expressed in terms of the slowness, p; however, since it is being used here to identify different wave modes it is more convenient to express the Radon transform in terms of phase velocity, i.e., in the τ-c_p domain.

The left side of Figure 15 expresses the Radon transform in terms of the phase velocity for the B-scan data of Figure 14. The Rayleigh waves propagate along linear trajectories and thus appear as localized points in the Radon transform. The shear waves do not map to points in the τ-c_p domain since their trajectories are hyperbolic in the x-t domain; instead they form a family of curves, one for each number of skips. The velocity measured on the surface of the plate and the time offsets measured by the Radon transform can be found in Table 4. Comparing the values used for the overlaid curves to those measured from the Radon transform shows good agreement for all values except for the first shear wave time offsets. The shear wave time offset measured by the Radon transform is inaccurate because the shear waves do not follow linear trajectories and thus the Radon overshoots the actual time offset. Creating a Radon transform that follows the hyperbolic trajectories of the shear waves is difficult because of the number of independent variables inherent in the hyperbolic trajectory, as seen in Eq. 14, is greater than for a linear trajectory (3 vs. 2).

Frequency-wavenumber analysis, described in Section 2.5.3, can provide similar information about the propagating wave modes as the Radon transform; however, it does not provide any temporal information about the propagating waves. The right side of Figure 15 shows the 2-D Fourier transform for the B-scan data of Figure 14. Generally, a wave propagating along a linear trajectory in the B-scan culminates as

Table 4: Summary of the phase velocities and time offsets measured from the Radon transform.

	Wedge Angle		
	43.1°	56.8°	65.2°
Rayleigh Wave Velocity (mm/μs)	2.93	2.92	2.93
Shear Wave Velocity (mm/μs)	4.54	3.71	3.43
Time offset (μs) for 1st Rayleigh wave	2.7	4.1	4.9
Time offset (μs) for 2nd Rayleigh wave	3.5	4.6	5.3
Time offset (μs) for 1st shear wave	6.4	6.9	7.1

a line of energy in the 2-D Fourier transform. The slope of this line is a function of the velocity of the propagating wave, which relates the frequency and the wavenumber as seen in Eq. 5. Since the Rayleigh wave propagates along a linear trajectory in the B-scan it culminates in the 2-D Fourier transform as a well defined line with a slope equal to the inverse of the velocity. The hyperbolic trajectory of the shear waves complicates the 2-D Fourier transform by essentially spreading the energy over a variety of velocities since the hyperbolic trajectory can be thought of as a continuum of refracted angles and thus phase velocities. The interaction of the hyperbolic trajectories of different skips produces the band of striations seen below the Rayleigh wave. This interaction complicates the velocity determination using the 2-D Fourier transform. Table 5 gives the best estimate for the phase velocity obtained by fitting a line to the peak energy at each frequency in the 2-D Fourier transform. Comparing Table 4 and 5, the Rayleigh velocity measured in the frequency-wavenumber domain is close to that obtained using the curve fitting and Radon transform methods; however, the estimate of the shear wave velocity is consistently below that of the other methods.

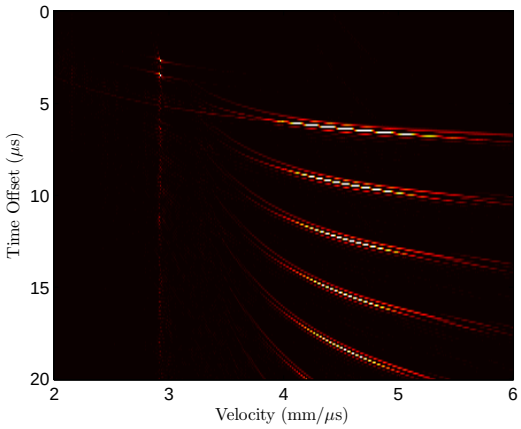

(a) Refracted angle of 43.1°: Radon Transform

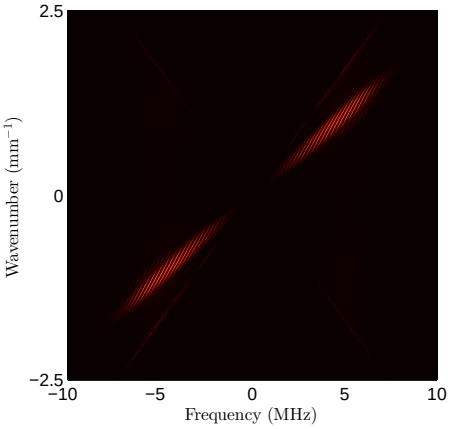

(b) Refracted angle of 43.1°: Fourier Transform

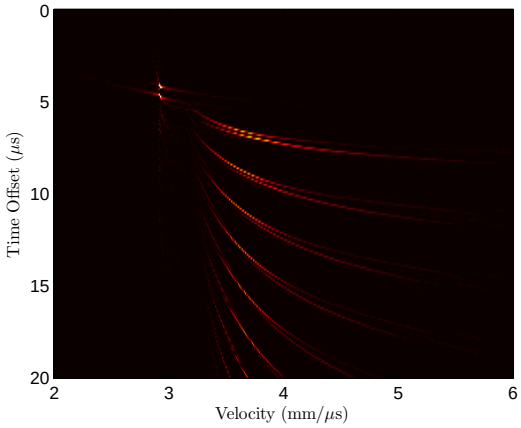

(c) Refracted angle of 56.8°: Radon Transform

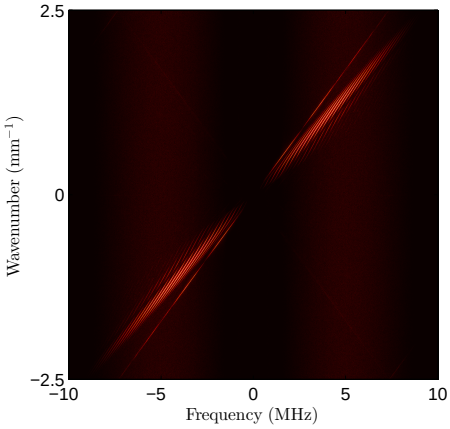

(d) Refracted angle of 56.8°: Fourier Transform

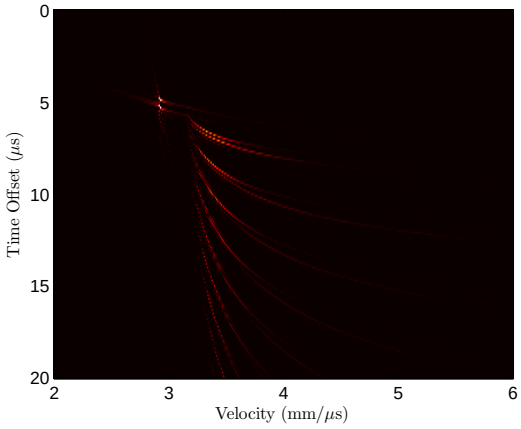

(e) Refracted angle of 65.2°: Radon Transform

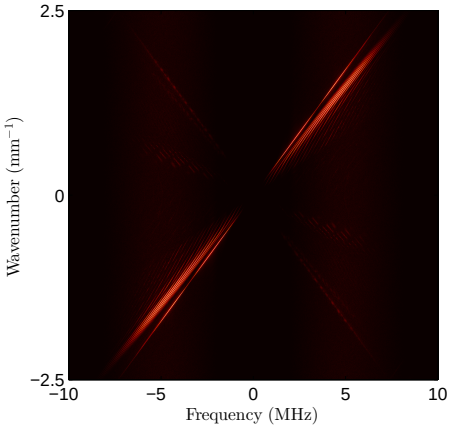

(f) Refracted angle of 65.2°: Fourier Transform

Figure 15: Radon (left) and Fourier (right) transforms of the B-scans for the three different wedge angles: 43.1° (top), 56.8° (middle), and 65.2° (bottom).

Table 5: Summary of the phase velocities measured from the Fourier transform.

	Wedge Angle		
	43.1°	56.8°	65.2°
Rayleigh Wave Velocity (mm/μs)	2.92	2.92	2.93
Shear Wave Velocity (mm/μs)	4.44	3.65	3.30

Although it is plain to see in the experimental B-scans and the wave identification method that Rayleigh waves are generated, traditional angle-beam experiments seldom acknowledge the presence of these waves. Two possible explanations for the presence of the Rayleigh wave in these measurements and its apparent absence in traditional angle-beam experiments are: (1) Traditional angle-beam measurements employ a wedge transducer both on transmit and receive; the received waveforms are scaled by the wedge effects twice. Since the wedge refracts the transducer beam down into the plate the wedge transducer is not very sensitive to waves propagating on the surface and these waves are greatly attenuated. The attenuation effect can be seen in the comparison in the Rayleigh wave magnitude between the 65.2° and 43.1° wedges. (2) At shallower refracted angles, even though the attenuation is less severe, the Rayleigh wave is often masked due to its overlap with the first shear wave arrival. Although few experiments acknowledge the presence of the Rayleigh waves, previous authors such as Rose [14] and Krautkramer [105] have noted the possible existence of such waves.

4.3 2-D Finite Element Model

Although wavefield measurements allow for complete characterization of wave propagation on the surface of the plate, they do not provide information on the nature of wave propagation within the plate. To gain insight into the behavior of the waves as they propagate through the plate, a simplified 2-D model was developed over a two

week period with the help of Dr. Jim Blackshire at Air Force Research Labs (AFRL) using PZFlex, a commercially available software package for finite element analysis. PZFlex is a time domain solver that uses a combination of both explicit and implicit numerical methods to solve large wave propagation problems. The remainder of this section outlines the model parameters and presents the results for a model that mimics the experimental scenario for the Olympus Model ABWM-4T-60° wedge. These results are then compared to the experimental measurements presented in Section 4.2.

The PZFlex model, which can be seen in Figure 16, consists of a Rexolite plastic wedge modeled after the Olympus Model ABWM-4T-60°, the dimensions of which are summarized in Figure 17, liquid coupled to an 6.35 mm thick aluminum plate with silicone oil. The incident angle in the wedge, θ_w, and the refracted angle in the aluminum plate, θ_r, are 39.3° and 56.8°, respectively. The properties of the materials that constitute the model can be seen in Table 6. The wedge was excited using a uniform pressure load applied to a silicone coupling layer with the same diameter (6.35 mm) as the Model ABWM-4T-60° transducer. Absorbing boundary conditions were applied to the left and right sides of the plate and free boundary conditions were applied to the bottom and top. The grid size was set at 30 elements per wavelength (0.01 mm elements), which resulted in 11.124 million elements. The model was run for a duration of 25 μs with a time step of 1.2685 ns. A snapshot of the magnitude of particle displacement over the modeled area was obtained every 0.5 μs. The total execution time was 8.9 hours. To mimic the experimental B-scans in Section 4.2 the y-displacement (out-of-plane displacement) on the surface of the plate was recorded during the simulation at each 1.2685 ns time step.

The magnitude of the particle displacement over the modeled area obtained from the PZFlex model at several time instances between 4 μs and 20 μ scan be seen in Figure 18. The reflection of the shear waves between the two surfaces of the plate creates a complicated displacement profile through the plate, especially as the wave

fronts propagate further from the transducer. The Rayleigh wave doublet, noted in the experimental data in Section 4.2, can also be seen propagating along the surface of the plate at 8, 10, and 12 μs before it is overtaken by the shear waves.

By displaying the magnitude of particle displacement over the modeled area for time instances between 4.0 μs and 6.0 μs at a finer time interval, as is done in Figure 19, the generation of the Rayleigh wave doublet can be studied. A Rayleigh wave is generated at the interface between the wedge and plate; its generation can be

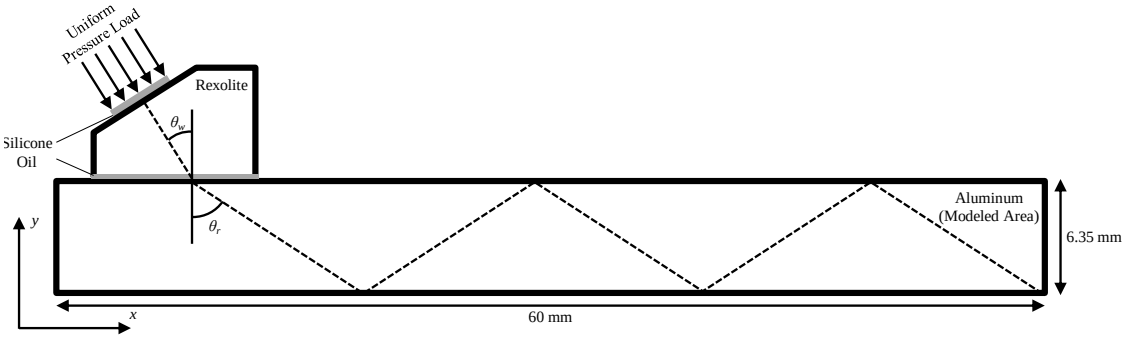

Figure 16: Diagram of the PZFlex model simulating angle-beam propagation in a scatterer-free plate.

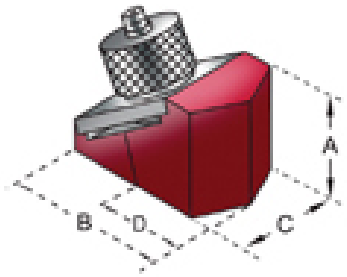

Wedge Angle	A (mm)	B (mm)	C (mm)	D (mm)
43.1°	12.4	16.8	11.4	5.8
56.8°	10.9	15.5	10.9	6.0
65.2°	12.2	18	10.9	6.8

Figure 17: Physical dimensions of Olympus angle-beam transducers, reproduced from [106].

Table 6: Properties of materials used in PZFlex model.

Material	Longitudinal Wave velocity (mm/μs)	Shear Wave velocity (mm/μs)	Density (kg/m^3)
Aluminum	6.306	3.114	2690
Rexolite	2.340	1.100	1060
Silicone Oil	0.960	–	818

clearly seen in the wake of the shear wave at time instances 5.0 and 5.5 μs. Another Rayleigh wave is generated by the interaction of the shear wave with the corner of the wedge, which can be seen at 7.0 μs. Because of the locations they were generated, the first Rayleigh wave generated will arrive later in the B-scan; to avoid confusion the Rayleigh waves will be denoted based on their appearance in the B-scan; i.e., the Rayleigh wave generated by the interaction of the shear wave with the corner of the wedge is the first wave in the doublet and the Rayleigh wave generated at the incident point is the second wave in the doublet.

4.4 Comparison of Models and Experiments

To validate the modeling results presented in Section 4.3, the surface displacement of the model was compared to the surface displacement obtained from wavefield measurements. Figure 20 gives a side-by-side comparison of the B-scan obtained from the wavefield measurement (left) and the PZFlex model (right) with and without the overplotted arrival time curves. Even given the geometric simplifications made in the PZFlex model, the modeling results are in excellent agreement with the measurements. Both the linear Rayleigh wave and hyperbolic shear wave trajectories agree almost perfectly with each other and with the arrival time curves generated using the ray-tracing model and parameters from Section 4.2. One of the more notable differences between the experimental and modeled B-scans are the sporadic arrivals in the modeled B-scan that occur both before and after the arrivals in the experimental B-scan. There are several possible explanations for these arrivals. (1) The arrivals could be the result of internal reflections within the wedge propagating into the plate. These reflections are typically damped by the 3-D geometry of the wedge. (2) The uniform pressure loading used as the excitation produces secondary reflections within the coupling layer that produce propagating waves that are not produced by the real transducer-wedge combination. (3) Possible model instabilities could account

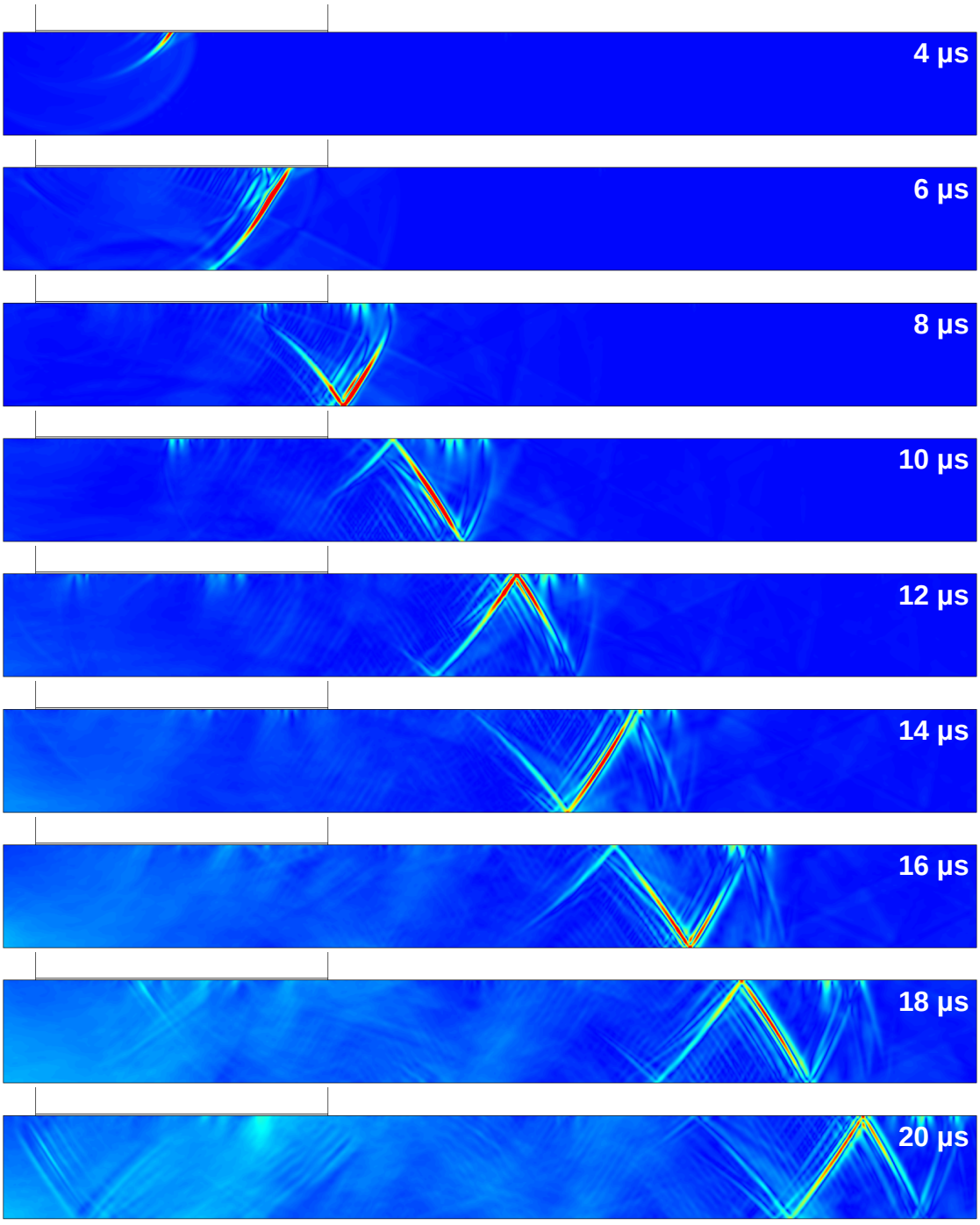

Figure 18: Magnitude of particle displacement in the plate obtained from the PZFlex model at various time instances.

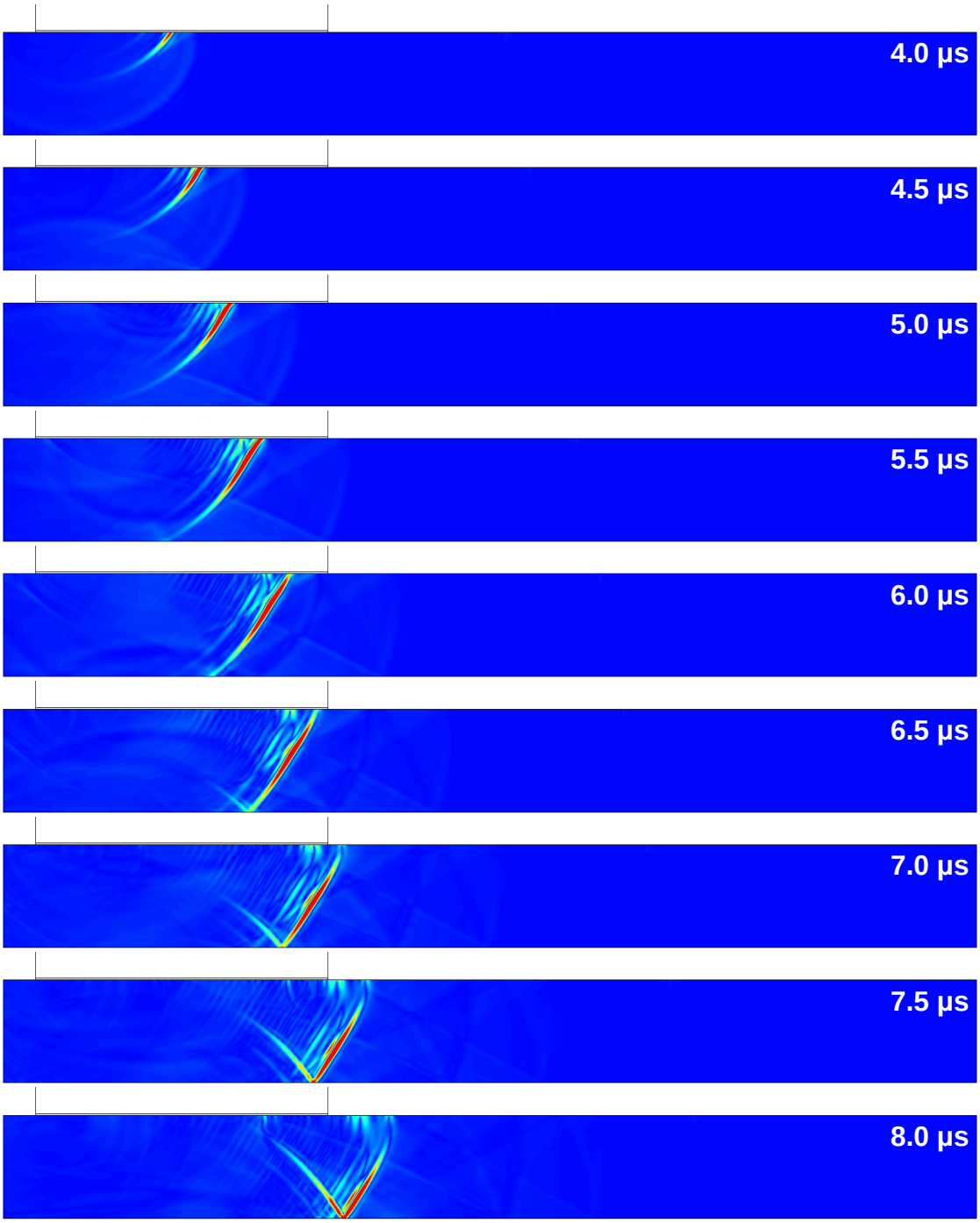

Figure 19: Magnitude of particle displacement in the plate obtained from the PZFlex model at various time instances, which highlight Rayleigh wave generation.

for some of the spurious arrivals, especially those at later time instances; modeling errors tend to be propagated through the model as the simulation time progresses. (4) Imperfect absorbing regions allow reflections from the ends of the plate.

In addition to the B-scan comparison, the experimental and modeling results can also be compared on a waveform-by-waveform basis as shown in Figure 21. As in the B-scans in Figure 20, the different wave arrivals have been identified in Figure 21; the convention for identification is as follows. Incident waves are identified by an abbreviation of the form: R (Rayleigh doublet), S_N (N^{th} shear wave skip), or RS_N (overlapping Rayleigh doublet and N^{th} shear wave skip). Comparing the two waveforms, the experimental data is slightly delayed when referenced to the model results. The delay most likely results from the wave generation within the piezoelectric transducer that is not captured by the simple uniform pressure loading used as an excitation in the PZFlex model. The differences between the piezoelectric transducer used in the experiments and the uniform pressure load used in the model may also account for the differences in the wave shapes. Differences in the waveforms may also arise from differences between the model and actual wedge material and dimensions. Contrary to normal experiment/model comparisons, the experimental wavefield data is less noisy than the model data; this most likely caused by the spurious wave arrivals giving the appearance of noise in the modeling data.

Despite minor differences in wave shapes, there is excellent agreement in overall wave propagation behavior including the presence of the Rayleigh wave doublet, the propagation trajectories, and the arrival times of the various waves. The size and complexity associated with solving more sophisticated 3-D angle-beam models makes wavefield imaging experiments an attractive method for developing a better understanding of angle-beam wave propagation and scattering.

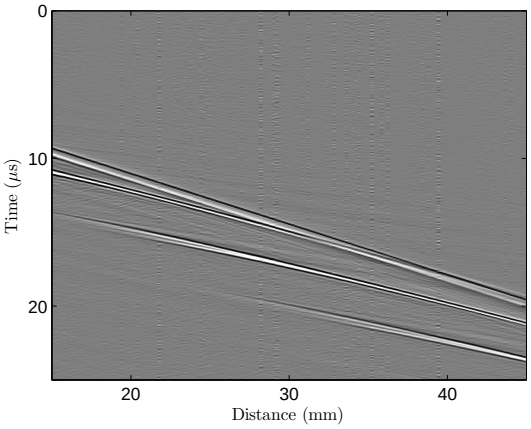

(a) Experimental Results

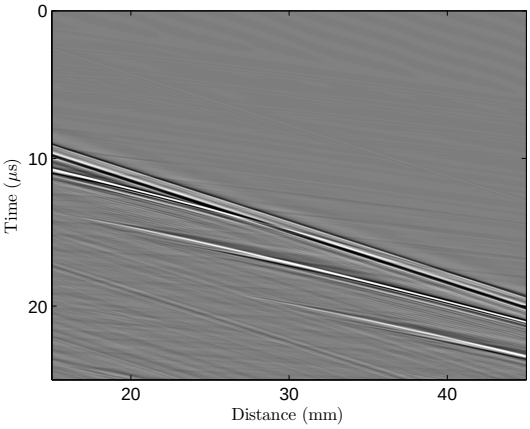

(b) PZFlex Model Results

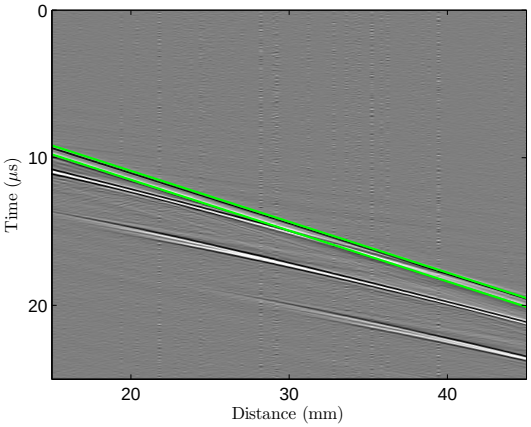

(c) Experimental Results: Rayleigh Waves

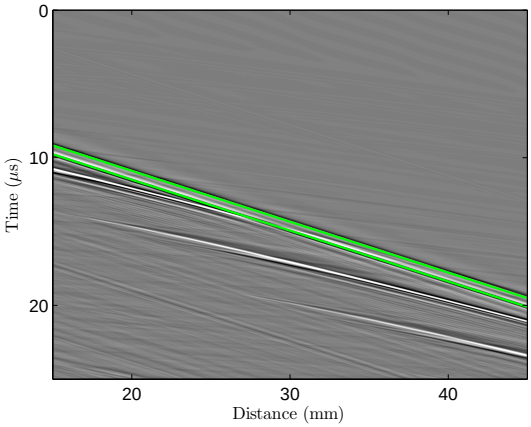

(d) PZFlex Model Results: Rayleigh Waves

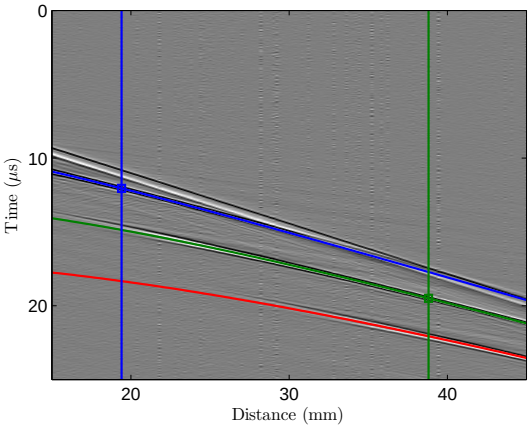

(e) Experimental Results: Shear Waves

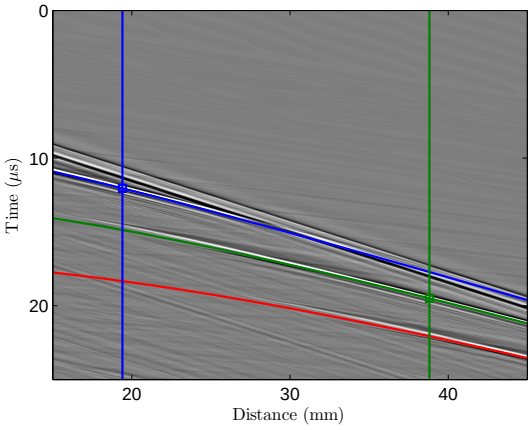

(f) PZFlex Model Results: Shear Waves

Figure 20: Overlay of theoretical arrival Rayleigh and shear waves time curves on the experimental (left) and PZFlex model (right) B-scans.

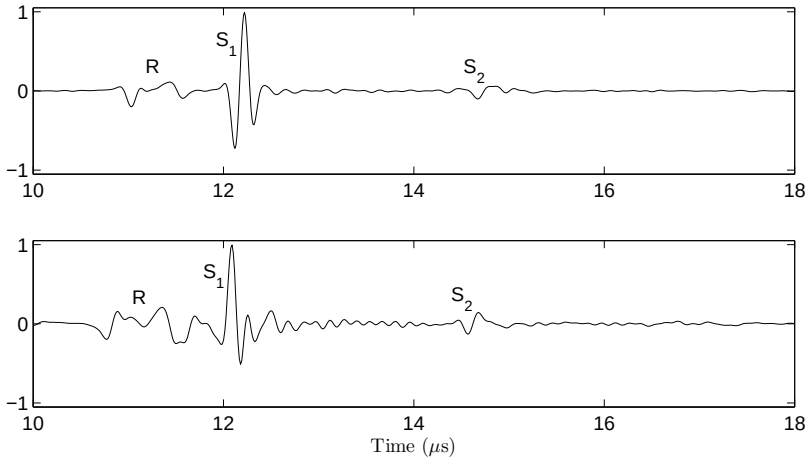

(a) Waveforms at 20 mm.

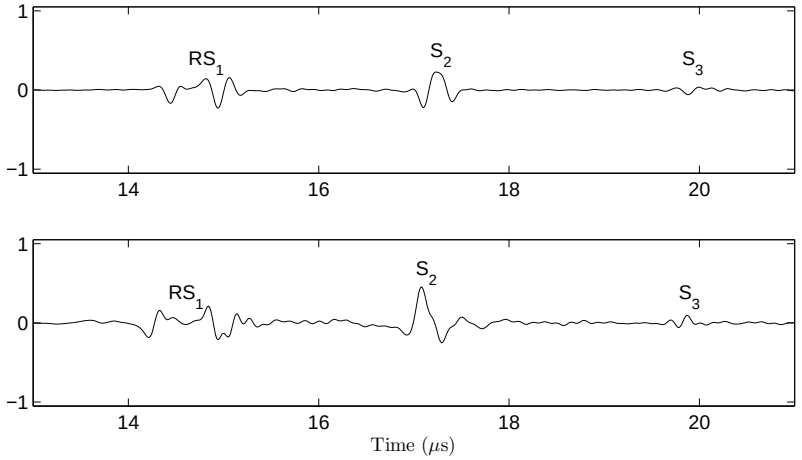

(b) Waveforms at 30 mm.

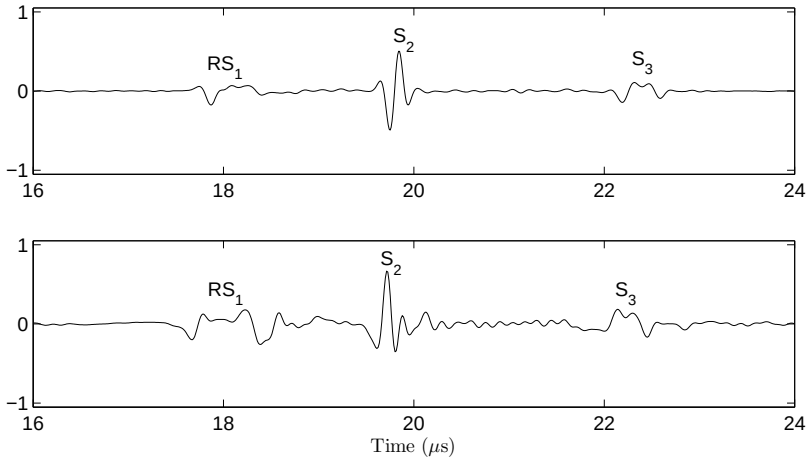

(c) Waveforms at 40 mm.

Figure 21: Comparison of experiment (top) and PZFlex model (bottom) waveforms at three distances.

CHAPTER V

WAVEFIELD ANALYSIS METHODOLOGY

In this chapter, a methodology is described for performing wavefield baseline subtraction to separate scattered waves from the total wavefield; that is, baseline wavefield data acquired from a defect-free specimen is subtracted from analogous data acquired after introduction of a defect. Two methods for aligning the wavefield data in space and time prior to performing baseline subtraction are presented and metrics for assessing their performance are discussed. Lastly, a method to generate radial energy maps is outlined. These radial energy maps provide a measure of the energy of waves propagating out from a point in the wavefield and can be used to generate scattering patterns.

5.1 Wavefield Data Preprocessing

Spatial windowing is applied to the wavefield data at different stages during the processing to reduce edge artifacts and remove noisy data from the empty hole where the laser vibrometer is out-of-focus. These steps are described in the following sections.

5.1.1 Edge Windowing

The finite scan window results in abrupt termination of the data at its outer edges, which causes spectral leakage in the wavenumber domain. To mitigate this problem, a 10% Tukey window was applied along the 30 mm extent of each spatial (x, y) dimension [103] to smooth the sharp transition between signal and no-signal at these edges.

5.1.2 Automated Through-Hole Windowing

Interruptions such as holes or changes in surface quality of the specimen are manifested as changes to the statistical distribution of the laser vibrometer measurements. If the correlation between the physical changes in the specimen and the changes in the signal distributions is well understood or can be accurately approximated, then the signal distribution can be used to spatially segment the data into different regions. Of particular interest here is the automatic location of the through-hole. Inconsistencies in plate mounting make the exact position of the hole unknown; automatic location of the hole efficiently accounts for spatial shifts caused by small mounting variations.

The presence of the through-hole introduces a region where the laser vibrometer is out-of-focus, resulting in noisy, large amplitude signals. It is convenient to apply gray level thresholding [107] of the wavefield data to distinguish between the through-hole and the plate by calculating $\Lambda(x, y)$, the sum of the absolute value of each waveform, as the test statistic,

$$\Lambda(x, y) = \sum_{n=1}^{N} |W(t_i, x, y)|, \tag{22}$$

where W is the wavefield data. Pixels for which $\Lambda > \gamma$ are identified as "though-hole," where γ is a threshold. Since the nominal size of the hole is known *a priori*, the threshold is adaptively set such that the total area of the pixels identified as "hole" matches the actual area of the hole. Various image fill techniques [108] can be used to remove points within the hole that are misidentified by the threshold test. Here, the MATLAB^{TM} function "imfill" [109] is used for this purpose so that an accurate hole area can be determined from the identified pixels.

Once the through-hole pixels are identified, the centroid [110] is calculated using the Matlab^{TM} function "regionprops" [111] and used as the center of a spatial window to remove the noisy signals. A 6th order circular Butterworth window with a 4 mm

radial cutoff is used to suppress the through-hole noise, and is given by

$$w_B(x,y) = \frac{1}{\sqrt{1+\left(\frac{r_c}{\sqrt{x^2+y^2}}\right)^2}}, \tag{23}$$

where r_c is the radial cutoff and $n = 6$ is the window order. For the 6.35 mm hole a 4 mm radial cutoff is used. Windowing the through-hole noise improves both the visual presentation of the wavefield data and reduces undesirable edge effects resulting from the sharp transition between signal and noise when utilizing frequency-wavenumber analysis methods.

5.2 Wavefield Baseline Subtraction

Wavefield baseline subtraction is performed by subtracting the corresponding waveforms in each wavefield to isolate the differences between them,

$$r(t,x,y) = w_c(t,x,y) - w_c(t,x,y) \tag{24}$$

The residual wavefield, $r(t,x,y)$, is the point-wise difference between signals contained in the current wavefield, $w_c(t,x,y)$, and a baseline wavefield, $w_B(t,x,y)$; all signals here are expressed in the 3-D time-space domain.

5.2.1 Metrics for Baseline Subtraction Performance

The efficacy of baseline subtraction can be evaluated qualitatively by inspection of the residual wavefield at time instances of interest. Poor baseline subtraction is typically manifested as feed-through of larger amplitude incident waves, which obscure the smaller amplitude scattered waves. Performance can be quantified by computing the energy of each residual signal either relative to the maximum baseline signal energy or relative to the energy of the baseline at each point in the wavefield.

The energy of the residual at pixel location (x_l, y_m), referenced to the maximum

of the energy of the baseline, is expressed in dB as,

$$E_G(x_l, y_m) = 10 \log_{10} \left(\frac{\sum_n r(t_n, x_l, y_m)^2}{\max_{i,j} \left(\sum_n w_B(t_n, x_i, y_j)^2 \right)} \right). \tag{25}$$

Since the reference is the maximum energy of the baseline, E_G is referred to as the globally referenced residual energy. The peak and mean of E_G can be readily calculated and are also useful as performance metrics.

It is also informative to reference the energy of the residual to the local energy of the baseline; i.e., each spatial location is referenced to the energy of the baseline at that same location:

$$E_L(x_l, y_m) = 10 \log_{10} \left(\frac{\sum_n r(t_n, x_l, y_m)}{\sum_n w_B(t_n, x_l, y_m)^2} \right). \tag{26}$$

This metric, E_L, is referred to as the locally referenced residual energy.

If no damage is introduced in between acquisition of the baseline and current wavefield, both metrics should ideally be zero. If damage has been introduced, then either measure of residual energy should be related to the strength of the scatterer.

5.2.2 Factors Affecting Baseline Subtraction Performance

Baseline subtraction performance is dependent on the degree to which signals resulting from structural elements remain consistent from measurement to measurement. Generally, signal inconsistencies that reduce the performance of baseline subtraction are the result of uncontrolled environmental conditions the structure is subjected to during measurement. Here, the two factors that most negatively affect the performance of wavefield baseline subtraction are temperature changes and spatial misalignment. Of these two factors, spatial misalignment is the most detrimental to wavefield subtraction performance.

5.2.2.1 *Effects of Temperature*

As discussed in Section 2.5.4.2, the primary effect of a change in temperature is a change in the ultrasonic velocity. The change of ultrasonic velocity affects received signals by introducing a time-dependent time shift [71]. Assuming a wave arrival time of t_0 and a temperature change of ΔT, the change in the time of arrival for a shear wave can be calculated as,

$$\Delta t = \frac{c_s t_0}{c_s + \kappa_s \Delta T} - t_0 \approx -t_0 \frac{\kappa_s}{c_s} \Delta T, \tag{27}$$

where c_s is the shear wave velocity (3080 m/s for 6061 aluminum) and κ_s is the coefficient of change in shear velocity with temperature (-0.752 m/s/°C for shear waves in aluminum [112]). A 2°C change in temperature would thus result in a time shift of about 0.012 μs for an echo arriving at 25 μs and 0.024 μs for an echo arriving at 50 μs. Given that the period of a 5 MHz sinusoid is 0.2 μs and times of arrivals of interest are generally less than 50 μs, time shifts caused by temperature changes of $\pm$2°C or less will not have a significant effect on baseline subtraction.

5.2.2.2 *Effects of Spatial Misalignment*

Spatial misalignment errors can be evaluated relative to the smallest wavelength present in the data, which is approximately 0.3 mm (Rayleigh wavelength at 10 MHz). For good baseline subtraction, the spatial misalignment error should be no bigger than about 10% of the wavelength, which is about 0.03 mm. It is highly unlikely that the specimen can be manually repositioned this accurately, although 0.1-0.2 mm should be possible. The estimated repeatability of the scanner used for these experiments is approximately 0.05 mm, which is close to 0.03 mm. Given that the energy is centered at 5 MHz (Rayleigh wavelength of 0.6 mm), the scanner repeatability, although not negligible, is likely not the primary source of misalignment.

5.2.3 Alignment Methods for Baseline Subtraction

The primary source of poor baseline subtraction for the wavefield data reported here is global spatial misalignment caused by specimen repositioning, which should be manifested as a simple translation. With this assumption, a variety of global image registration algorithms could be candidates to compensate for differences between the measurements; these include direct (pixel-based) registration or feature-based registration [92, 91]. The problem at hand is simpler in some ways than typical image registration problems in that there are no changes in rotation or magnification, but the time-dependence of the wavefield introduces challenges. Although temperature changes are not expected to be significant, the possibility of temporal misalignment should also be considered.

Two methods for the aligning the baseline wavefield with the current wavefield are proposed and compared. The first method globally aligns the baseline wavefield with the current wavefield in three dimensions (two spatial dimensions and time). The second method spatially aligns the baseline wavefield with the current wavefield on a frame-by-frame basis, but searches the baseline wavefield forward and backward in time for several frames to select the one with the best registration after spatial alignment. The second method provides more flexibility in both spatially and temporally aligning the wavefields, which could potentially give a better degree of registration in the presence of a global temperature change. Both alignment methods are performed on the first 30 μs (750 frames) of data , which contains most of the signals of interest for the spatial scan window. The methods are applied to the data following deconvolution, and spatial windowing as described in Section 5.1 is applied following determination of the optimum spatial shift to compute the residual wavefield.

5.2.3.1 Global Space-Time Alignment

The first method of wavefield image registration, global space-time alignment (GSTA), optimally registers the baseline wavefield with the current wavefield by applying subpixel spatial and temporal global shifts. This method, which is similar to the well-known phase correlation method [113], should correct for simple shifts in the plate position as well as a constant time shift, providing a first order correction for a global temperature change.

The GSTA method is accomplished in the frequency domain by minimizing the L_2 norm of the residual with respect to $(\Delta t, \Delta x, \Delta y)$, which are the shifts in t, x and y that are applied to the baseline wavefield prior to subtraction:

$$(\Delta t_0, \Delta x_0, \Delta y_0) = \underset{\Delta t, \Delta x, \Delta y}{\arg\min} ||W_C(\omega, k_x, k_y) - W_B(\omega, k_x, k_y) e^{-i(\omega \Delta t + k_x \Delta x + k_y \Delta y)}||. \quad (28)$$

Here W_B and W_C are the baseline and current wavefield data, respectively, in the ω-k domain and $(\Delta t_0, \Delta x_0, \Delta y_0)$ are the optimal shifts along the three wavefield data dimensions that minimize the L^2 norm of the residual. The residual wavefield in the ω-k domain is thus calculated as,

$$R(\omega, k_x, k_y) = W_C(\omega, k_x, k_y) - W_B(\omega, k_x, k_y) e^{-i(\omega \Delta t_0 + k_x \Delta x_0 + k_y \Delta y_0)}, \quad (29)$$

which is converted back to the (t, x, y) domain via an inverse 3-D Fourier transform. Since the shifts are performed in the frequency-wavenumber domain, subpixel registration of the discrete wavefield data is possible and is achieved using the MATLAB™ function "fminsearch" [114]. As applied here, both the baseline and current wavefields are down-sampled in time to 25 MHz prior to alignment, which significantly reduces the processing time. The down-sampling does not compromise performance since 25 MHz is a sufficiently high sampling frequency to prevent temporal aliasing, and sub-sample shifts are possible in the frequency-wavenumber domain.

5.2.3.2 Time Slice Spatial Alignment

The second method of wavefield image registration, time slice spatial alignment (TSSA), spatially aligns each time slice of the current wavefield with a corresponding time slice (frame) of the baseline wavefield prior to calculating the residual wavefield. The frame of the baseline wavefield used for the spatial alignment is selected by looking forward and backward in time by several frames to find the one that is best aligned with the current frame. This method should correct for simple shifts in the plate position as well as time-varying time shifts, which would provide a second order correction for a temperature change.

This method is performed by first transforming each frame of both the current and baseline wavefields into the k_x-k_y domain via a spatial 2-D Fourier transform. For the nth time slice of the current wavefield, which is at t_n, a range of frames in the baseline wavefield are considered both before and after t_n. The one is selected that minimizes the L_2 norm of the residual in the k_x-k_y domain after spatial alignment:

$$(t_n^B, \Delta x_n, \Delta y_n) = \underset{\Delta t_k, \Delta x, \Delta y}{\arg\min} ||\overline{W}_C(t_n, k_x, k_y) - \overline{W}_B(t_k, k_x, k_y) e^{-i(k_x \Delta x + k_y \Delta y)}|| \forall k \in [n_L n_u], \tag{30}$$

where $\overline{W}_C$ and $\overline{W}_B$ are the 2-D Fourier transforms of each frame in the current and baseline wavefields. Here n_L and n_U and the lower and upper bounds of the baseline frame index k, t_n^B is the selected time slice of the baseline wavefield corresponding to the n^{th} time slice of the current wavefield, and $(\Delta x_n, \Delta y_n)$ are the corresponding spatial shifts. The residual wavefield in the wavenumber domain at time t_n is thus calculated as,

$$\overline{R}(t_n, k_x, k_y) = \overline{W}_C(t_n, k_x, k_y) - \overline{W}_B(t_n^B, k_x, k_y) e^{-i(k_x \Delta x_n + k_y \Delta y_n)}, \tag{31}$$

which is converted back to the (t, x, y) domain via an inverse 2-D Fourier transform at each time step. Subpixel registration of the discrete wavefield data is again possible

and is achieved using the built in MATLAB^{TM} function "fminsearch" [114] at each time slice. By performing the optimal spatial alignment on a frame-by-frame basis and by allowing some play in the correspondence between frames in the two wavefields, the alignment is more robust to environmental variations such as a temperature change. As a note, the temporal sampling of the two wavefields does not have to be the same to use the TSSA method. As applied here, the current wavefield is down-sampled to 25 MHz prior to alignment but the baseline wavefield is retained at 100 MHz. This finer sampling interval for the baseline improves the performance of TSSA by increasing the resolution of the frames available for matching.

5.3 Analysis of Scattering Behavior

Wavefield imaging eliminates many of the challenges associated with experimental characterization of angle-beam scattering and allows for techniques similar to those outlined in Section 2.5.5 for SHM to be used. The use of wavefield data to obtain angle-beam scattering patterns is more complicated than for guided waves because guided waves excite the plate throughout its thickness whereas angle-beam waves reflect between the plate surfaces. Since wavefield measurements are performed on the surface of the plate, there is the potential for ambiguity between different wave modes because the phase velocity, Eq. 16, is a function of both the wave velocity and the refracted angle. Another complication to producing angle-beam scattering patterns is mode conversion. Mode conversion is a function of the incident wave mode and incident angle as well as the defect type and orientation. The combination of phase velocity ambiguity and mode conversion makes analyzing angle-beam bulk wave scattering difficult. Any method to characterize angle-beam scattering must be able to accurately measure and quantify scattering in the presence of multiple waves modes propagating at different refracted angles. The remainder of this section outlines a method to use wavefield data to obtain estimated scattering patterns that

can both separate waves propagating at different velocities and provide a means for estimating mode conversion.

The flow chart in Figure 22 details a methodology to calculate the energy of the outward propagating waves as a function of the angle and the wave velocity, referred to as a radial energy map, which can be used to generate angle-beam scattering patterns as a function of wave mode. In addition to the flow chart, Figure 22 provides examples of representative data (Scan #4) at each step of the process. In Step 1 of the flow chart, preprocessing may include spatial Tukey windowing and automated hole-windowing, described in Section 5.1, and wavefield alignment using either GSTA or TSSA, described in Section 5.2.3, if the scattering patterns of two sets of wavefield data are being compared.

For Step 2, the B-scan data at each angle, θ from a specified reference point, is interpolated from the full wavefield data. The length of the interpolated B-scan, R, is set such that none of the points in the B-scan fall outside of the smallest circle, centered on the automatically detected hole, that can be inscribed in the scan area. In the case where the origin of the radial B-scans is centered on a point, (x_{ref},y_{ref}), other than the center of the hole, as seen in Figure 23, R will be a non-constant continuous function of θ, which follows from the cosine rule,

$$R = \sqrt{r_1^2 - r_2^2 \sin^2(\theta)} - r_2 \cos(\theta), \tag{32}$$

where r_1 is the radius of the inscribed circle and r_2 distance from the origin of the radial B-scan to the center of the inscribed circle. Restricting the value of R in this way prevents sharp changes in the energy calculation by removing the corner effects.

Since the scattered energy is of interest, only the energy of the wave propagating outwards (positive velocity) from the origin of the radial B-scan is calculated in Step 4. By computing the energy in the frequency-wavenumber domain, there is an inherent ability to separate the energy from waves propagating at different velocities.

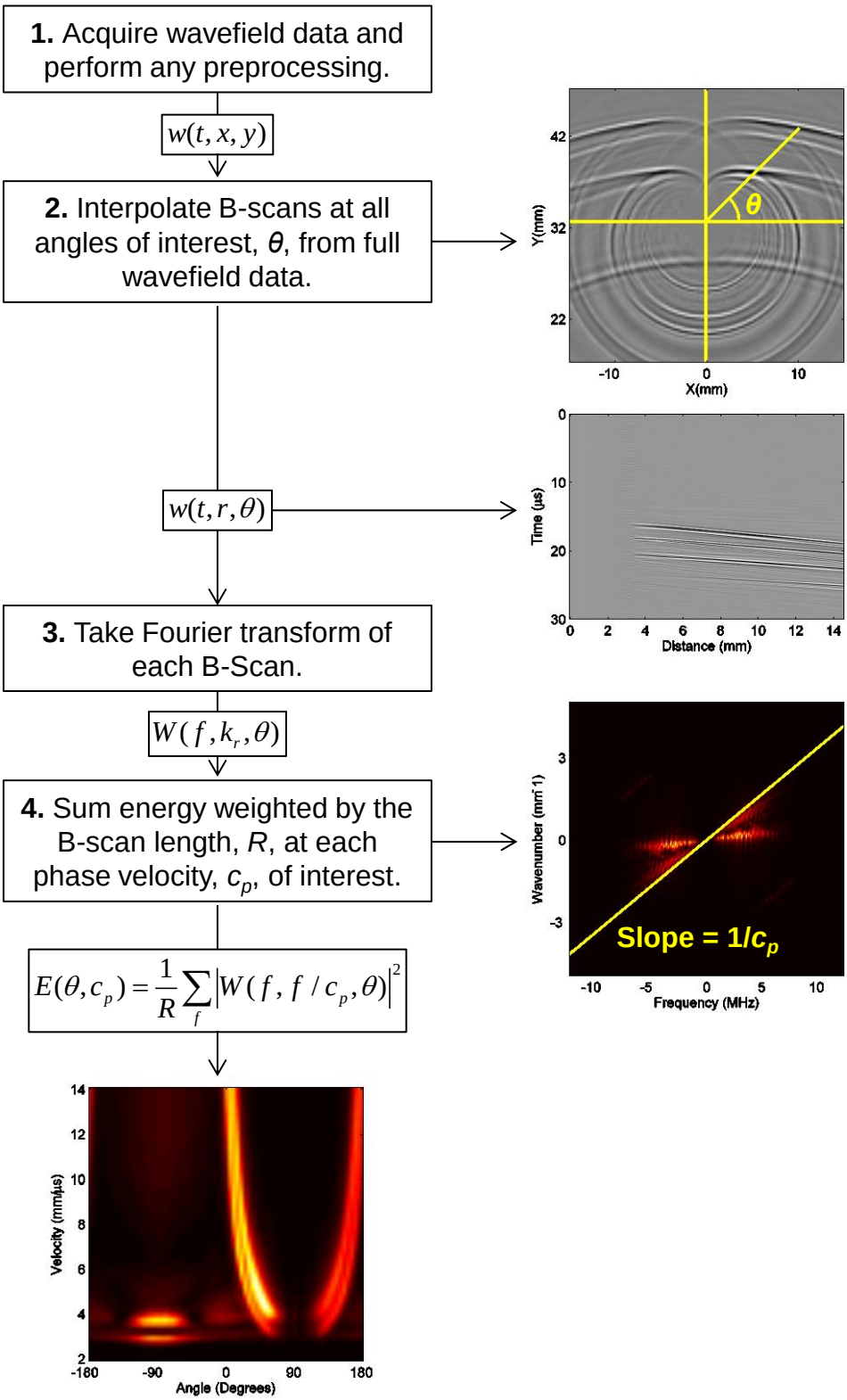

Figure 22: Flow chart of the methodology for generating radial energy maps with examples of representative data.

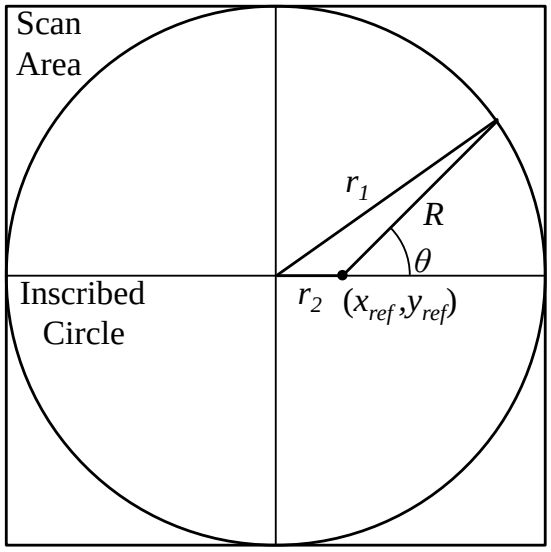

Figure 23: Diagram of the radius used for the radial B-scans based on a off-centered reference point.

After calculating the radial energy map, it can be used to characterize scattering or as a means determining or isolating the effects of a scatterer by comparing two radial energy maps. When comparing two scatterers or scattering scenarios, the radial energy maps can be subtracted to isolate the scattering from the defect,

$$E_D(\theta, c) = E_C(\theta, c) - E_B(\theta, c) \tag{33}$$

where E_C is the current radial energy map containing the defect or scatterer of interest and E_B is the radial energy map being used as the baseline. In addition to subtracting the radial energy maps, the log ratio of the the modal scattering patterns,

$$E_R(\theta, c) = 10 \log_{10}\left(\frac{E_C(\theta, c)}{E_B(\theta, c)}\right) \tag{34}$$

can be used to investigate the changes in the scattering behavior resulting from the addition of the defect and is similar to the scattering coefficients used to quantify Lamb wave scattering described in Section 2.5.5.

Despite the potential ambiguity between different wave modes caused by the fact that the phase velocity is a function of both the wave velocity and the refracted angle,

the ability to measure the radial energy as a function of the phase velocity is a powerful means to separate and study the scattering of different wave modes, especially for wave velocities where this ambiguity does not exist. Scattering patterns for the three wave modes of interest: Rayleigh, shear, and longitudinal, can be generated by summing along the range of phase velocities corresponding to the desired wave mode in the radial energy map. Table 7 summarizes the phase velocity ranges that are used to produce scattering patterns for each wave mode. Since the Rayleigh wave propagates along the surface, its range of phase velocities is much smaller than the range for the shear and longitudinal waves. There is an ambiguity between longitudinal and shear waves for velocities above 6.306 mm/μs; however most of the shear wave energy is captured by the chosen velocity range.

Table 7: Phase velocity ranges used to generate scattering patterns for each wave type.

Wave Mode	Wave Velocity (mm/μs)	Phase Velocity Range (mm/μs)	Shear Angle Range*	Longitudinal Angle Range*
Rayleigh	2.902	2.6-3.0	–	–
Shear	3.114	3.2-6.2	76.7°-30.1°	–
Longitudinal	6.306	6.4-14	29.1°-12.9°	80.2°-26.8°

*Calculated from Eq. 16.

Figure 24 shows the radial energy map, of a 6.35 mm through hole with the radial B-scans referenced to the center of the whole. The angle interval for the radial energy maps is 5° and the velocity interval is 0.2 mm/μs. Figure 24 also shows plotted on the radial energy map the velocity ranges, which were summed over to generate scattering patterns for each mode, identified as well scattering patterns for the Rayleigh, shear, and longitudinal waves. The lack of symmetry in the radial energy map and the scattering patterns is a result of the transducer not being perfectly centered on the through hole. The radial energy map was generated without the use of baseline subtraction to remove the incident waves and so the presence of the incident

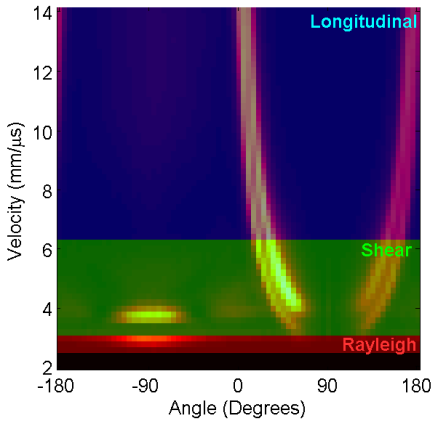

(a) Modal Scattering Pattern

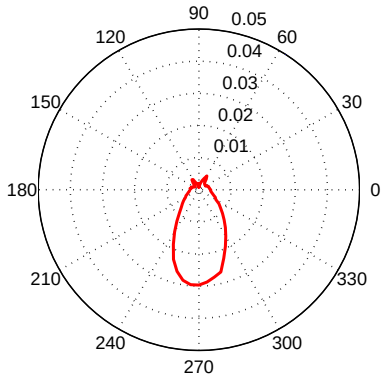

(b) Scattering Pattern: Rayleigh

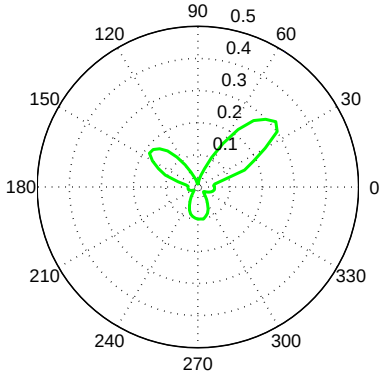

(c) Scattering Pattern: Shear

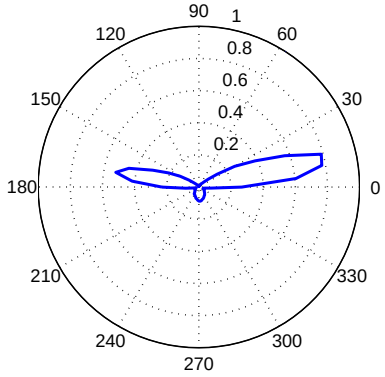

(d) Scattering Pattern: Longitudinal

Figure 24: Scattering patterns for scan #4 including (a) the radial energy map with velocity ranges for each mode identified and scattering patterns for the (b) Rayleigh, (c) shear, and (d) longitudinal waves.

waves, which form the asymptotes at 0° and 180°, are clearly visible. The asymptotic behavior of the phase velocity of the incident waves results from the fact that the direction of propagation of the incident waves is perpendicular to the radial B-scan at these angles, so the incident waves appear to move through the B-scan much faster than they are actually traveling. The scattering patterns for the longitudinal waves, Figure 24(d), is the most affected by this phenomenon because the velocity range used to generate it is much greater. The shear wave scattering pattern is affected as well, although to a lesser extent. The presence of the incident waves can often be

removed using baseline subtraction. The remainder of radial energy maps presented here will focus on isolating scattering by removing the incident waves using either baseline subtraction, the radial energy difference, or the radial energy ratio.

CHAPTER VI

WAVEFIELD ANALYSIS RESULTS

The purpose of this chapter is to evaluate the performance of the baseline subtraction methods outlined in Section 5.2, to use the methods described in Section 5.3 to analyze scattering from corner notches, and to discuss the efficacy of the methods for characterizing angle-beam scattering. First, the performance of the two baseline subtraction methods is evaluated and compared on nominally identical data sets with and without spatial misalignment. Second, the two baseline subtraction methods are used to isolate the scattered waves from notches of four different sizes for two different transducer orientations: -90° and 45° relative to the notch. Radial energy maps and scattering patterns are generated from the TSSA aligned wavefields using the methods described in Section 5.3 and the scattering from the notches is discussed. Finally, the ability of the analysis methodology to characterize scattering is discussed.

6.1 Quantifying Baseline Subtraction Performance

Scans #9, #10, and #11 were all recorded from the specimen containing a through-hole with a 4 mm corner notch. Scan #10 was recorded immediately after scan #9 with no repositioning of the specimen and no significant temperature changes. Scan #11 was recorded immediately after scan #10 and the specimen was repositioned. Although the notch is a scatterer of interest, scan #9 is first used as a baseline for scan #10 and #11 to assess the performance of baseline subtraction for nominally identical wavefields without and with spatial misalignment.

Figure 25 shows direct baseline subtraction results between scans #9 and #10 in the form of a snapshot of the residual wavefield at 19 μs (Figure 25(a)), the globally referenced residual energy map (E_G from Eq. 25, Figure 25(c)), and a histogram of

the raw residual energy values (Figure 25(e)). Note that the gray scale for this and subsequent snapshots is identical to those of Figure 8. Aside from artifacts around the hole, it can be seen that the performance of baseline subtraction is the worst in the high amplitude area of the incident wavefield directly in front of the hole, which is not unexpected since even a small phase mismatch will cause incomplete cancellation. The mean and peak of the residual energy are 24.5 and 5.9 dB lower, respectively, than the mean energy of the baseline wavefield (scan #9). As a means of comparison, the peak value of the baseline scan (scan #9) is 11.5 dB higher than the mean value.

Both the GSTA and TSSA methods were performed prior to baseline subtraction of scans #9 and #10 and reduce the mean and peak residual energy as compared to direct subtraction. There is not much improvement since the wavefields were already well-aligned and so the results are not shown. As seen in Table 8, GSTA performs slightly better than TSSA for this case. The primary difference between these wavefields is the random noise in the hole, and the TSSA method has enough degrees of freedom so that this noise can be partially suppressed. A side effect is that performance is slightly reduced as compared to GSTA since final residual wavefields are computed after spatial windowing where as alignment is performed prior to spatial windowing.

To investigate the effects of spatial misalignment, baseline subtraction was performed using scan #10 as the baseline wavefield and scan #11 as the current wavefield. The result of direct baseline subtraction of these two scans can be seen in Figure 25. The slight spatial misalignment between the two measurements, which was estimated to be less than 0.5 mm in both the x and y directions, is large enough so that no appreciable cancellation can be seen in the snapshot of the residual wavefield.

Comparison of Figures 25(a) and 25(b) shows a substantial reduction in the performance of the baseline subtraction. Comparing the residual energy maps, the degradation in performance is as high as 20 dB in some areas where the signals are large

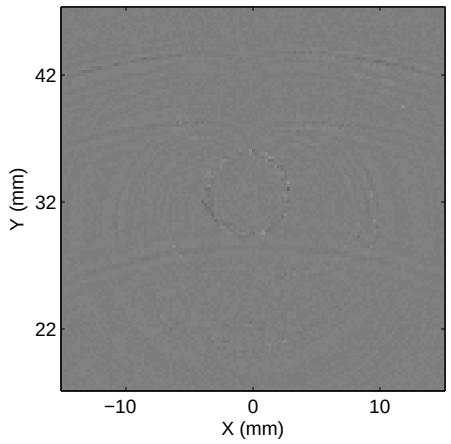

(a) Back-to-Back Scans: Snapshot at 19 μs

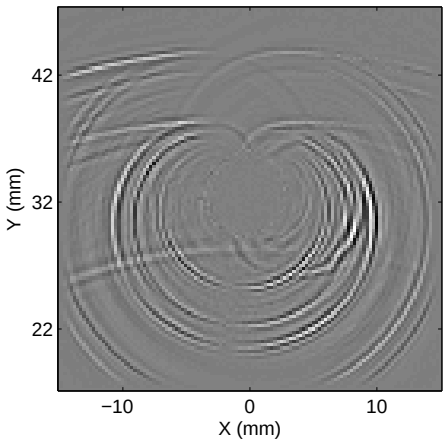

(b) Remounted Scans: Snapshot at 19 μs

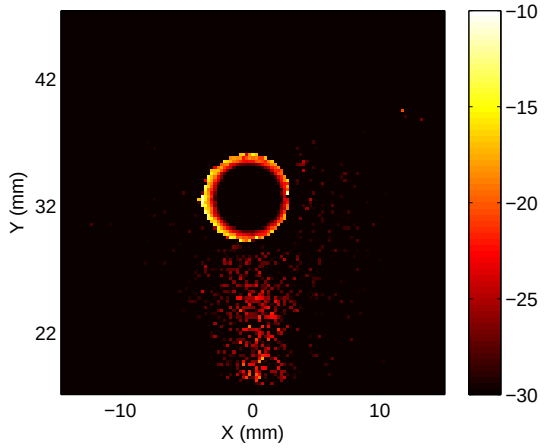

(c) Back-to-Back: Energy

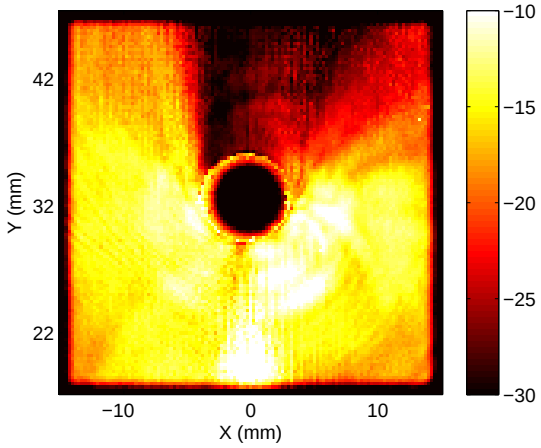

(d) Remounted Scans: Energy

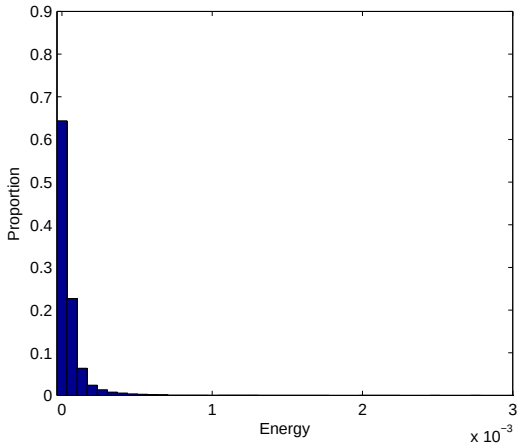

(e) Back-to-Back: Energy Histogram

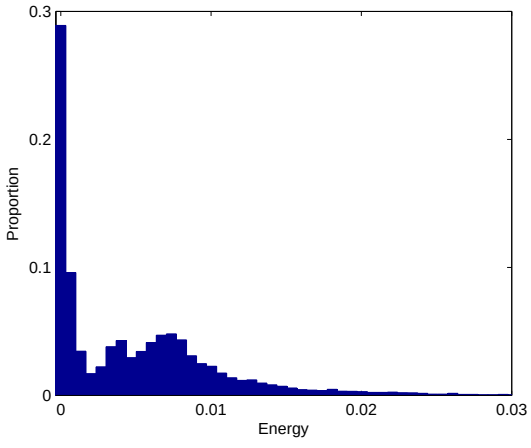

(f) Remounted: Energy Histogram

Figure 25: Baseline subtraction results for back-to-back scans without (scan #10, left) and with (scan #11, right) specimen remounting using scan #9 as the baseline without alignment.

Table 8: Comparison of the performance of baseline subtraction methodologies without and with specimen remounting.

Current Scan	Baseline Scan	Description	Alignment Method	Mean Residual Energy (dB)	Peak Residual Energy (dB)
#10	#9	Baseline: 4 mm notch Current: 4 mm notch No specimen remounting	None	-24.5	-5.9
#10	#9		GSTA	-27.4	-9.1
#10	#9		TSSA	-25.4	-7.7
#11	#10	Baseline: 4 mm notch Current: 4 mm notch Specimen Remounted	None	-4.7	7.1
#11	#10		GSTA	-19.8	-2.8
#11	#10		TSSA	-21.0	-2.9

in amplitude. A comparison of the energy histograms in Figure 25(e) and 25(f) also shows the ineffectiveness of baseline subtraction after the specimen has been removed and remounted. The histogram of Figure 25(f) can also be compared to that of the total wavefield in Fig. 4(c). There is an increase in the proportion of energy values close to zero after baseline subtraction, but the distribution is still much more similar to that of the total wavefield than to the residual wavefield of Figure 25 with no specimen remounting. Instead of a 24.5 dB reduction in the mean energy, there is only a 4.7 dB reduction, and a 7.1 dB increase in the peak energy rather than a 5.9 dB decrease. This increase indicates that the subtraction has actually caused constructive interference of the two wavefields, at least in some locations, rather than cancellation.

Figure 26 shows the corresponding results of baseline subtraction of scans #10 and #11 after applying the GSTA and TSSA alignment methods, respectively. A comparison of these figures to those of Figure 25 shows that using either alignment method significantly improves baseline subtraction performance following specimen remounting. The TSSA method performs somewhat better than GSTA, particularly

in the lower portion of the scan area (below the hole) where signals are the largest amplitude. It can be seen that both alignment methods remove the double-peak structure from the energy histogram and yield distributions more comparable to that of Figure 25(e), which was generated from successive scans without specimen remounting. The mean energy of the residual after remounting is reduced from that of the baseline by 19.1 dB and 21.1 dB for GSTA and TSSA, respectively, and the peak energy by 2.8 dB and 2.9 dB. While not quite as good as the 24.5 dB and 5.9 reductions (mean and peak) obtained from the back-to-back scans, it is nevertheless a substantial improvement as compared to direct subtraction.

Although both alignment methods have similar baseline subtraction performance, there are some noteworthy differences. Since the TSSA method aligns the wavefields on a frame-by-frame basis (i.e., as a function of time), it has the capability of compensating for the time-dependent time shifts that would be indicative of a temperature change. Even though temperature was not expected to be a significant issue for the data recorded here, nevertheless it was not measured to the accuracy required to verify this assumption, and the somewhat improved performance of the TSSA method over GSTA indicates that temperature may indeed have been a secondary but non-negligible factor.

A further comparison of the methods can be made from maps of the locally referenced residual energy (E_L from Eq. 26), which can be seen in Figure 27. For the case of no specimen remounting, the energy of the residual referenced to the local energy of the baseline, Figure 27(a), has the appearance of speckled noise with little structure, indicating that random variations in the signals are proportional to signal amplitudes. This characteristic is indicative of laser speckle noise rather than additive random noise, which would be independent of signal amplitude. The only exception is in the shadow zone (i.e., near 90°), where the signal strength is very low to begin with and additive random noise appears to dominate over laser speckle noise. Although

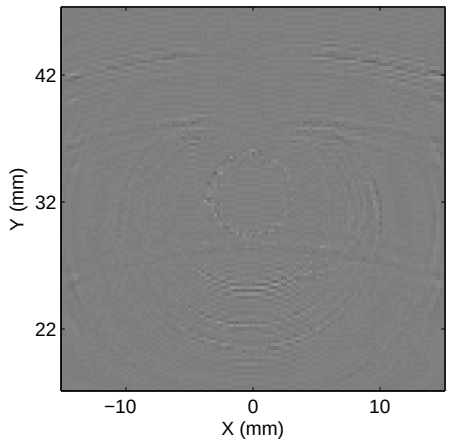

(a) GSTA: Snapshot at 19 μs

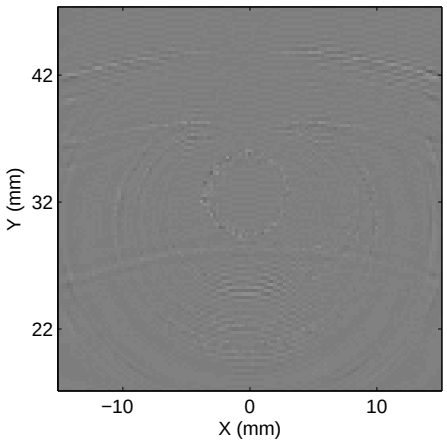

(b) TSSA: Snapshot at 19 μs

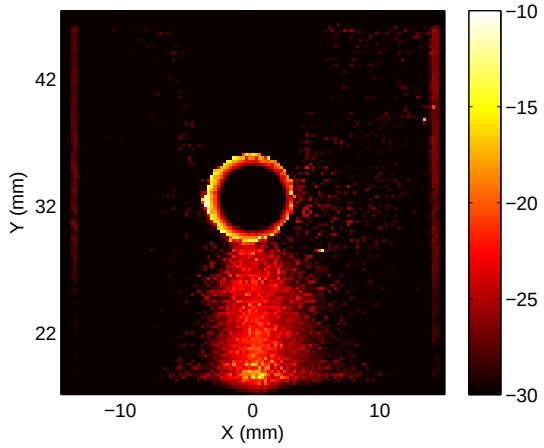

(c) GSTA: Energy

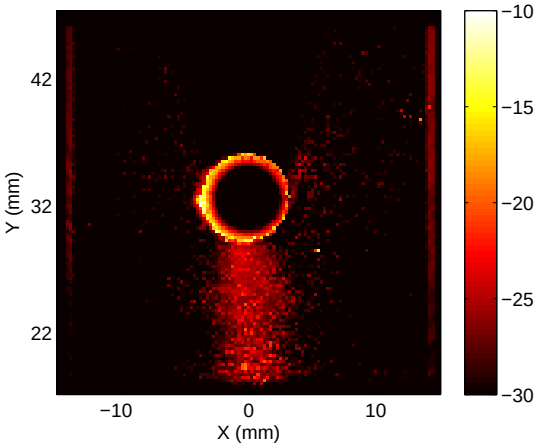

(d) TSSA: Energy

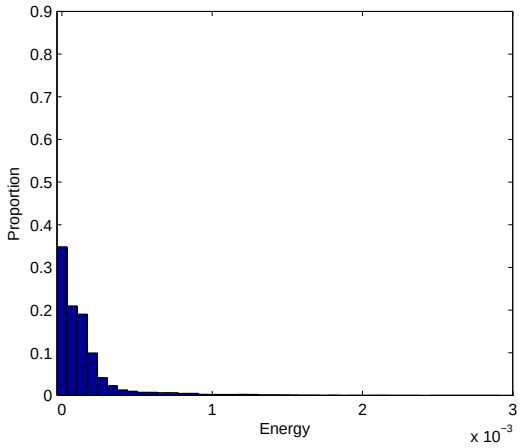

(e) GSTA: Energy Histogram

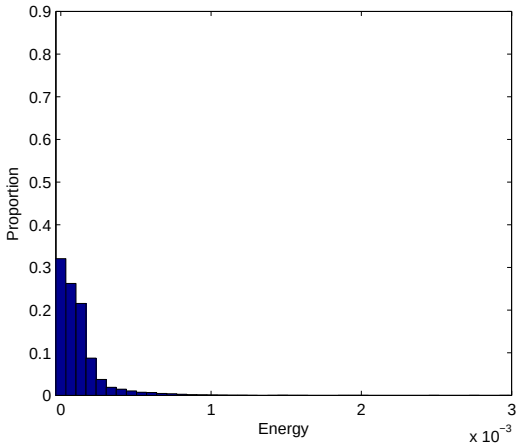

(f) TSSA: Energy Histogram

Figure 26: Baseline subtraction results for back-to-back scans for a remounted specimen (scan #11) with the baseline (scan #9) aligned using the GSTA (left) and TSSA (right) methods.

similar, Figure 27(b) and 27(c) both have more structure than that of Figure 27(a), for which the specimen was not remounted. Although not shown here, for TSSA the structure of the locally referenced energy maps is more pronounced if a coarser temporal sampling interval is used for the baseline (e.g., 25 MHz vs. 100 MHz). Since the frame-by-frame matching does not allow for sub-pixel temporal shifts, performance of the TSSA method decreases with coarser sampling and becomes comparable to that of GSTA. Although temperature changes in between scans were small for the data reported here, the TSSA method should outperform GTSA if there are larger temperature differences.

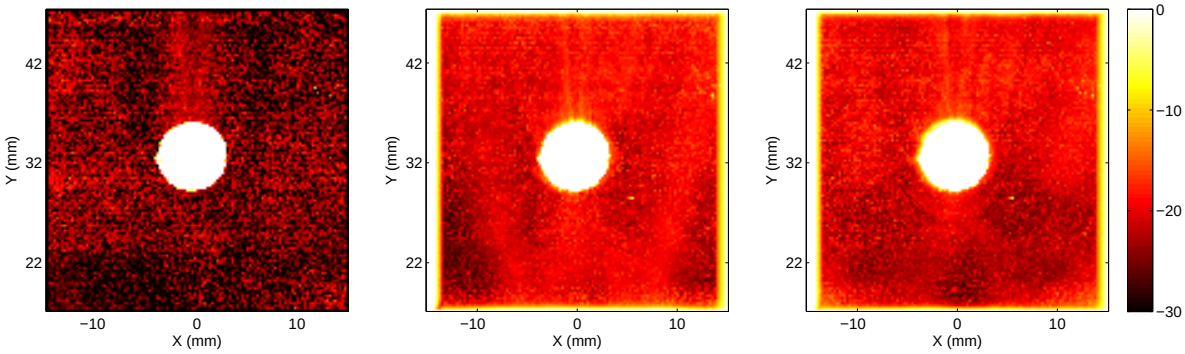

(a) Back-to-Back: No Alignment (b) Remounted: GSTA (c) Remounted: TSSA

Figure 27: Locally referenced residual energy for different baseline subtraction scenarios.

6.2 Isolation and Analysis of Scattering Behavior

Baseline subtraction is used to separate and highlight scattering from 1, 2, 3 and 4 mm corner notches originating from the 6.35 mm drilled through-hole for both the -90° and 45° transducer orientations; specifically, the effect of notch size on scattering will be studied. For each transducer orientation, wavefield snapshots and energy maps are shown after baseline subtraction. Radial energy maps and scattering patterns are generated from the TSSA aligned wavefields using the methods described in Section 5.3 and the scattering from the notches is discussed.

6.2.1 -90° Transducer Orientation

For the transducer oriented at -90°, baseline subtraction is performed for each notch size using scan #4 as the baseline, snapshots of which can be seen in the left column of Figure 8. Figures 8 and 9 show wavefield snapshots and energy maps, respectively, for scans #5-8 prior to baseline subtraction.

Figure 28 shows snapshots of the residual wavefields for the four notch sizes, in order of increasing notch size, after application of the TSSA method; results are similar for the GSTA method and are not shown. The incremental increase in the scattering as the notch size increases can be clearly seen moving along each row. Performance metrics for both alignment methods and each notch size are compared in Table 9; although baseline subtraction does not result in perfect cancellation of the incident waves, the energy of the residual wavefield is positively correlated with the size of the notch.

Although the residual images show both some baseline wavefield feed-through and minor imaging artifacts, many interesting features of the scattered waves are visible. At 18 μs, a fast longitudinal wave is visible for each notch size that originates from the notch location at 0°. The snapshots also show an artifact near the hole boundary at about 30° that is likely also in the baseline wavefield. For every notch but the 1 mm notch, the start of two scattered shear waves can be seen: one at 0° propagating in the 0° direction and another at 180° propagating in the 180° direction. The wave at 0° is directly scattered from the notch whereas the one at 180° is likely formed by evanescent waves that have traveled around the hole from the notch and reformed as a propagating shear wave, similar to those reported in [17]. These waves are not visible for the 1 mm notch in the 18 μs snapshot. They may be obscured by imaging artifacts, or, since the notch is further from the measurement surface, they may not have yet arrived at the surface. As time progresses, the scattered waves propagate as expected, although the 180° wave never becomes clearly visible for the 1 mm notch.

Table 9: Comparison of the baseline subtraction residual energy of different notch sizes for the transducer oriented at -90°.

Current Scan	Baseline Scan	Description	Alignment Method	Mean Residual Energy (dB)	Peak Residual Energy (dB)
#5	#4	Baseline: No notch Current: 1 mm notch Transducer at -90°	None	-2.9	6.5
#5	#4		GSTA	-16.5	2.8
#5	#4		TSSA	-17.1	-2.9
#6	#4	Baseline: No notch Current: 2 mm notch Transducer at -90°	None	-5.4*	3.7*
#6	#4		GSTA	-15.7*	3.4*
#6	#4		TSSA	-15.7*	2.8*
#7	#4	Baseline: No notch Current: 3 mm notch Transducer at -90°	None	1.4*	14.8*
#7	#4		GSTA	-12.3*	3.1*
#7	#4		TSSA	-12.6*	3.1*
#8	#4	Baseline: No notch Current: 4 mm notch Transducer at -90°	None	1.3	13.9
#8	#4		GSTA	-10.5	3.4
#8	#4		TSSA	-10.8	3.5

*A single noisy measurement was removed prior to calculation.

The three frames shown in Figures 8 and 28 of 18, 19 and 20 μs were selected to highlight scattering of the shear wave with the notch as manifested by the second skip. Since the probe is located 1.5 skips from the bottom edge of the hole, the second skip on the top surface is most strongly influenced by the bottom surface notches. Snapshots of the residual wavefield at different times, although not shown here, illustrate weaker scattering of several other skips. All of the skips interact with the through-hole, as does the Rayleigh wave; although there is some feedthrough of these arrivals, they have been reduced enough by the baseline subtraction to be able to see details of the notch scattering that were not otherwise visible.

The top row of Figure 29 shows the radial energy map for the baseline subtraction

residual using the TSSA method. The radial energy difference, seen on the middle row of Figure 29, was produced by subtracting the radial energy map for the baseline wavefield from the radial energy map for the current wavefield. The radial energy ratio, seen on the top row of Figure 29, was produced by taking the log ratio of the current and baseline measurements. The radial energy maps were obtained using the method described in Section 5.3 for each notch size; the center of the notch in the current measurements was the reference point for the radial B-scans used to calculated the energy. All three energy map types in Figure 29 are colored such that red denotes an increase and blue denotes a decrease in energy of the waves propagating at the velocity and in the direction indicated. The radial energy map for the baseline subtracted residual is a measure of energy and is therefore always a positive quantity. The radial energy difference and ratio can be either positive or negative depending on whether there is an increase or a decrease in the absolute or relative energy. All three energy maps convey similar information; however, the difference (both the energy and baseline subtraction residual) gives an indication of absolute effect of the scatterer and the ratio gives an indication of the relative effect of the scatterer. Figures 30 and 31 provides scattering patterns for each notch size and wave mode–Rayleigh (top), shear (middle), and longitudinal (bottom)–produced using the methodology in Section 5.3 on the baseline subtraction radial energy and radial energy difference, respectively, in Figure 29.

Comparison of the baseline subtraction radial energy maps and the radial energy differences in Figure 29, which should be similar, show some notable differences. The baseline subtraction radial energy map is much smoother and more symmetric than the radial energy difference. Also, producing the radial energy map on the baseline subtraction residual rather than subtracting the radial energy maps results in less baseline feed-through, which is manifested as the asymptotic behavior at 0° and 180°. When producing scattering patterns, the characteristics of the baseline

subtraction radial energy map are superior to those of the radial energy difference as can be seen by comparing Figures 30 and 31. The scattering patterns produced from the baseline subtraction radial energy map are much smoother, match more closely with expected scattering from the defects studied, and produce clear trends in the effect of the increasing notch size.

Both the radial energy difference and ratio show the addition of the notch increases shear wave scattering in backward direction ($-90°$) and decreases shear waves propagating in forward direction ($90°$). The shear wave scattering patterns in Figure 30 confirm this and show the reduction in shear wave scattering in the forward direction is greater than the increase in the backward direction; most likely some of the shear waves propagating in the forward direction prior to the addition of the notch have undergone mode conversion into longitudinal waves following the introduction of the notch, which can be seen in the radial energy difference and ratio maps. Figure 30 shows that the magnitude of both the shear and longitudinal wave scattering is directly proportional to the size of the notch, as expected. Some baseline feed-through can be seen in the baseline subtraction radial energy map and manifests itself in the longitudinal scattering pattern as a slight spike at $5°$. The Rayleigh wave scattering pattern is two orders of magnitude below the shear and longitudinal scattering, which is not surprising since the Rayleigh waves propagate along the surface of the plate and should not be greatly perturbed by the notch. Despite the fact that the notch is not close to the surface, there is a positive correlation between scattered energy in the $0°$ and $90°$ directions and the size of the notch. The scattered Rayleigh waves are likely the result of mode conversion of the scattered shear and longitudinal waves from the notch, as described in [29].

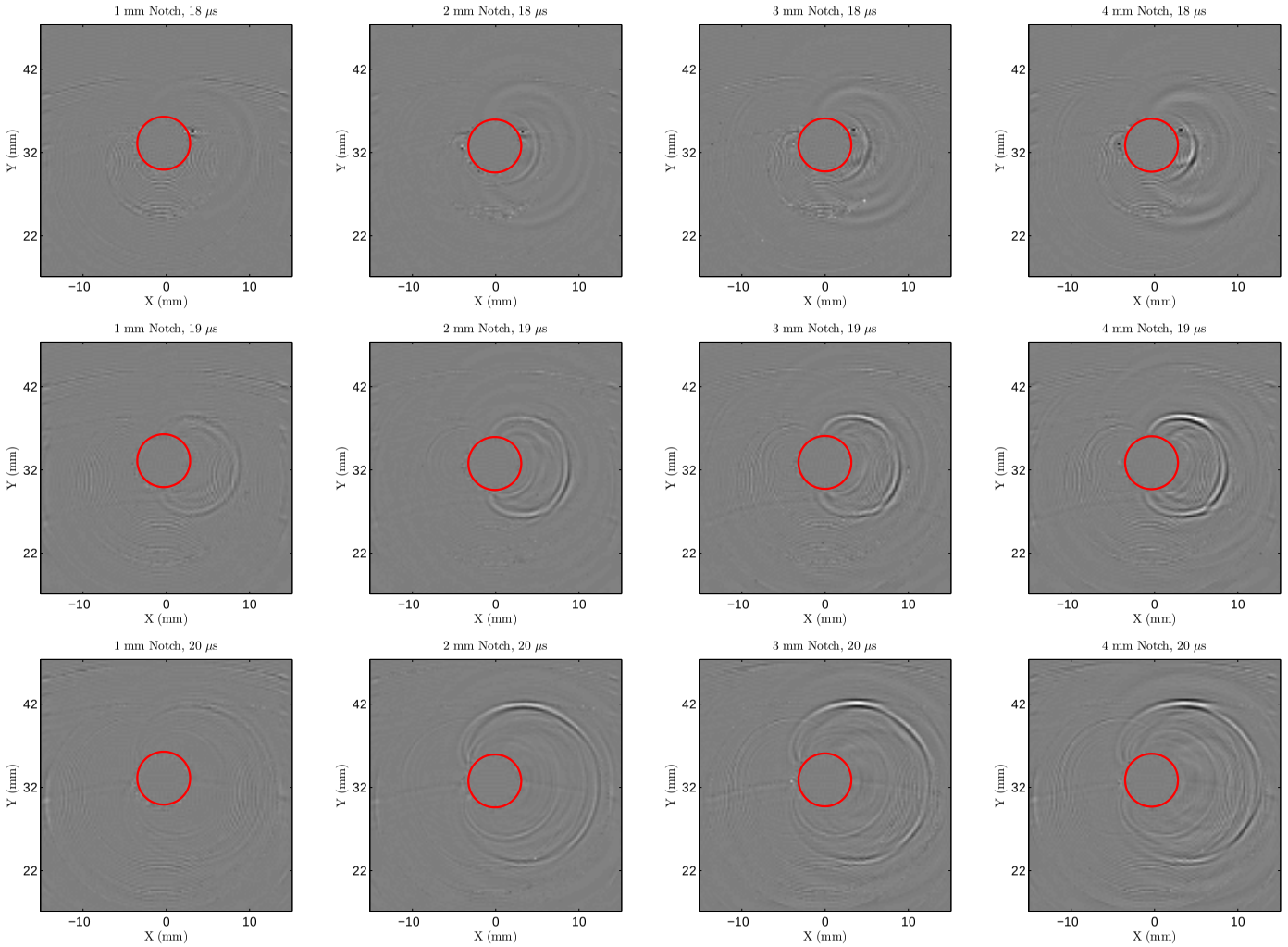

Figure 28: Snapshots at three different times (18, 19, and 20 μs) of the residual wavefield after introduction of a corner notch (scans #5-8) using the no-notch wavefield (scan #4) as the baseline and after baseline alignment with TSSA for the -90° transducer orientation. The edge of the hole is outlined in red.

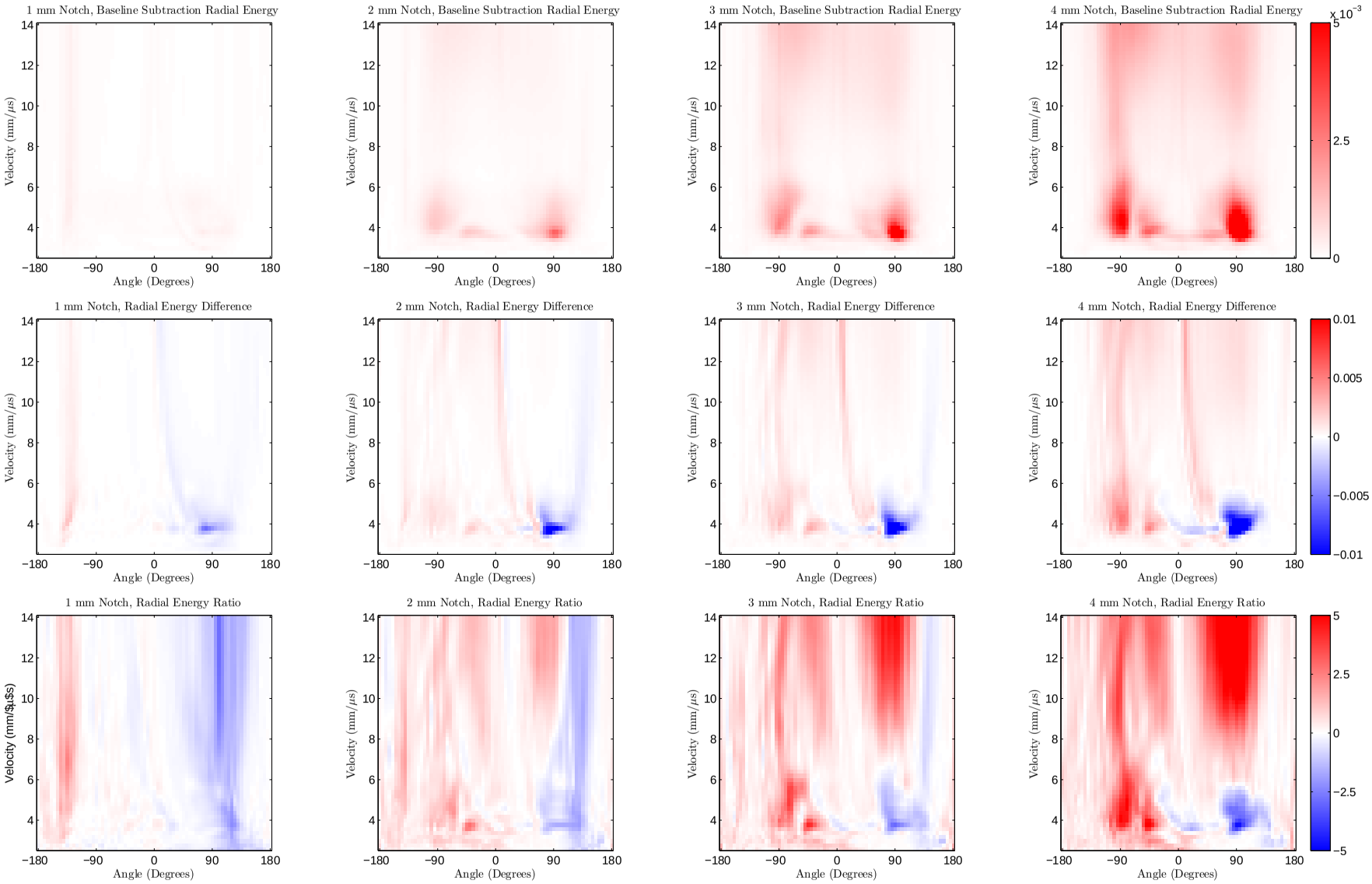

Figure 29: Baseline subtraction radial energy (top) as well as the radial energy differences (middle) and ratios (bottom) for 1-4 mm notches (scans #5-8) using scan #4 as a baseline.

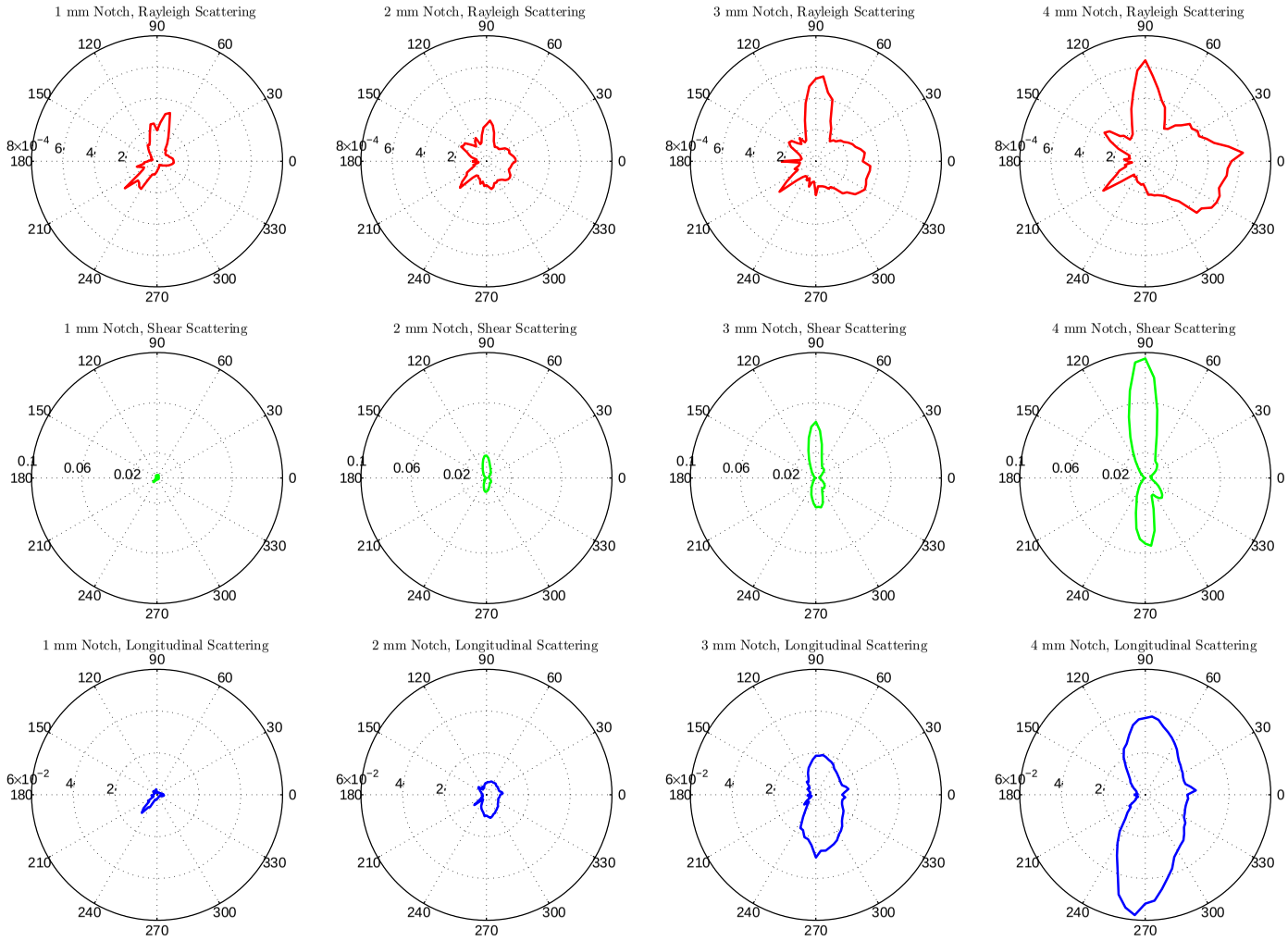

Figure 30: Scattering patterns for each notch size and wave mode obtained by summing over the appropriate velocity ranges in the baseline subtracted radial energy map for the $-90°$ transducer orientation.

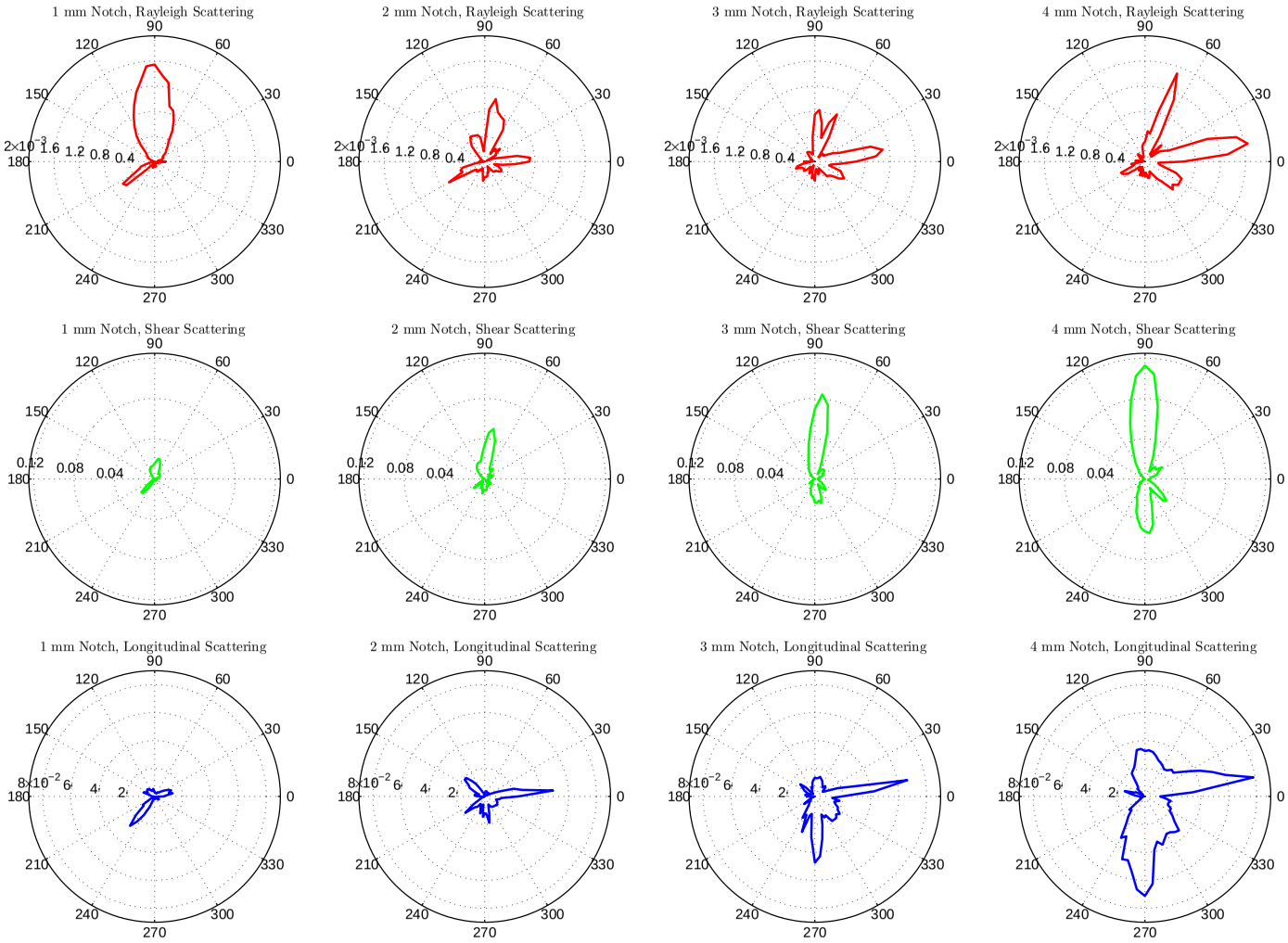

Figure 31: Scattering patterns for each notch size and wave mode obtained by summing over the appropriate velocity ranges in the radial energy difference map for the $-90°$ transducer orientation. The edge of the hole is outlined in red.

6.2.2 45° Transducer Orientation

For the transducer oriented at 45°, baseline subtraction is performed for each notch size using scan #12 as the baseline, snapshots of which can be seen in the left column of Figure 10. Figures 10 and 11 show wavefield snapshots and energy maps, respectively, for scans #13-16 prior to baseline subtraction.

Figure 32 shows snapshots of the residual wavefields for the four notch sizes, in order of increasing notch size, after application of the TSSA method; results are similar for the GSTA method and are not shown. The incremental increase in the scattering as the notch size increases can be clearly seen moving along each row. Performance metrics for both alignment methods and each notch size are compared in Table 10; although baseline subtraction does not result in perfect cancellation of the incident waves, the energy of the residual wavefield is positively correlated with the size of the notch.

The residual images are similar to the snapshots for the −90° transducer orientation in that there is undesirable baseline feed-through and minor imaging artifacts; however, the features of the scattered waves are different. At 16 μs, a longitudinal wave is visible for every notch size that originates from the notch location at 0°. For every notch but the 1 mm notch, a shear wave scattering from the notch at 0° and propagating in the 0° direction along the notch can be seen at 17 μs. The arrival time when this wave reaches the surface of the plate and appears in the wavefield is positively correlated with the size of the notch. At 18 μs several shear waves can be seen emanating from the notch for all notch sizes including the 1 mm notch; the waves are fairly omnidirectional except around the notch at 0°. As these waves propagate, they bend around the edges of the hole.

The top row of Figure 33 shows the radial energy map for the baseline subtraction residual using the TSSA method. The radial energy difference, seen on the middle row of Figure 33, was produced by subtracting the radial energy map for the baseline

Table 10: Comparison of the baseline subtraction residual energy of different notch sizes for the transducer oriented at 45°.

Current Scan	Baseline Scan	Description	Alignment Method	Mean Residual Energy (dB)	Peak Residual Energy (dB)
#13	#12	Baseline: No notch Current: 1 mm notch Transducer at 45°	None	-8.2	5.5
#13	#12		GSTA	-16.1	0.6
#13	#12		TSSA	-16.2	0.3
#14	#12	Baseline: No notch Current: 2 mm notch Transducer at 45°	None	-10.0	2.1
#14	#12		GSTA	-10.4	1.0
#14	#12		TSSA	-10.6	0.7
#15	#12	Baseline: No notch Current: 3 mm notch Transducer at 45°	None	-2.7	9.5
#15	#12		GSTA	-10.4	1.3
#15	#12		TSSA	-10.4	1.3
#16	#12	Baseline: No notch Current: 4 mm notch Transducer at 45°	None	-4.6	6.2
#16	#12		GSTA	-8.8	4.0
#16	#12		TSSA	-8.8	2.9

*A single noisy measurement was removed prior to calculation.

wavefield from the radial energy map for the current wavefield. The radial energy ratio, seen on the top row of Figure 29, was produced by taking the log ratio of the current and baseline measurements. The radial energy maps were obtained using the method described in Section 5.3 for each notch size; the center of the notch in the current measurements was the reference point for the radial B-scans used to calculated the energy. Figures 34 and 35 show the corresponding scattering patterns for each notch size and wave mode: Rayleigh (top), shear (middle), and longitudinal (bottom) obtained from the baseline subtraction radial energy map and the radial energy difference, respectively. These maps are the same as those described in Section 6.2.1, only for the transducer oriented at 45°. Similar to those for the −90° transducer

orientation, the scattering patterns produced from the the baseline subtraction radial energy map are of better quality.

The baseline subtraction radial energy and the radial energy difference both show shear wave scattering from the notch at angles between $-90°$ and $90°$ for the 2, 3, and 4 mm notches. The velocities of the scattered shear waves at the angles between $-45°$ and $45°$ vary smoothly from 3.6 mm/μs to 6.0 mm/μs, suggesting the waves scattered parallel to the notch at $0°$ are scattered at a larger refracted angle. These waves are fairly directional and can be clearly seen in the 17 μs snapshots of Figure 32. The shear waves at 18 μs scatter much more omnidirectionally except for in the vicinity of the notch at $0°$ where there is a slight reduction in amplitude. These waves, which bend around the hole as they propagate, account for much of the energy in the shear wave scattering pattern between $-120°$ and $120°$. The shear waves scattering in these directions are accompanied by longitudinal scattering, which can be seen in the baseline subtraction radial energy and the longitudinal wave scattering pattern. The longitudinal scattering is the result of shear waves undergoing mode conversion. The angle of the incident wave relative to the notch results in a stronger longitudinal wave scattering perpendicular to the notch, which results in the increased scattering at $90°$ seen in the scattering pattern. Looking at both the radial energy maps and the scattering patterns it is clear the magnitude of both the shear and longitudinal wave scattering is proportional to the notch size.

Although it is several orders of magnitude below the shear and longitudinal scattering, there is also Rayleigh wave scattering in the direction parallel to the notch at $0°$. With the exception of the 3 mm notch the Rayleigh wave scattering is proportional to the notch size as well. The reduction in Rayleigh wave scattering for the 3 mm notch could be the result of coherent interaction of secondary scattering between the notch and the hole, which would also account for the similar levels of residual energy

seen in Table 10 for the 2 mm and 3 mm notches. In cases like this where different wave modes are propagating in the same direction, the velocity/refracted angle ambiguity can make it difficult to distinguish different wave modes using only time domain methods; however, the different wave modes can be reliably identified using the radial energy maps and scattering patterns.

In addition to the scattering radiating out from the notch, there is also a reduction in forward shear wave scattering in the $-135°$ direction. This reduction in forward scattering is clearly visible in the baseline subtraction radial energy and radial energy difference at every notch size, except for the 1 mm notch. It is less clear in the corresponding radial energy ratios. The reduction in forward scattering is only visible in the 3 and 4 mm shear wave scattering patterns. The reduction in the forward scattering should be a function of the notch size, i.e., a larger notch size should should prevent more of the waves from propagating around the hole. Although it can be clearly seen in the radial energy map, the reduction in forward scattering is not evident in the 2 mm notch scattering pattern because it blends into the rest of the scattering pattern.

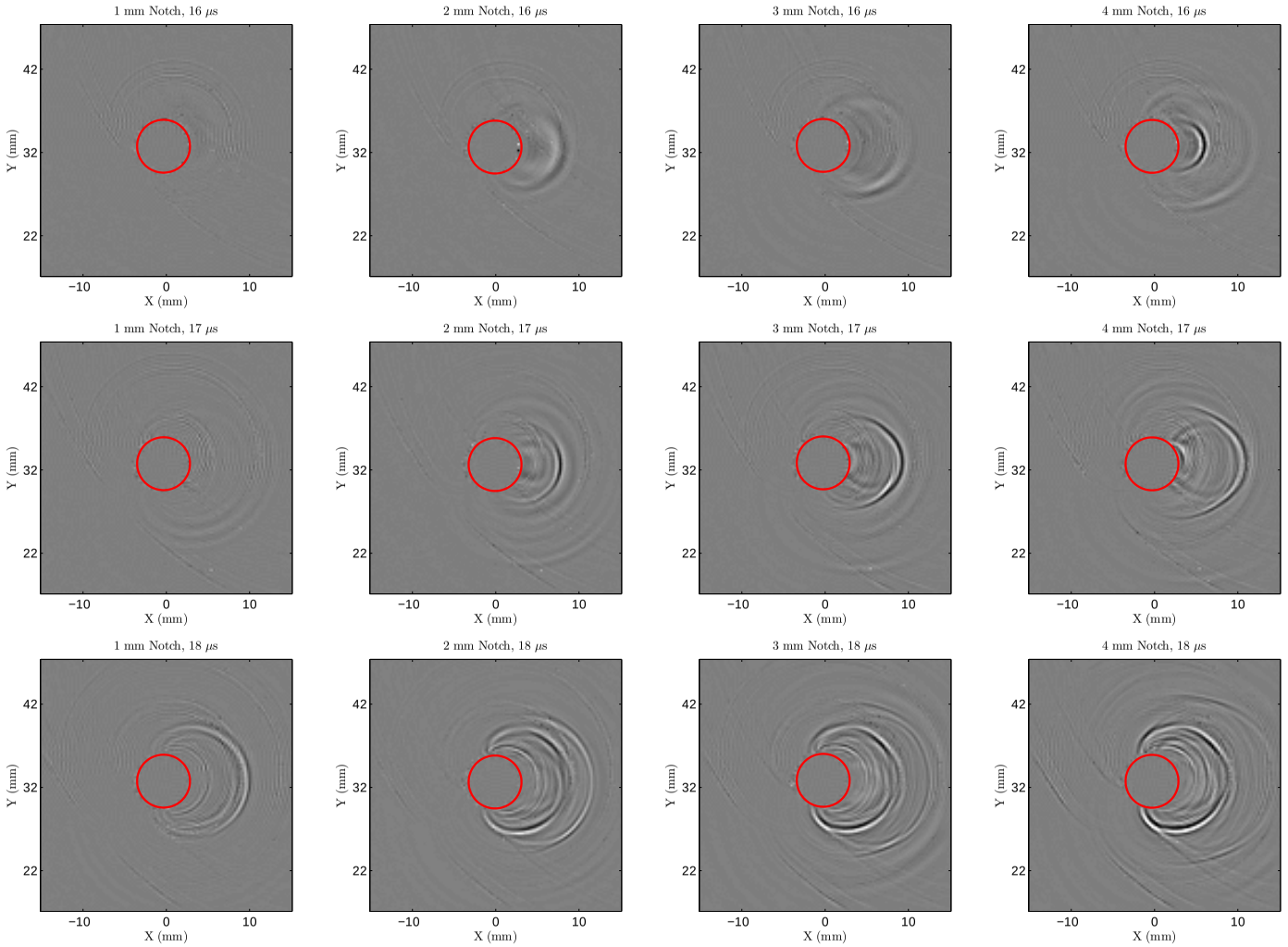

Figure 32: Snapshots at three different times (16, 17, and 18 μs) of the residual wavefield after introduction of a corner notch using the no-notch wavefield as the baseline and after baseline alignment with TSSA for the 45° transducer orientation. The edge of the hole is outlined in red.

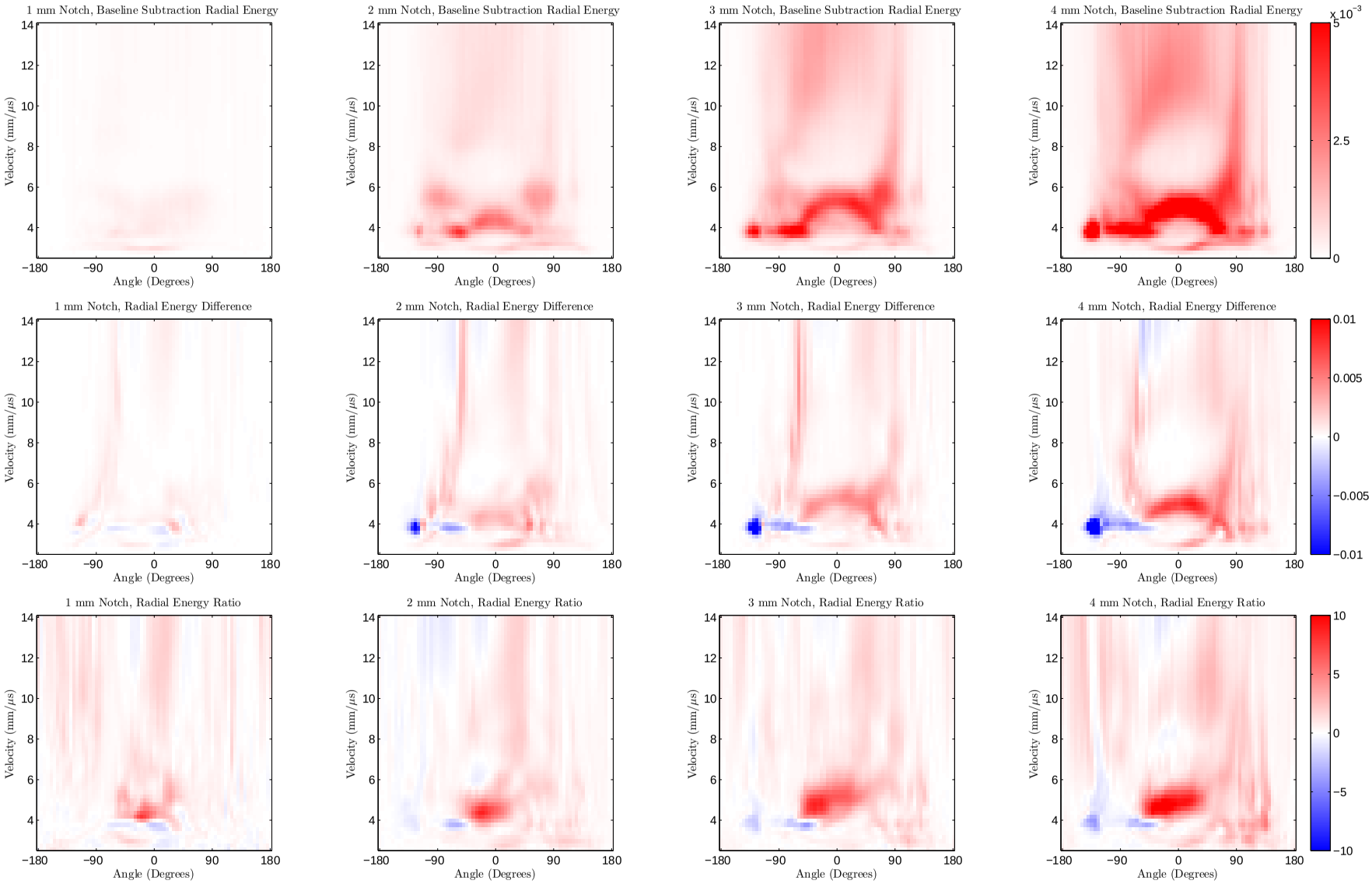

Figure 33: Baseline subtraction radial energy (top) as well as the radial energy differences (middle) and ratios (bottom) for 1-4 mm notches (scans #13-16) using scan #12 as a baseline.

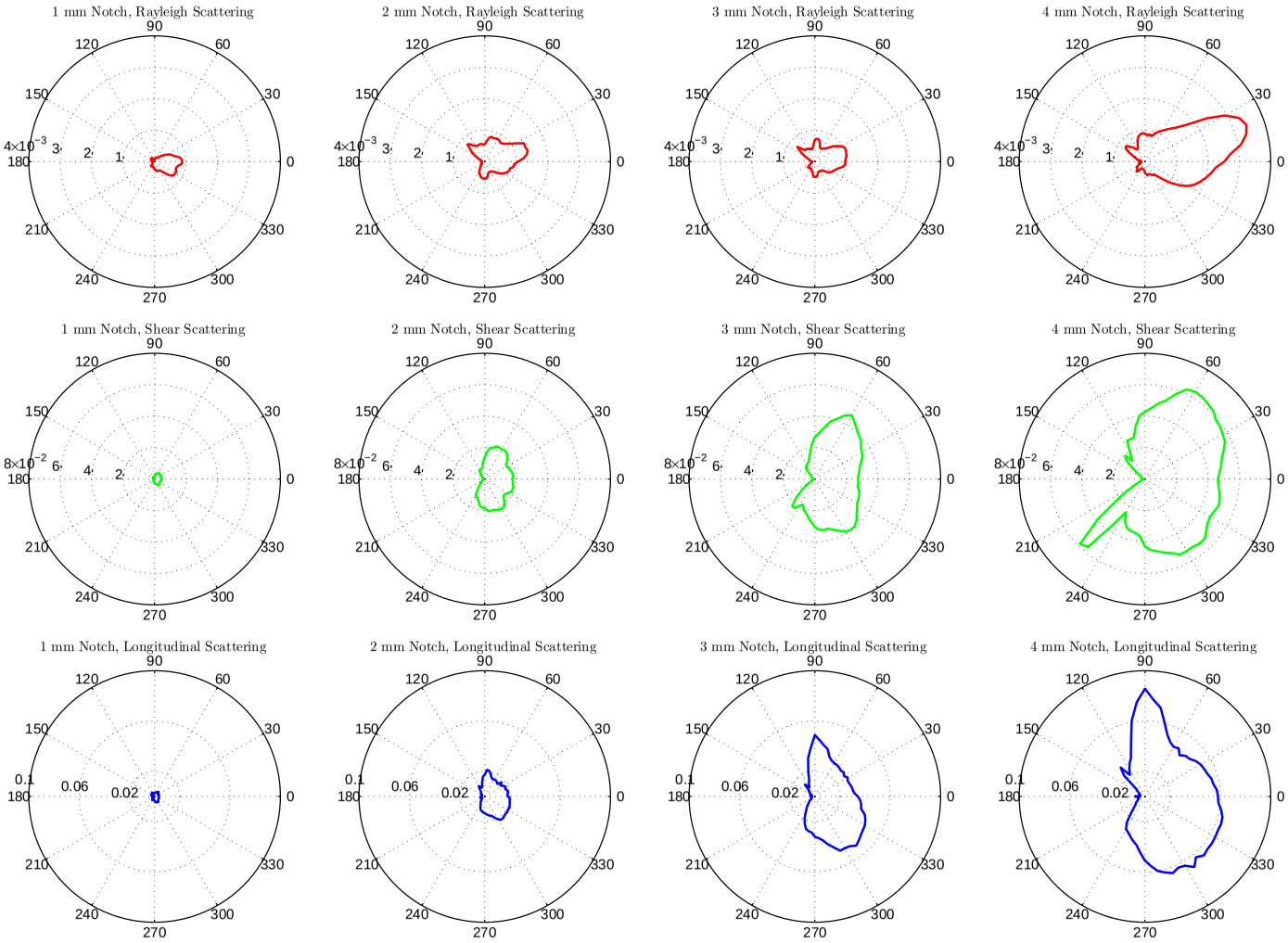

Figure 34: Scattering patterns for each notch size and wave mode obtained by summing over the appropriate velocity ranges in the baseline subtraction radial energy map for the 45° transducer orientation.

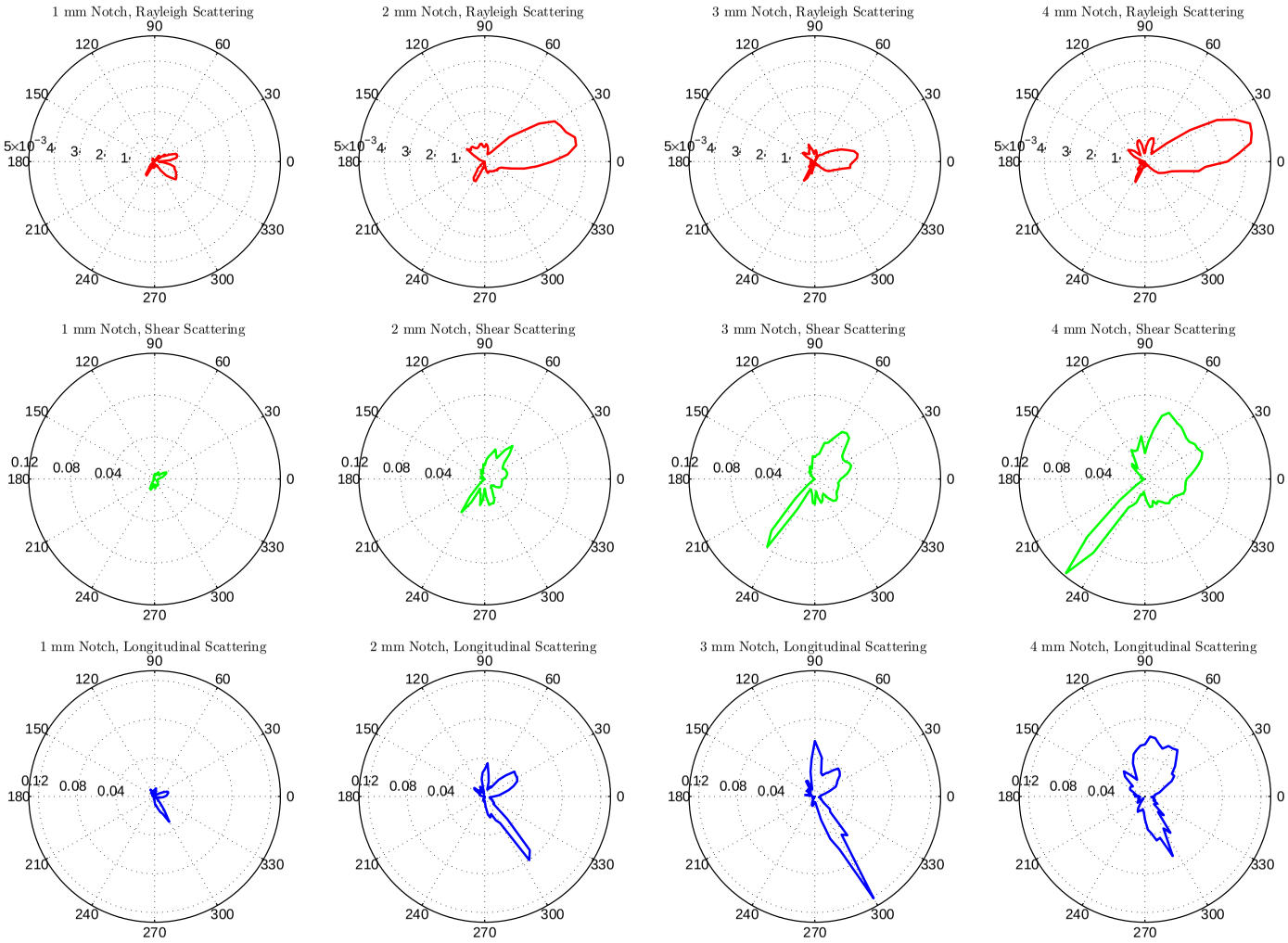

Figure 35: Scattering patterns for each notch size and wave mode obtained by summing over the appropriate velocity ranges in the radial energy difference map for the 45° transducer orientation.

6.2.3 Effect of Transducer Orientation on Scattering

The performance of angle-beam ultrasonic NDE is dependent on the placement and orientation of the probe relative to the defect. Comparison of the scattering patterns for the two transducer orientations in Figures 31 and 35 gives an indication of the significant change in scattering that results from a change in the transducer orientation. The scattering from the notch is more directional when the transducer is oriented at $-90°$ rather than at $45°$ relative to the notch, especially for the shear wave scattering. The shear wave scattering for the $-90°$ orientation is almost completely oriented in the forward and backward directions with some small sidelobes at $\pm 45°$. The shear wave scattering for the $45°$ orientation, on the other hand, scatters fairly uniformly at angles between $-120°$ and $120°$, bending around the hole as it scatters. The longitudinal scattering for both transducer orientations is similar in shape; it emanates out from the notch at angle between $-120°$ and $120°$. The notable difference in the longitudinal scattering between the two orientations is the angle of strongest scattering. For the $-90°$ orientation, the strongest scattering is in the $-90°$ direction, and for the $45°$ orientation, the strongest scattering is in the $90°$ direction. The Rayleigh wave scattering for both orientations is also similar; however, the $-90°$ orientation has a strong forward scattered component in the $90°$ direction.

Generally, angle-beam NDE is performed in a pulse-echo configuration, which requires scattered energy to return to the angle-beam transducer to detect a defect. Comparing the scattered energy in the direction of the transducer can assess the relative performance of each orientation. The scattered shear waves in the direction of the transducer is slightly larger at 0.08 for the $45°$ orientation than for the $-90°$ orientation at 0.06. The longitudinal scattering is almost identical at 0.58 for both orientations. Traditionally inspectors attempt to detect cracks in through-holes by orienting the transducer at $45°$ relative to the crack. The scattering plots generated here support this methodology. Also, cracks emanating from through-holes are

generally located by scanning the angle-beam probe around the hole. The more omnidirectional nature of the scattering pattern at the 45° allows for a greater margin of error than if the transducer was oriented at 90°. Scattering studies such as these can guide detection methodologies employing angle-beam waves.

6.3 Discussion of Methodology Efficacy

The measurement of scattering is in general challenging, especially when the scatterer of interest exists in the presence of a geometric feature, such is the case for the crack-like notch emanating from a through-hole studied here. Both the radial energy maps in Figures 29 and 33 and the scattering patterns in Figures 30 and 34 provide a great deal of information about scattering from the notch either in isolation or relative to the scattering from the hole. Although these plots contain artifacts from imperfect baseline subtraction, such as incident wave feed-through, they can still be used to quantify the scattering behavior of the notch and demonstrate the ways in which that behavior changes as a function of the notch size.

The methodology presented here, which combines the use of wavefield alignment, baseline subtraction, and radial energy estimation in the frequency-wavenumber domain, allows for the detailed characterization of angle-beam scattering and presents several advantages over existing methods. First, the use of wavefield imaging to study scattering addresses one of the unavoidable shortcomings of using discrete transducers for generating scattering patterns: the paucity of sampling points. Second, the ability to align the wavefields in both time and space prior to subtraction allows for much better removal of incident waves than can often be achieved with other methods of scattering characterization. Wavefield baseline subtraction allows for reasonable removal of scattering from structural features to characterize scatters that are additions to these features. Third, performing the scattering characterization in the frequency-wavenumber domain produces some inherent filtering, which further

removes the incident waves and allows for the scattering of different wave modes to be isolated and studied. Additionally, studying scattering as a function of both angle and wave velocity provides information about mode conversion that is difficult to obtain with existing scattering pattern methodologies. Lastly, wavefield imaging has been employed to study ultrasonic wave propagation and scattering in a variety of scenarios; the techniques presented here are not limited to the study of angle-beam scattering and could be applied to other wavefield measurements.

Despite the numerous advantages, there are several challenges to the use of these methods to characterize scattering. First, the acquisition and analysis of wavefield data is time consuming and computationally intensive. Second, because of the necessity of a constant temperature environment and the restrictions of the wavefield scanner itself, the methods presented here are practically limited to being performed under laboratory conditions. Third, even with application of the baseline subtraction alignment methods, there are baseline feed-through artifacts which distort the scattering patterns generated from the wavefield data. Keeping these benefits and challenges in mind, it is clear to see how the methods presented here can be used to robustly characterize angle-beam scattering and provide insights that can be used to guide the development of NDE techniques and to validate ultrasonic models.

CHAPTER VII

CONCLUSIONS AND RECOMMENDATIONS

7.1 Conclusions

Described in this thesis are experimental procedures for recording ultrasonic angle-beam wavefields in the 1-10 MHz frequency range using a laser vibrometer followed by a methodology to characterize scattering behavior using baseline subtraction of the measured wavefields. Intermediate to this goal, angle-beam wave propagation in undamaged plates was investigated through experimental studies, ray-tracing models, and 2-D FE models. These preliminary studies provide a clear understanding of the properties of angle-beam waves and reveal some of the complications of analyzing angle-beam wave propagation. These complications arise from the reflection of the waves between the surfaces of the plate, which culminates in the hyperbolic trajectories in space/time and ambiguities in velocity/refracted angle. In addition to these complications, a propagating Rayleigh wave doublet, which is typically not discussed in traditional angle-beam studies, was identified. From the 2-D FE model it was determined that the Rayleigh wave doublet originates from mode conversion at the wedge/plate interface and from shear wave interaction with the corner of the wedge. Deeper understanding of angle-beam wave propagation and the challenges associated with analyzing these waves help guide the development of methods to characterize angle-beam scattering.

The isolation of scattering behavior is essential to the characterization methods presented in this work; alignment of the baseline wavefield to the current wavefield in both space and time prior to subtraction allows for sufficient suppression of incident waves to study scattering in isolation. Both of the proposed baseline subtraction

methodologies, global space-time alignment (GSTA) and time slice spatial alignment (TSSA), are shown to be capable of removing the baseline wavefield to a sufficient degree to visualize small amplitude waves scattered from far-surface notches emanating from through-holes. The smallest notch (1 mm) is comparable in length to the shear wavelength at the center frequency of 5 MHz, which is about 0.6 mm. The isolation of scattered waves achieved by wavefield baseline subtraction allows for visualization of the effect of scatterers in addition to providing qualitative information.

The isolation of the scattering behavior also allows for the development of new wavefield-based means of quantifying scattering to be used for defect characterization. The radial energy maps are able to quantify scattering as a function of both the scattered angle and the phase velocity. Using these maps, scattering of different wave modes and mode conversion can be studied. The radial energy maps can be transformed into scattering patterns, providing a means of quantifying scattering that is of interest to ultrasonic community. Both the radial energy maps and the scattering patterns are used to rigorously characterize scattering from corner notches. Scattering patterns were produced for all three wave modes common in angle-beam ultrasonic testing: Rayleigh, shear, and longitudinal for two transducer orientations. The effect of notch size on scattering is as expected; the scattering pattern shape is roughly the same for every notch size, but larger notches scatter more energy. Also the transducer orientation with respect to the notch has a profound effect on the shape of the scattering pattern. Of the two transducer orientations investigated here, the $-90°$ orientation produced a much more directional scattering pattern than the $45°$ orientation.

Although the alignment methods presented here are applied to angle-beam shear waves, the techniques are generally applicable to any 3-D wavefield data, such as

those commonly measured for guided waves. Regardless of the application, successful isolation of scattered wavefields permits better characterization of defects by removing interfering incident waves. This problem is particularly difficult when the base structure already contains a scatterer, such as was the case here for the initial through-hole. The ability to study the scattered waves in isolation allows for better quantification and characterization of scattering phenomena than would otherwise be possible, which can be used to improve ultrasonic NDE methods and models.

In conclusion, this work has met its main objective by providing the following contributions: a reliable means for high-resolution measurement of angle-beam wavefields in plates; a framework for the analysis of angle-beam wavefield data; a method for characterizing scattering behavior by isolating scattered waves from full wavefield data via baseline subtraction; and a method for generating angle-beam scattering patterns from wavefield data.

7.2 Recommendations for Future Work

Although, the work performed to date has established a systematic methodology to measure, analyze, and characterize angle-beam wave propagation and scattering using wavefield data, a considerable amount of work remains to both study a wider array of ultrasonic defects using the methods presented here and to improve the methods themselves. The remainder of this section provides recommendations for the direction of future work studying different scattering scenarios, improving the methodology, and exploring alternatives to baseline subtraction for isolating scattered waves.

7.2.1 Analyze a Variety of Scattering Scenarios

Methods for reliable separation and characterization of ultrasonic waves have been developed and must be tested on a variety of ultrasonic defect configurations to ensure that they provide meaningful information about the nature of the scattering behavior. The experimental aspect of the future work should focus on developing meaningful

experiments that mimic real-world ultrasonic defects or that provide insight for ultrasonic wave propagation models. Common defects found in aerospace structures such as cracks emanating from fastener holes and welds should be the focus of experiments to characterize real-world defects. Additional experiments should focus on the effects of boundary conditions on wave propagation and scattering. The experimental and analytical aspects of these studies have the potential to work together to provide a more complete, characterized picture of wave propagation that will benefit the ultrasonic NDE community at large.

7.2.2 Improve Methodology for Scattering Characterization

Although the methodology presented here can successfully isolate and characterize scattered waves, there are several areas that could be improved. First the number of degrees-of-freedom for the alignment methods could be increased to include scale and rotation, at the expense of increased computation, to improve the incident wave removal using baseline subtraction. Baseline subtraction could also be improved by manipulating the amplitude of the baseline prior to subtraction through energy normalization or histogram reweighting. With any manipulation of the baseline, care must be taken to not reduce the effect of the scatterer. In addition to improving the isolation of the scattered waves, it would also be beneficial to be able to isolate specific V-paths so that the scattering from different wave arrivals could be studied separately. Second, alternative methods to using the radial B-scans for producing the radial energy maps and the subsequent scattering patterns should be explored. Most obviously, the radial energy maps could be produced directly in the 3-D frequency-wavenumber domain rather then from the 2-D frequency-wavenumber domain of the radial B-scans. Calculating the energy in the 3-D frequency-wavenumber domain would eliminate the need to interpolate the radial B-scans in the time-space domain and may produce more accurate measurements of the energy. Lastly, for the sake of

presentation and to make comparison with ultrasonic models more straightforward, it may be beneficial to apply some smoothing or approximation to the scattering patterns generated from the baseline subtraction residual as was done in [87].

7.2.3 Explore Alternatives to Baseline Subtraction for Wave Separation

Although baseline subtraction has proven to be a useful technique for the separation of incident and scattered waves, it would be beneficial to develop a method that is able to perform wave separation in the absence of a well-matched baseline. There are several promising methods, borrowed from the field of image processing, that may be able to separate incident and scattered waves in wavefield images. The first method would treat the scattered waves as areas of undesired image corruption in an otherwise pristine image. Sparse low-rank texture repair algorithms [115] and corrupt matrix recovery algorithms [116] could then be applied to remove the scattered waves. The challenge to this approach would be developing a method to robustly identify the scattered waves as corruption. Another method that may prove promising is image segmentation using boundary compression; however, such methods would be highly dependent on the degree in which incident and scattered waves form boundaries in the images [117]. The challenges associated with both methods may be mitigated by leveraging the availability of a baseline image, even a mismatched one, which may allow for global identification of scattering that can then be isolated locally.

REFERENCES

[1] U.S. Homeland Security: Science and Technology Directorate, *Aging Infrastructure: Issues, Research, and Technology*, 2010.

[2] U.S. Air Force Scientific Advisory Board, *Sustaining Air Force Aging Aircraft into the 21st Century*, 2011.

[3] A. Jardine, D. Lin, and D. Banjevic, "A review on machinery diagnostics and prognostics implementing condition-based maintenance," *Mechanical Systems and Signal Processing*, vol. 20, pp. 1483–1510, 2006.

[4] T. E. Michaels and J. E. Michaels, "Application of acoustic wavefield imaging to non-contact ultrasonic inspection of bonded components," in *AIP Conference Proceedings*, vol. 820, p. 1484, 2006.

[5] J. Takatsubo, B. Wang, H. Tsuda, and N. Toyama, "Generation laser scanning method for the visualization of ultrasounds propagating on a 3-D object with an arbitrary shape," *Journal of Solid Mechanics and Materials Engineering*, vol. 1, no. 12, pp. 1405–1411, 2007.

[6] A. J. Dawson, J. E. Michaels, and T. E. Michaels, "Acquisition and baseline subtraction of angle-beam ultrasonic wavefield data," *Mechanical Systems and Signal Processing*, 2015. Submitted for publication.

[7] A. J. Dawson, J. E. Michaels, R. M. Levine, X. Chen, and T. E. Michaels, "Acquisition and analysis of angle-beam wavefield data," in *AIP Conference Proceedings*, vol. 1581, pp. 1716–1723, 2014.

[8] A. J. Dawson, J. E. Michaels, and T. E. Michaels, "Challenges in the separation and analysis of scattered waves in angle-beam wavefield data," in *AIP Conference Proceedings*, vol. 1650, pp. 827–834, 2015.

[9] A. J. Dawson, J. E. Michaels, and T. E. Michaels, "Modeling and measurement of angle-beam wave propagation in a scatterer-free plate," in *AIP Conference Proceedings*, 2016. Submitted for publication.

[10] J. W. Kummer, A. J. Dawson, and J. E. Michaels, "A methodology for estimating scattering patterns of empty and filled through-holes from angle-beam wavefield measurements," 2015. Submitted for clearance to Air Force Research Laboratory (AFRL).

[11] L. Rayleigh, "On waves propagated along the plane surface of an elastic solid," *Proceedings of the London Mathematical Society*, vol. 1, no. 1, pp. 4–11, 1885.

[12] H. Lamb, "On waves in an elastic plate," *Proceedings of the Royal Society of London. Series A*, vol. 93, no. 648, pp. 114–128, 1917.

[13] R. Stoneley, "Elastic waves at the surface of separation of two solids," *Proceedings of the Royal Society of London. Series A, Containing Papers of a Mathematical and Physical Character*, vol. 106, no. 738, pp. 416–428, 1924.

[14] J. L. Rose, *Ultrasonic Waves in Solid Media*. New York: Cambridge University Press, 1999.

[15] P. J. Shull, ed., *Nondestructive Evaluation: Theory, Techniques, and Applications*. New York: Marcel Dekkerl, 2002.

[16] The Collaboration for NDT Education: Iowa State University, *NDT Education Resource Center*, Accessed: Dec. 20, 2013. url: `http://www.ndt-ed.org/index_flash.htm`.

[17] C. J. Hellier, ed., *Handbook of Nondestructive Evaluation*. New York: McGraw-Hill, 2001.

[18] D. Cook and Y. Berthelot, "Detection of small surface-breaking fatigue cracks in steel using scattering of Rayleigh waves," *NDT & E International*, vol. 34, no. 7, pp. 483 – 492, 2001.

[19] R. Edwards, S. Dixon, and X. Jian, "Depth gauging of defects using low frequency wideband Rayleigh waves," *Ultrasonics*, vol. 44, no. 1, pp. 93 – 98, 2006.

[20] I. A. Viktorov, *Rayleigh and Lamb waves: Physical Theory and Applications*. Plenum press New York, 1967.

[21] V. Giurgiutiu, "Tuned Lamb wave excitation and detection with piezoelectric wafer active sensors for structural health monitoring," *Journal of Intelligent Material Systems and Structures*, vol. 16, pp. 291–305, 2005.

[22] A. Raghavan and C. E. Cesnik, "Review of guided-wave structural health monitoring," *Shock and Vibration Digest*, vol. 39, no. 2, pp. 91–116, 2007.

[23] J. E. Michaels, "Detection, localization, and characterization of damage in plates with an *in situ* array of spatially distributed ultrasonic sensors," *Smart Materials and Structures*, vol. 17, no. 3, p. 035035, 2008.

[24] D. N. Alleyne and P. Cawley, "Optimization of Lamb wave inspection techniques," *NDT & E International*, vol. 25, no. 1, pp. 11–22, 1992.

[25] P. Wilcox, M. Lowe, and P. Cawley, "The effect of dispersion on long-range inspection using ultrasonic guided waves," *NDT & E International*, vol. 34, no. 1, pp. 1–9, 2001.

[26] D. Bray and R. Stanley, *Nondestructive Evaluation: A Tool in Design, Manufacturing and Service*. Taylor & Francis, 1996.

[27] A. McNab and M. Campbell, "Ultrasonic phased arrays for nondestructive testing," *NDT International*, vol. 20, no. 6, pp. 333 – 337, 1987.

[28] S. C. Wooh and Y. Shi, "Optimum beam steering of linear phased arrays," *Wave Motion*, vol. 29, no. 3, pp. 245–265, 1999.

[29] M. Silk, "The transfer of ultrasonic energy in the diffraction technique for crack sizing," *Ultrasonics*, vol. 17, no. 3, pp. 113 – 121, 1979.

[30] F. Ravenscroft, K. Newton, and C. Scruby, "Diffraction of ultrasound by cracks: comparison of experiment with theory," *Ultrasonics*, vol. 29, no. 1, pp. 29 – 37, 1991.

[31] M. Musgrave, *Crystal Acoustics: Introduction to the Study of Elastic Waves and Vibrations in Crystals*. San Francisco: Holden-Day, 1970.

[32] H. Pollard, *Sound Waves in Solids*. New York: Pion, 1977.

[33] L. Schmerr, *Fundamentals of Ultrasonic Nondestructive Evaluation: A Modeling Approach*. New York: Springer US, 1998.

[34] J. C. Aldrin, M. P. Blodgett, E. A. Lindgren, G. J. Steffes, and J. S. Knopp, "Scattering of obliquely incident shear waves from a cylindrical cavity," *Journal of the Acoustical Society of America*, vol. 129, no. 6, pp. 3661–3675, 2011.

[35] H. Jeong and L. W. Schmerr, "Ultrasonic transducer fields modeled with a modular multi-Gaussian beam and application to a contact angle beam testing," *Research in Nondestructive Evaluation*, vol. 19, no. 2, pp. 87–103, 2008.

[36] L. J. Bond, "Methods for the computer modeling of ultrasonic waves in solids," in *Research Techniques in Nondestructive Testing* (R. Sharpe, ed.), vol. VI, Academic Press, 1982.

[37] R. Ludwig and W. Lord, "A finite-element formulation for the study of ultrasonic NDT systems," *IEEE Transactions on Ultrasonics, Ferroelectrics, and Frequency Control*, vol. 35, no. 6, pp. 809–820, 1988.

[38] J. Zhang, B. Drinkwater, and P. Wilcox, "Comparison of ultrasonic array imaging algorithms for nondestructive evaluation," *IEEE Transactions on Ultrasonics, Ferroelectrics, and Frequency Control*, vol. 60, no. 8, pp. 1732–1745, 2013.

[39] M. V. Felice, A. Velichko, and P. D. Wilcox, "Accurate depth measurement of small surface-breaking cracks using an ultrasonic array post-processing technique," *NDT & E International*, vol. 68, pp. 105–112, 2014.

[40] B. Ghose, K. Balasubramaniam, C. Krishnamurthy, and A. S. Rao, "Two dimensional FEM simulation of ultrasonic wave propagation in isotropic solid media using COMSOL," in *COMSOL Conference*, 2010.

[41] T. Kimura and S. Wadaka, "Simulation of ultrasonic fields and echoes obtained using angle beam transducer by hybrid FDTD method," *E-Journal of Advanced Maintenance*, vol. 3, no. 1, pp. 11–24, 2011.

[42] T. Kimura, K. Misu, S. Wadaka, and M. Koike, "A new hybrid model to calculate echoes and ultrasonic fields scattered by flaws combining FDTD method with Rayleigh integral," *IEICE Transactions on Fundamentals of Electronics, Communications and Computer Sciences*, vol. E90-A, no. 7, pp. 1366 – 1375, 2007.

[43] S. Banerjee and T. Kundu, "Ultrasonic field modeling in plates immersed in fluid," *International Journal of Solids and Structures*, vol. 44, no. 18-19, pp. 6013–6029, 2007.

[44] W. Choi, E. Skelton, M. J. S. Lowe, R. Craster, and P. Rajagopal, "Generic hybrid models for three-dimensional ultrasonic NDE," *AIP Conference Proceedings*, vol. 1430, no. 1, pp. 126–133, 2012.

[45] CEA, *CIVA*, Accessed: May 29, 2015. url: `http://www-civa.cea.fr/en/`.

[46] P. Calmon, S. Mahaut, S. Chatillon, and R. Raillon, "CIVA: An expertise platform for simulation and processing NDT data," *Ultrasonics*, vol. 44, Supplement, pp. e975 – e979, 2006. Proceedings of Ultrasonics International (UI'05) and World Congress on Ultrasonics (WCU).

[47] D. Hopkins, M. Datuin, J. Aldrin, D. Forsyth, M. Warchol, and L. Warchol, "Damage localization using ultrasonic methods in multi-layered metallic structures," *AIP Conference Proceedings*, vol. 1650, pp. 817–826, 2015.

[48] R. Miorelli, C. Reboud, T. Theodoulidis, N. Poulakis, and D. Lesselier, "Efficient modeling of ECT signals for realistic cracks in layered half-space," *IEEE Transactions on Magnetics*, vol. 49, no. 6, pp. 2886–2892, 2013.

[49] T. E. Michaels, J. E. Michaels, B. Mi, and M. Ruzzene, "Damage detection in plate structures using sparse ultrasonic transducer arrays and acoustic wavefield imaging," in *AIP Conference Proceedings*, vol. 760, pp. 938–945, 2005.

[50] W. Staszewski, B. Lee, L. Mallet, and F. Scarpa, "Structural health monitoring using scanning laser vibrometry: I. Lamb wave sensing," *Smart Materials and Structures*, vol. 13, no. 2, pp. 251–260, 2004.

[51] P. Castellini, M. Martarelli, and E. Tomasini, "Laser Doppler vibrometry: development of advanced solutions answering to technology's needs," *Mechanical Systems and Signal Processing*, vol. 20, no. 6, pp. 1265–1285, 2006.

[52] J. A. Scales and A. E. Malcolm, "Laser characterization of ultrasonic wave propagation in random media," *Phys. Rev. E*, vol. 67, p. 046618, 2003.

[53] D. Algernon, B. Gräfe, F. Mielentz, B. Köhler, and F. Schubert, "Imaging of the elastic wave propagation in concrete using scanning techniques: application for impact-echo and ultrasonic echo methods," *Journal of Nondestructive Evaluation*, vol. 7, pp. 83–97, 2008.

[54] S. Yashiro, N. Toyama, J. Takatsubo, and T. Shiraishi, "Laser-generation based imaging of ultrasonic wave propagation on welded steel plates and its application to defect detection," *Materials Transactions*, vol. 51, no. 11, pp. 2069–2075, 2010.

[55] H. Sohn, D. Dutta, J. Yang, H. Park, M. DeSimio, S. Olson, and E. Swenson, "Delamination detection in composites through guided wave field image processing," *Composites Science and Technology*, vol. 71, no. 9, pp. 1250–1256, 2011.

[56] M. D. Rogge and C. A. C. Leckey, "Local guided wavefield analysis for characterization of delaminations in composites," in *AIP Conference Proceedings*, vol. 1511, pp. 963–970, 2013.

[57] Y. Fukushima, O. Nishizawa, and H. Sato, "A performance study of a laser Doppler vibrometer for measuring waveforms from piezoelectric transducers," *IEEE Transactions on Ultrasonics, Ferroelectrics, and Frequency Control*, vol. 56, no. 7, pp. 1442–1450, 2009.

[58] J. Goossens, L. Martinez, N. Glorieux, C. Wilkie-Chancellier, C. O. Ehssein, and S. Serfaty, "Laser ultrasonic analysis of normal modes generated by a voltage pulse on an AT quartz sensor," *Ultrasonics*, vol. 44, pp. e1179–e1182, 2006.

[59] C. Eckl, A. S. Kovalev, A. P. Mayer, A. M. Lomonosov, and P. Hess, "Solitary surface acoustic waves," *Phys. Rev. E*, vol. 70, p. 046604, 2004.

[60] D. H. Hurley, O. B. Wright, O. Matsuda, T. Suzuki, S. Tamura, and Y. Sugawara, "Time-resolved surface acoustic wave propagation across a single grain boundary," *Phys. Rev. B*, vol. 73, p. 125403, 2006.

[61] J. Blackshire, "Ultrasonic scattering from complex crack morphology features," in *IEEE International Ultrasonics Symposium (IUS), 2012*, pp. 248–251, Oct 2012.

[62] X. H. Chapman, K. v. Wijk, J. A. Scales, and G. C. Herman, "Imaging and suppressing near-receiver scattered surface waves," *Geophysics*, vol. 70, no. 2, pp. V21–V29, 2005.

[63] B. A. Auld, *Acoustic Fields and Waves in Solids*, vol. 1 & 2. Krieger Publishing Company, 2nd ed., 1990.

[64] C. H. Chapman, "Generalized Radon transforms and slant stacks," *Geophysical Journal of the Royal Astronomical Society*, vol. 66, no. 3, pp. 445–453, 1981.

[65] J. B. Diebold and P. L. Stoffa, "The traveltime equation, tau-p mapping, and inversion of common midpoint data," *Geophysics*, vol. 43, no. 3, pp. 238–254, 1981.

[66] A. Kebaili and D. R. Schmitt, "Ultrasonic anisotropic phase velocity determination with the Radon transform," *Journal of the Acoustical Society of America*, vol. 101, no. 6, pp. 3278–3286, 1996.

[67] D. H. Johnson and D. E. Dudgeon, *Array Signal Processing: Concepts and Techniques*. Simon & Schuster, 1992.

[68] T. E. Michaels, J. E. Michaels, and M. Ruzzene, "Frequency-wavenumber domain analysis of guided wavefields," *Ultrasonics*, vol. 51, pp. 452–466, 2011.

[69] M. Ruzzene, "Frequency-wavenumber domain filtering for improved damage visualization," *Smart Materials and Structures*, vol. 16, no. 6, pp. 2116–2129, 2007.

[70] A. Croxford, P. Wilcox, B. Drinkwater, and G. Konstantinidis, "Strategies for guided-wave structural health monitoring," *Proceedings of the Royal Society A: Mathematical, Physical and Engineering Science*, vol. 463, no. 2087, pp. 2961–2981, 2007.

[71] Y. Lu and J. E. Michaels, "A methodology for structural health monitoring with diffuse ultrasonic waves in the presence of temperature variations," *Ultrasonics*, vol. 43, no. 9, pp. 717–731, 2005.

[72] A. J. Croxford, J. Moll, P. D. Wilcox, and J. E. Michaels, "Efficient temperature compensation strategies for guided wave structural health monitoring," *Ultrasonics*, vol. 50, no. 4, pp. 517–528, 2010.

[73] J. Harley and J. Moura, "Scale transform signal processing for optimum ultrasonic temperature compensation," *IEEE Transactions on Ultrasonics, Ferroelectrics and Frequency Control*, vol. 59, no. 10, pp. 2226–2236, 2012.

[74] L. Ambrozinski, P. Magda, K. Dragan, T. Stepinski, and T. Uhl, "Temperature compensation based on Hilbert transform and instantaneous phase for Lamb waves-based SHM systems of aircraft structures," in *Proceedings of the 9th International Workshop on Structural Health Monitoring*, vol. 9, pp. 1259–1268, 2013.

[75] Z. Lu, S. J. Lee, J. E. Michaels, and T. E. Michaels, "On the optimization of the temperature compensation for guided wave structural health monitoring," in *AIP Conference Proceedings*, vol. 1211, pp. 1860–1867, 2010.

[76] C. Mow and Y. Pao, *Diffraction of elastic waves and dynamic stress concentrations*. Rand Corporation research study, Crane, Russak, 1973.

[77] S. Sancar, Y.-H. Pao, and W. Sachse, "Spectral analysis of elastic pulses scattered from two cylindrical cavities in a solid," *Journal of the Acoustical Society of America*, vol. 61, no. S1, p. S16, 1977.

[78] G. S. Kino, "The application of reciprocity theory to scattering of acoustic waves by flaws," *Journal of Applied Physics*, vol. 49, no. 6, pp. 3190–3199, 1978.

[79] Y. Al-Nassar, S. Datta, and A. Shah, "Scattering of Lamb waves by a normal rectangular strip weldment," *Ultrasonics*, vol. 29, no. 2, pp. 125 – 132, 1991.

[80] Z. Chang and A. Mal, "Scattering of Lamb waves from a rivet hole with edge cracks," *Mechanics of Materials*, vol. 31, no. 3, pp. 197 – 204, 1999.

[81] M. J. S. Lowe, R. E. Challis, and C. W. Chan, "The transmission of Lamb waves across adhesively bonded lap joints," *Journal of the Acoustical Society of America*, vol. 107, no. 3, pp. 1333–1345.

[82] F. Lanza di Scalea, P. Rizzo, and A. Marzani, "Propagation of ultrasonic guided waves in lap-shear adhesive joints: Case of incident A0 Lamb wave," *Journal of the Acoustical Society of America*, vol. 115, no. 1, pp. 146 – 156, 2004.

[83] Y. Lu, L. Ye, Z. Su, and C. Yang, "Quantitative assessment of through-thickness crack size based on Lamb wave scattering in aluminium plates," *NDT & E International*, vol. 41, pp. 59 – 68, 2008.

[84] P. Fromme and M. Sayir, "Measurement of the scattering of a Lamb wave by a through hole in a plate," *Journal of the Acoustical Society of America*, vol. 111, no. 3, pp. 1165 – 1170, 2002.

[85] O. Diligent, T. Grahn, A. Bostrom, P. Cawley, and M. Lowe, "The low-frequency reflection and scattering of the S0 Lamb mode from a circular through-thickness hole in a plate: finite element, analytical and experimental studies," *Journal of the Acoustical Society of America*, vol. 112, no. 6, pp. 2589 – 2601, 2002.

[86] P. Fromme and C. Rouge, "Directivity of guided ultrasonic wave scattering at notches and cracks," in *Journal of Physics: Conference Series*, vol. 269, p. 012018, 2011.

[87] X. Chen, J. Michaels, and T. Michaels, "A methodology for estimating guided wave scattering patterns from sparse transducer array measurements," *IEEE Transactions on Ultrasonics, Ferroelectrics, and Frequency Control*, vol. 62, no. 1, pp. 208–219, 2015.

[88] A. Velichko and P. D. Wilcox, "A generalized approach for efficient finite element modeling of elastodynamic scattering in two and three dimensions," *Journal of the Acoustical Society of America*, vol. 128, no. 3, pp. 1004–1014, 2010.

[89] J. Zhang, B. Drinkwater, and P. Wilcox, "Longitudinal wave scattering from rough crack-like defects," *IEEE Transactions on Ultrasonics, Ferroelectrics and Frequency Control*, vol. 58, no. 10, pp. 2171 – 2180, 2011.

[90] J. Zhang, B. W. Drinkwater, and P. D. Wilcox, "Defect characterization using an ultrasonic array to measure the scattering coefficient matrix," *IEEE Transactions on Ultrasonics, Ferroelectrics, and Frequency Control*, vol. 55, no. 10, pp. 2254 – 2265, 2008.

[91] R. Szeliski, "Image Alignment and Stitching: A Tutorial," *Foundations and Trends® in Computer Graphics and Vision*, vol. 2, no. 1, pp. 1–104, 2006.

[92] L. G. Brown, "A survey of image registration techniques," *ACM Computing Survey*, vol. 24, no. 4, pp. 325–376, 1992.

[93] C. Schmid, R. Mohr, and C. Bauckhage, "Evaluation of interest point detectors," *International Journal of Computer Vision*, vol. 37, no. 2, pp. 151–172, 2000.

[94] S. Gauglitz, T. Höllerer, and M. Turk, "Evaluation of interest point detectors and feature descriptors for visual tracking," *International Journal of Computer Vision*, vol. 94, no. 3, pp. 335–360, 2011.

[95] R. Cutler, C. S. Shekhar, B. Burns, R. Chellappa, R. C. Bolles, and L. S. Davis, "Monitoring human and vehicle activities using airborne video," vol. 3905, pp. 146–153, 2000.

[96] R. Hess and A. Fern, "Improved video registration using non-distinctive local image features," in *Proceedings of the IEEE Computer Society Conference on Computer Vision and Pattern Recognition*, pp. 1–8, 2007.

[97] R. Wiles, D. Hirvonen, S. Hsu, R. Kumar, W. Lehman, B. Matei, and W.-Y. Zhao, "Video georegistration: algorithm and quantitative evaluation," in *Proceedings of the Eighth IEEE International Conference on Computer Vision, 2001*, vol. 2, pp. 343–350, 2001.

[98] Y. Sheikh, S. Khan, M. Shah, and R. Cannata, "Geodetic alignment of aerial video frames," in *Video Registration* (M. Shah and R. Kumar, eds.), vol. 5 of *The International Series in Video Computing*, pp. 144–179, Springer US, 2003.

[99] A. Rav-Acha, Y. Pritch, and S. Peleg, *Online video registration of dynamic scenes using frame prediction*, vol. 4358 LNCS of *Lecture Notes in Computer Science*. 2007.

[100] M. Nejati, S. Sadri, and R. Amirfattahi, "Nonrigid image registration in digital subtraction angiography using multilevel b-spline," *Biomed Research International*, vol. 2013, p. 236315, 2013.

[101] Y. K. An, B. Park, and H. Sohn, "Complete noncontact laser ultrasonic imaging for automated crack visualization in a plate," *Smart Materials and Structures*, vol. 22, p. 025022, 2013.

[102] J. E. Michaels, S. J. Lee, A. J. Crawford, and P. D. Wilcox, "Chirp excitation of ultrasonic guided waves," *Ultrasonics*, vol. 53, pp. 265–270, 2013.

[103] F. J. Harris, "On the use of windows for harmonic analysis with the discrete Fourier transform," in *Proceedings of the IEEE*, vol. 66, pp. 51–83, 1978.

[104] J. Achenbach, A. Gautesen, and H. McMaken, *Ray Methods for Waves in Elastic Solids: With Applications to Scattering by Cracks*. Monographs and Studies in Mathematics, Pitman Advanced Pub. Program, 1982.

[105] J. Krautkramer and H. Krautkramer, *Ultrasonic Testing of Materials*. New York: Springer-Verlag, 1977.

[106] Olympus Corporation, *Flaw Detector: Angle Beam*, Accessed: March 15, 2015. url: http://www.olympus-ims.com/en/ultrasonic-transducers/angle-beam/.

[107] N. R. Pal and S. K. Pal, "A review on image segmentation techniques," *Pattern Recognition*, vol. 26, no. 9, pp. 1277–1294, 1993.

[108] P. Soille, ed., *Morphological Image Analysis: Principles and Applications*. Berlin; New York: Springer.

[109] MatLab™, *imfill*, Accessed: January 19, 2015. url: `http://www.mathworks.com/help/images/ref/imfill.html`.

[110] F. v. d. Heijden, ed., *Image Based Measurement Systems: Object Recognition and Parameter Estimation*. Chichester, New York: Wiley.

[111] MatLab™, *regionprops*, Accessed: May 12, 2015. url: `http://www.mathworks.com/help/images/ref/regionprops.html`.

[112] K. Salama and C. Ling, "The effect of stress on the temperature dependence of ultrasonic velocity," *Journal of Applied Physics*, vol. 51, no. 3, pp. 1505–1509, 1980.

[113] B. S. Reddy and B. N. Chatterji, "An FFT-based technique for translation, rotation, and scale-invariant image registration," *IEEE Transactions on Image Processing*, vol. 5, no. 8, pp. 1266–1271, 1996.

[114] MatLab™, *fminsearch*, Accessed: January 19, 2015. url: `http://www.mathworks.com/help/matlab/ref/fminsearch.html`.

[115] X. Liang, X. Ren, Z. Zhang, and Y. Ma, "Repairing sparse low-rank texture," in *Computer Vision: ECCV 2012*, (Heidelberg), pp. 482–495, Springer-Berlin, 2012.

[116] Z. Lin, A. Ganesh, J. Wright, L. Wu, M. Chen, and Y. Ma, "Fast convex optimization algorithms for exact recovery of a corrupted low-rank matrix," *Computational Advances in Multi-Sensor Adaptive Processing (CAMSAP)*, vol. 61, 2009.

[117] H. Mobahi, S. R. Rao, A. Y. Yang, S. S. Sastry, and Y. Ma, "Segmentation of natural images by texture and boundary compression," *International Journal of Computer Vision*, vol. 95, no. 1, pp. 86–98, 2011.